Det Norske Videnskaps-Akademi i Oslo

Geofysisk årbok

GEOFYSISKE PUBLIKASJONER

VOL. 30 NO. 4 1973

UNIVERSITETSFORLAGET

Geophysica Norvegica

is a journal of geophysics, issued under the auspices of the Norwegian Academy of Science and Letters in Oslo

PUBLISHER

Universitetsforlaget: P. O. Box 307, Blindern, Oslo 3, Norway.
P. O. Box 142, Boston, Mass. 02113, U.S.A.

SUBSCRIPTION

Geophysica Norvegica (Geofysiske Publikasjoner) is published at irregular intervals. Order from the Publisher, Universitetsforlaget.

Geophysica Norvegica (Geofysiske Publikasjoner) is a series of scientific publications issued by the Norwegian Academy of Science and Letters in Oslo. The Geophysical Commission appoints an editor and editorial committee.
Manuscripts for publication in Geophysica Norvegica should be carefully prepared (see Instructions to Author on p. 3 of the cover) and sent to the editor. The next step is the manuscript's submission to the Academy by a competent member, who is responsible for ensuring that the paper meets a sufficiently high scientific standard. (Members of the Academy are allowed to submit their own papers.) The final decision as to whether the paper should be published is taken by the editor.
Geophysica Norvegica is mainly intended as a journal for Norwegian authors, but papers from other authors may be accepted provided that the work has been carried out at a Norwegian institution or its content has a special relevance to Norway.

Electric Field Microstructures in the Auroral E-Region

J. A. HOLTET
The Norwegian Institute of Cosmic Physics, Blindern, Oslo, Norway

Holtet, J. A. Electric Field Microstructures in the Auroral *E*-Region. *Geophysica Norvegica*, Vol. 30, No. 4, 1973.

The present work represents a study of microstructures in the auroral *E*-region based on in situ observations of AC electric fields. The main characteristics of the observed wavefields, called ELF *E*-layer noise, are as follows:

1) The emissions appear in the altitude region 95–120 km.
2) The noise is found in the range 50 Hz to 3 kHz.
3) The orientation in space of the wave *E*-field vector is well defined and is approximately in the magnetic east-west direction. This does, however, change significantly with altitude.
4) The wave is electrostatic.

It is shown that these fields can be generated by a two-stream plasma instability. The observed characteristics are compared with features derived using linear instability theory and an ionospheric model representing the observation conditions, and a good correspondence is found. An additional piece of information obtained from the measurements is that the wavefield observations give means to record small scale variations in the direction of the electric current.

J. A. Holtet, The Norwegian Institute of Cosmic Physics, Blindern, Oslo 3, Norway

The day will yet come when the progress of research through long ages will reveal to sight the mysteries of nature that are now concealed. A single lifetime, though it were wholly devoted to study, does not suffice for the investigation of problems of such complexity... It must, therefore, require long successive ages to unfold all. The day will yet come when posterity will be amazed that we remained ignorant of things that will to them seem so plain.

Seneca. Naturales quaestiones 7.25 (about A.D. 63).

A. Omholt submitted this paper to the Norwegian Academy of Science and Letters in Oslo, 6th April 1973.

CONTENTS

1. INTRODUCTION AND OUTLINE

The main purpose of this study was to perform an experimental and theoretical investigation of small-scale irregularities in the auroral *E*-region. 'Small-scale' in this context means structures with horizontal extent in the range 10^{1}–10^{-1} m.

The experimental basis was in situ observations of AC electric fields during the presence of visual aurora. Variational fields of this kind can be directly related to irregularities in the distribution of thermal electrons. Their presence has earlier been postulated from measurements of other ionospheric parameters and on theoretical grounds. The technique utilized in the present study has, however, provided a new approach to the problems. In situ observations give first-hand information about spectral distribution and direction of the wavefield, together with variations of the wave properties *vs.* altitude. The direct result of this is improved mapping of the small-scale electric fields in the *E*-region. This, in turn, leads to a better understanding of physical processes involved in the formation of irregularities in this part of the ionosphere.

To give an impression of the kind of irregularities which will be considered, and outline the problem, we will begin with a presentation of the experimental results together with a short discussion of the raw data (Chapter 2). In dealing with ionospheric irregularities it is, however, necessary to obtain information about the 'regular' ionosphere. In Chapter 3, therefore, we rather summarily give a picture of the ionospheric medium, and present various ionospheric parameters and their variations, while Chapter 4 deals with the electrodynamics of the ionosphere – the motion of charged particles influenced by electric and magnetic fields. This is followed in Chapter 5 by a presentation of auroral current systems, a result of the particle motions. In the same chapter we will evaluate the present knowledge about large-scale electric fields, the driving force of the currents. Furthermore, we will present some observations of DC fields in auroral situations and go into the experimental technique for measuring electric fields in the ionosphere. Details of this subject will be further discussed in Appendices I and II.

Supporting the observations of small-scale electric fields, presented in Chapter 2, is the presence of microstructures in the electron distribution observed at the same time as the field variations. These recordings, made by the VLF Doppler technique, are described in Chapter 6. To see our observations in a wider perspective, the subject for the following chapter is small-scale irregularities in the auroral *E*-region in general, giving a survey of observed small-scale structures in particle precipitation, optical aurora, and radio aurora.

The source of *E*-region microstructures is likely to be found in a plasma instability (Chapter 8). It is deduced that the observed features during the existing ionospheric conditions can plausibly be explained by a modified two-stream instability.

The last chapter is devoted to comparisons and discussions of the instability theory *vs.* observed features. The primary parameter in generation of the instability is the electron-ion drift velocity. Both frequency, amplitude, and direction of the wavefield depend on this property. A supplementary result from the observations is therefore that from observations of the field direction one can track the velocity vector and thus record small-scale variations in the direction of the current.

The observation of the *E*-region irregularities came as an unexpected result from an experiment originally flown to measure very low frequency radio emissions in aurora. The payload was therefore not primarily composed to give thorough information about the *E*-region plasma. In the comparison between observed and theoretically derived properties of the wavefield one is therefore limited to the use of a somewhat simplified ionospheric model. However, essential observed features as altitude region, amplitude *vs.* frequency distribution, and direction of the wavefield in space, correspond very well to that predicted from the theoretical model study.

2. IN SITU MEASUREMENTS OF *E*-REGION ELECTRIC FIELD MICROSTRUCTURES

2.1. *Introduction*

The observations which constitute the basis for this study, and which will later be put into a wider

perspective, are the results from measurements of small-scale variations in the electric field. The observations were made by means of rockets, and are based on the double floating probe technique. The measuring technique and instrumentation will be described in detail in Chapter 5 and Appendix I.

The data mainly originate from two rocket flights, F23 and F24, but, for comparison, results from two other rockets (NASA 14.383 and 18.57) will also be mentioned. The main point will be the presence of small-scale fields in the *E*-region, but to get an impression of the entire picture, the AC observations at other altitudes will also be briefly described.

2.2 *Launch conditions and payload operation*

The rockets were launched from Andøya Rocket Range in Northern Norway. Coordinates for the range are: Geographic 69.3°N, 16.0°E, corrected geomagnetic 66.1°N, 103.1°E (Hakura 1965). Magnetic midnight (eccentric dipole time) is about 2200 UT. The launch site is located approximately 120 km magnetic west of Tromsø (Auroral Observatory), 230 km magnetic northwest of Kiruna (Rocket Range and Geophysical Observatory), and 600 km magnetic south-west of Bear Island (magnetic observatory).

The rockets were night flights, and were fired during weakly to moderately disturbed conditions. Visual aurora was present in or close to the launch direction of F23, F24, and NASA 18.57, while no aurora could be seen near the trajectory of NASA 14.383. The main characteristics of the payloads, together with information about ionospheric disturbances, are summarized in Table 2.1. The launch conditions for F24 and F23 will be described in more detail.

F24: Even though ground observations of the ionosphere at the launch time of F24 (0017.37 UT, March 8, 1970) gave evidence of moderate activity, the period when the launch took place must be described as very disturbed. A SC at 0805 UT, March 5 preceded a minor storm and a second SC, which initiated a great storm, started at 1420 UT, March 8. However, the conditions during the launch period were dominated by a minor PCA which was reported to start about 1410 UT, March 6. The ATS-1 records indicated a maximum for the proton event some time before 0020 UT, March 8 (ESSA 1970). A PCA caused by precipitation of high energy solar particles will establish relatively stable ionospheric conditions over a large scale (Hultqvist 1968). The main features will thus be conserved over a long

Table 2.1. Flight characteristics and launch conditions

Rocket code	F24	F23	NASA 14.383	NASA 18.57
Rocket type	Nike/Tomahawk	Nike/Tomahawk	Nike/Apache	Nike/Tomahawk
Launch date	March 8, 1970	Nov. 13, 1970	Jan. 12, 1972	Jan. 16, 1973
Launch time ($T = 0$), UT	0017.37	2219.41	2116.35	2058.51
Azimuth setting,°	320	320	343	345.5
Peak altitude, km	216	214	197	260
Spin period, *s*	1.8	1.09	0.48	1.1
Coning period, *s*	260	175	40	170
Coning half angle,°	20	17.5		
E-field exp.	DC, widebd., spectr.	DC, widebd., spectr.	DC, spectr.	DC, spectr.
Auroral cond.	Glow	Patchy glow	No near trajectory	Glow, double arc
Kp	4+	2o	2−	3−
Dst, γ	−43	−18		
CNA(27,6 MHz, $T = 0$), dB	0.6	0.7	0.2	4.5
Magn. act. ($T = 0$), γ	−300 (ΔH)	−240 (ΔH)	+50 (ΔX)	−150 (ΔX)

period, but this does not prevent other perturbations from being superimposed on the slow PCA variation.

The launch took place in the recovery of a negative bay, and the deflection in the *H*-component decreased fairly steadily from −290 to −190 γ during the flight (*cf.* Fig. 2.1, curve b). The deviation in magnetic *H* and *Z* at Bear Island, Tromsø, and Kiruna, gave evidence of a westward electrojet with the integrated current system located to the north of, but close to the launch site zenith. Thus, the rocket trajectory was most likely to the north of the main electrojet. The *Kp* value of 4 (6− in the previous 3-hour interval) and the *Dst* figure of −43 γ showed a high magnetic activity.

The auroral situation was dominated by a fairly homogeneous and quiet glow which covered the launch direction. The intensity of the N_2^+ (4278) emission as measured from the ground decreased slowly from about 1.2 to 0.9 kR, without any marked structure (*cf.* Fig. 2.1.c). Photographs indicated, however, the presence of very faint discrete forms within the glow.

Propagation studies of VLF waves, both from transmitters and naturally emitted (atmospherics), showed stable 'day time' propagation conditions, as are normal for a PCA event. This means that the precipitation of energetic particles caused ionization below 80 km resembling a day time *D*-layer (*cf.* Sect. 3.4). The cosmic noise absorption (27.6 MHz) at Tromsø, Andøya, and Kiruna, which gives an indication of the precipitation of high energy particles ($E > 40$ keV), was low (0.5 to 1 dB) but fairly constant (Fig. 2.1.a).

F23: This rocket was launched in a more typical auroral situation, with more structures and rapid

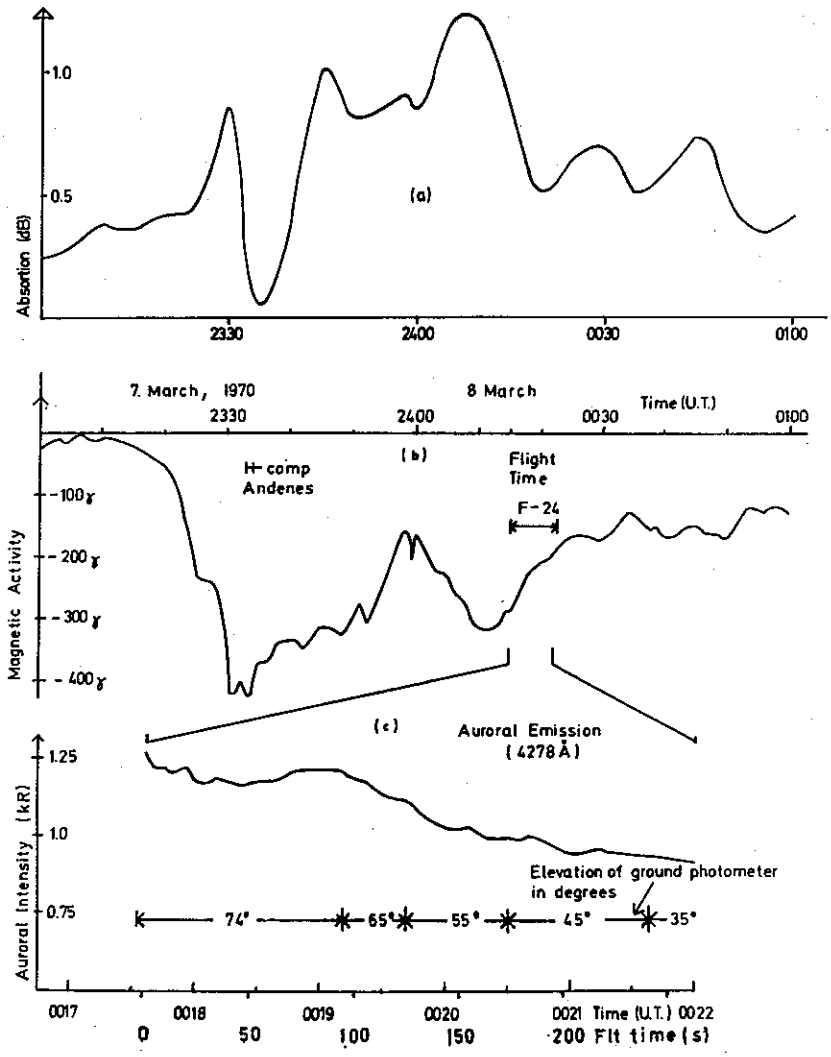

Fig. 2.1. Cosmic noise absorption at 27.6 MHz (curve (*a*)) and deviation in the magnetic *H*-component (curve (*b*)) measured at the launch site for the F24 launch period. Curve (*c*) shows the intensity of the auroral N_2^+ (4278 Å) emission as measured from the launch site at different elevation angles in the plane of the rocket trajectory. The elevation angles were selected to watch the particular parts of the aurora which were expected to be magnetically linked to the rocket during the different periods of the flight. The photometers were in a fixed position in each period.

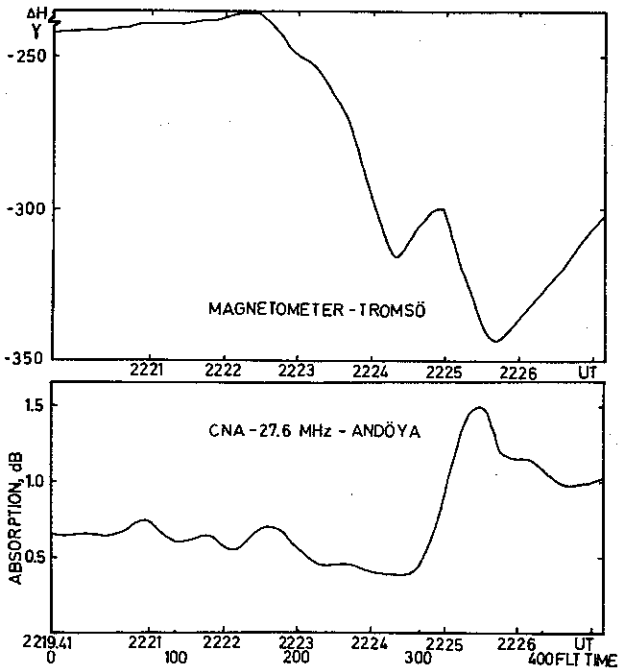

Fig. 2.2. Deviation in magnetic *H*-component (Tromsø) and cosmic noise absorption at 27.6 MHz (Andøya) during the flight of F23.

variations. Generally, the ionospheric conditions during the flight period can be characterized as moderately disturbed. The launch took place in the expansive phase of a substorm (*cf.* Sect. 5.2), but the situation as a whole was too complicated to allow a schematic classification. The deviation in magnetic *H*-component was at launch approximately -250 γ, but during the flight this increased rather suddenly and reached a peak value of -350 γ (*cf.* Fig. 2.2.a). The magnetic observations indicated a westward current system, consistent with the adopted current configuration for the substorm growth phase (*cf.* Sect. 5.2), with its centre somewhat to the north of the launch site. The *Kp* and *Dst* figures were respectively 2o and -18 γ.

The cosmic noise absorption was also subject to large variations. From a fairly steady value of approximately 0.5 dB before and during the first part of the flight the absorption suddenly increased to about 1.5 dB, giving evidence of a sudden influx of energetic particles (Fig. 2.2.b). One may here find some resemblance with the F24 conditions, with energetic precipitation both in the PCA and in the sudden absorption event. However, the particle populations will most probably be quite different – while protons will dominate in the PCA precipitation, electrons will be most abundant in the SA flux (*cf. e.g.* Hultqvist 1968).

No photometric recordings of the aurora exist for this period, due to cloud coverage. From photographic observations at Tromsø the aurora can, however, be described as a patchy glow with weak structures near the launch direction. Vertical sounder records made at 2200 and 2300 UT at Kiruna and Tromsø showed the existence of sporadic *E*-layer. (In the case of F24 the low altitude absorption layer associated with the PCA precluded sounder measurements.)

Mechanically the two rockets were very similar, and in both cases the launcher settings were the same, with an azimuth angle of $\sim 320°$. The peak altitudes were 216 km (F24) and 214 km (F23). F24 had a spin period after despin and antenna deployment of 1.8 s. The precession cone, as determined by two fluxgate aspect magnetometers, opened up to 20° half angle and the precession period was approximately 260 s. The orientation of the cone was such that the spin axis was parallel to **B** once (near 204 km on the descent part). F23 had a spin period of 1.09 s, the axis of rotation was on a cone with 17.5° half angle, and the coning period was 175 s. In the attitude calculations it is assumed that the angular momentum vector lay in the plane of the trajectory.

In both payloads the *E*-field experiments functioned satisfactorily, without any problems of mechanical or electrical kind, and with a low interference level. The antennas were fully extended at 157 km for F24 and 138 km for F23. Atmospheric drag caused bending of the elements below 95 km on the descent path which disturbed the geometrical configuration and jammed the DC measurements (*cf.* Appendix I). AC data were obtained until the elements started to break off around 80 km. However, within the last 10 km a considerable amount of transient noise was present because of the unstable probe situation.

The DC measurements from the flights will be presented in Chapter 5. It will only be mentioned here that the general impression of the records fits the pictures of the launch conditions, with a

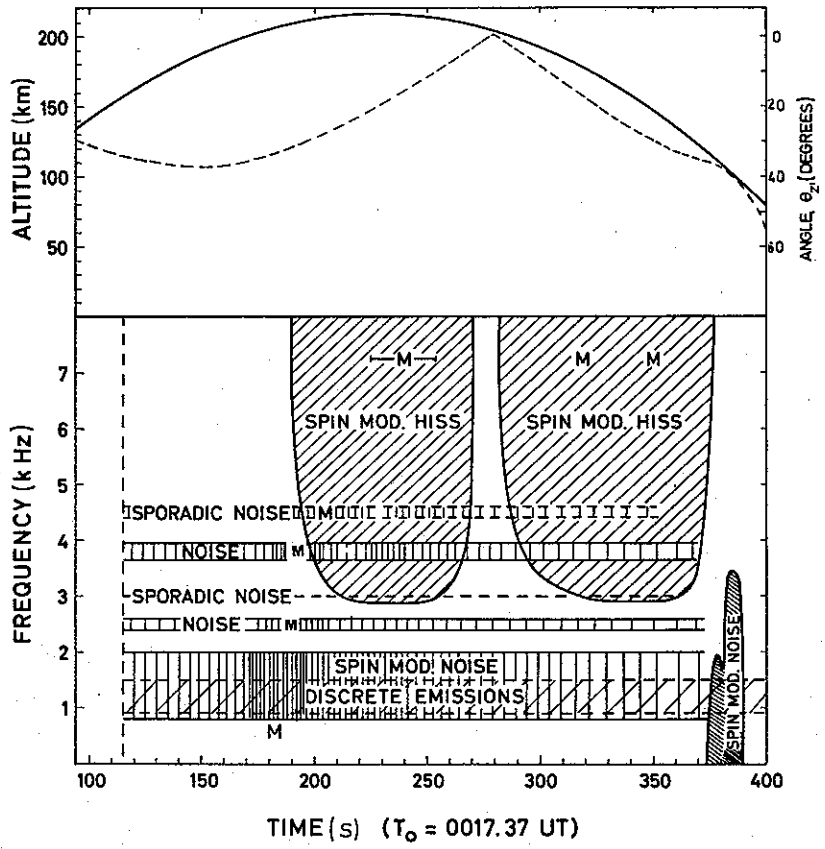

Fig. 2.3. Survey of different emissions recorded during the flight of F24. *M*'s denote region of maximum signal intensity. Altitude and angle between the rocket axis and the earth's magnetic field are given in the upper part of the figure.

slowly varying field during the F24 event and more dynamic variations in the F23 case.

2.3. *AC measurements above 130 km*

The AC fields observed above 130 km will only be briefly summarized, because these measurements will not be important in the following discussions. They will mainly serve to set off the low altitude recordings. (For a more detailed description of the observed emissions, *cf.* Holtet *et al.* 1971 *a*, *b*.)

A survey of the different emissions as observed by the wideband channel in F24 is given in Fig. 2.3. The noise above 130 km can roughly be divided into three groups, *i.e.* discrete emissions, noise bands below 5 kHz, and hiss above 3 kHz. (For the emission terminology, *cf. e.g.* Helliwell 1965.)

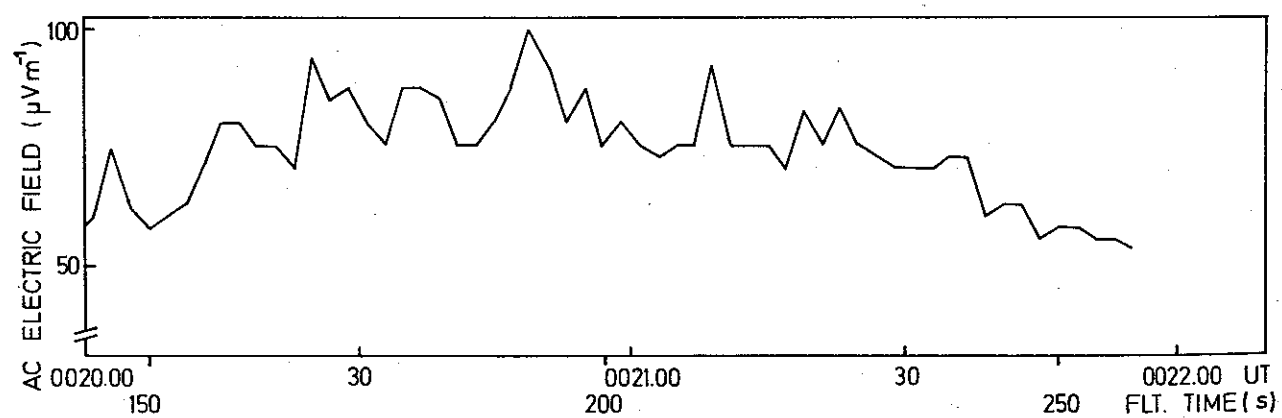

Fig. 2.4. The AC electric field in range 1 to 10 kHz *vs.* time for the flight period 150 to 250 s of F24.

Discrete emissions, both risers and more complex forms, appeared sporadically throughout the whole flight in the frequency range 1 to 2.5 kHz. There was a maximum around 180 s, but this peak was not pronounced.

Several noise bands with different bandwidths (*cf.* Fig. 2.3) were present during most of the recording period between approximately 0.8 and 4.7 kHz. The intensity of the noise was partly spin modulated, showing an anisotropy in the wavefield. A broad, but pronounced maximum appeared between 150 and 230 s flight time (Fig. 2.4). This corresponds to a region with decreased DC field, and the fluctuations in DC and AC field strengths were also almost in antiphase. It should be noted that the spin modulation was less marked in this region.

Spin-modulated wideband noise (hiss) above 3 kHz occurred in two bursts, lasting from about 190 to 270 s and 280 to 375 s flight time. It should be noted that the minimum between 270 and 280 s corresponds to the time when the rocket axis was approximately parallel to the magnetic field lines. The intensity of the signal integrated over one complete spin period was, however, rather slowly varying, and this emission showed no resemblance with the intense fluctuating emission known as auroral hiss (Helliwell 1965).

In general one can say that also the AC measurements reflect the stable and slowly varying PCA conditions.

The emission spectrum and variations recorded in the F23 event (summarized in Fig. 2.5) were basically different from that found in the F24 flight.

In this case hiss emissions were also present above approximately 6 kHz, but compared to the F24 hiss, these emissions were much more intensive and the amplitude fluctuated quite vigorously. According to VLF terminology these emissions should be classified as auroral hiss. Maximum signal strength appeared in several bursts between 210 and 250 s flight time. It will be noted that this corresponds to a peak in the DC field (*cf.* Sect. 5.6), and also that in the more rapid time variations the two records follow each other.

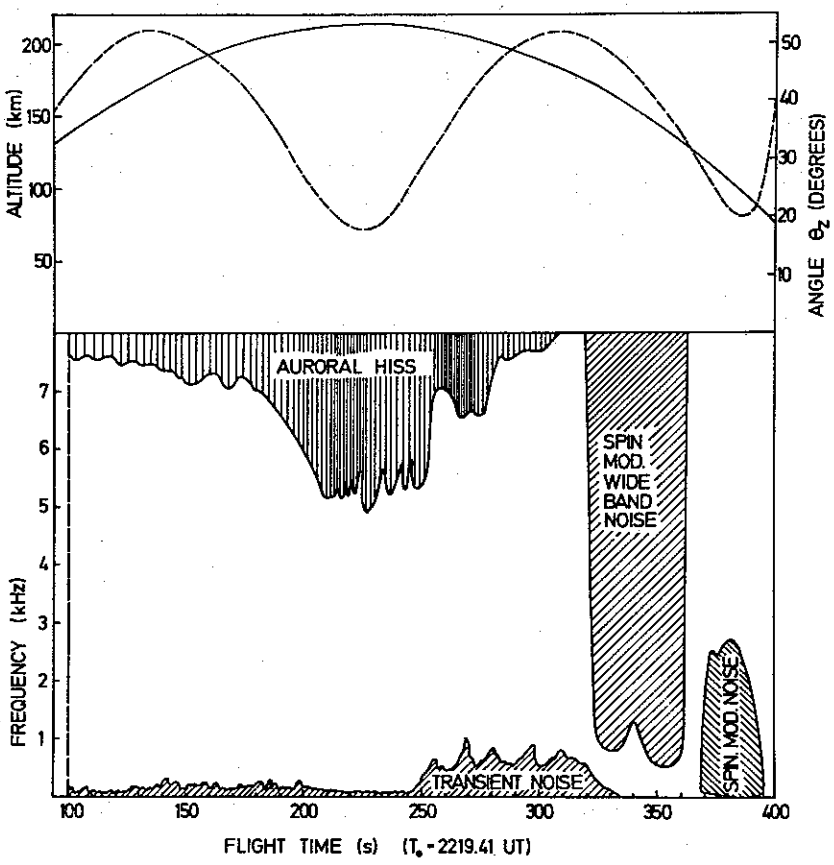

Fig. 2.5. Survey of emissions recorded during the flight of F23 together with a plot of altitude and angle between the rocket axis and the earth's magnetic field.

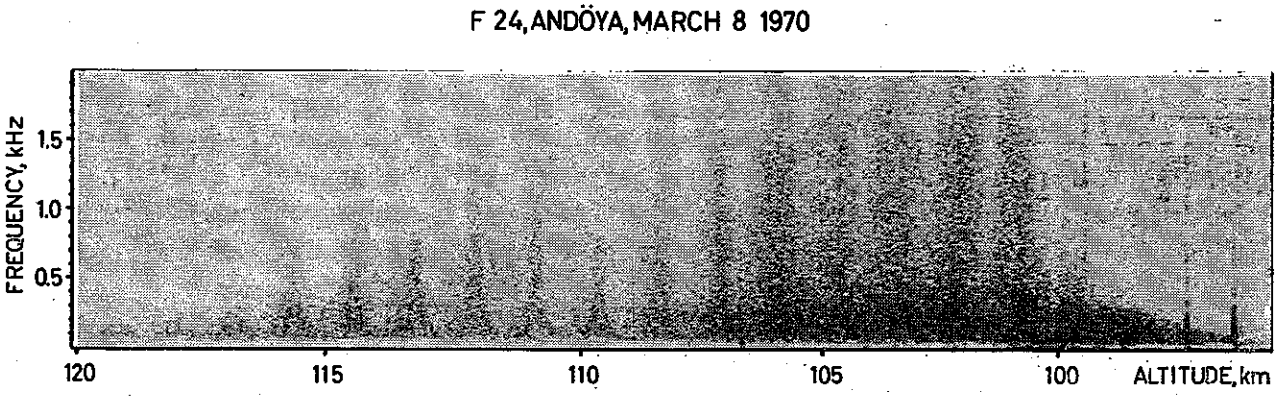

Fig. 2.6. Spectrogram of ELF *E*-layer noise recorded in the F24 event.

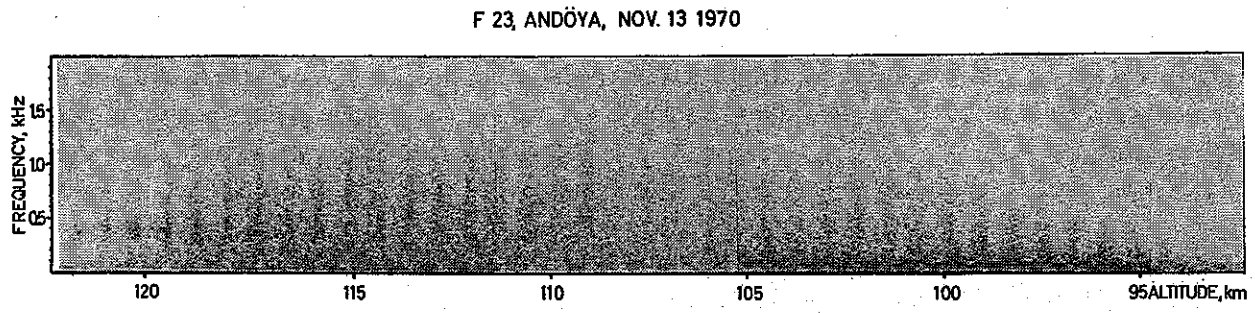

Fig. 2.7. Spectrogram of ELF *E*-layer noise in the F23 event.

This is quite contrary to the behaviour of the F24 noise bands.

In addition to the auroral hiss, two other kinds of emissions were observed. One was a band of noise bursts of rather transient character appearing below 1 kHz. The maxima in this noise appeared out of phase with the auroral hiss. The other type may be of more interest, as its onset can obviously be associated with the increased CNA, *i.e.* increased flux of high energy particles. The emission can be characterized as wideband noise from approximately 0.1 kHz to several tens of kHz. In the weaker parts it was spin modulated, but in the strongest bursts no spin modulation was present.

2.4. *AC measurements below 130 km*

Both the launch conditions and the observations made during the flight were very different for these two rockets. Furthermore, the difference in coning angle and period made the attitude of the rocket body and *E*-field antenna with respect to the earth's magnetic field quite different, for the flight in general and below 130 km in particular. In spite of this the general appearance of the AC electric fields observed in the height interval 130–90 km were almost identical for the two rockets. These fields, which spectrographically can be described as wideband noise with maximum intensity below 500 Hz (Figs. 2.6 and 2.7), will be termed ELF *E*-layer noise.

The similarity in the observations made under such different conditions makes us believe that our observations are fairly typical for this phenomenon. In the following we will briefly present what appear to be characteristic features for this *E*-layer noise.

a: The noise is located in the height interval 90–130 km.

b: The emissions cover frequencies from about 50 Hz to 3–4 kHz, with maximum amplitude in the lower part of the spectrum. The power spectrum is asymmetrical with a faster roll-off on the low frequency than on the high frequency side (*cf.* Fig. 2.8). This may, however, be somewhat modified by the frequency response of the antenna and electronics. The low frequency limit was, however, also verified by the recordings from the DC channel, which

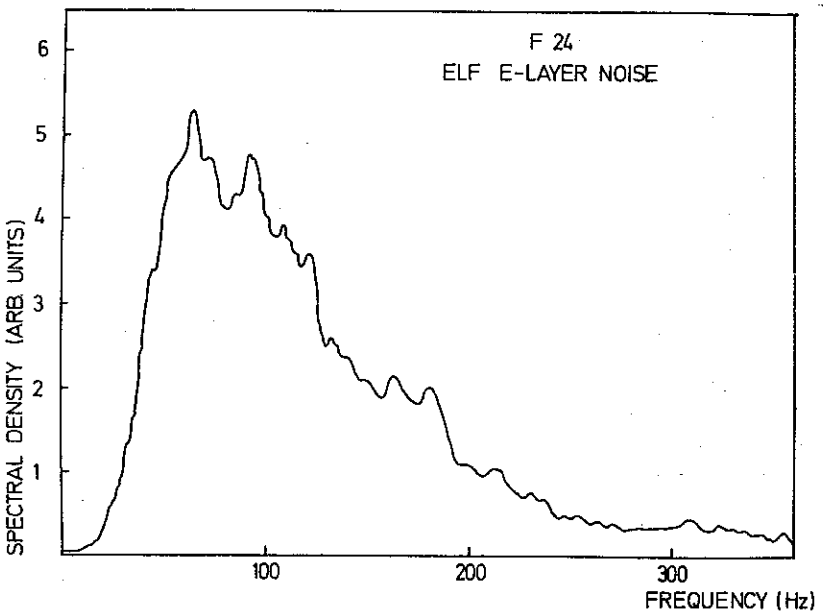

Fig. 2.8. Power spectrum of ELF *E*-layer noise recorded by F24. The spectrum is integrated over the total duration of the emissions.

has an AC response up to about 300 Hz (*cf.* Fig. 9.5).

c: The measured amplitude of the field reaches a maximum of about 5 mV m^{-1}.

d: There is no marked peak in the amplitude *vs.* frequency representation (Fig. 2.8).

e: The recorded signal is spin modulated with period equal to half the spin period (Fig. 2.9.) The direction of the electron field is thus well defined. This is even more clear if the width of the antenna pattern is taken into account. The modulation is most marked at high frequencies, and is more pronounced for the upper 15 km of the region than it is for the fields detected in the lower *E*-layer. In the last part of the noise burst, no spin modulation at all can be seen, as if the waves are scattered in all directions and the structure smeared out in the

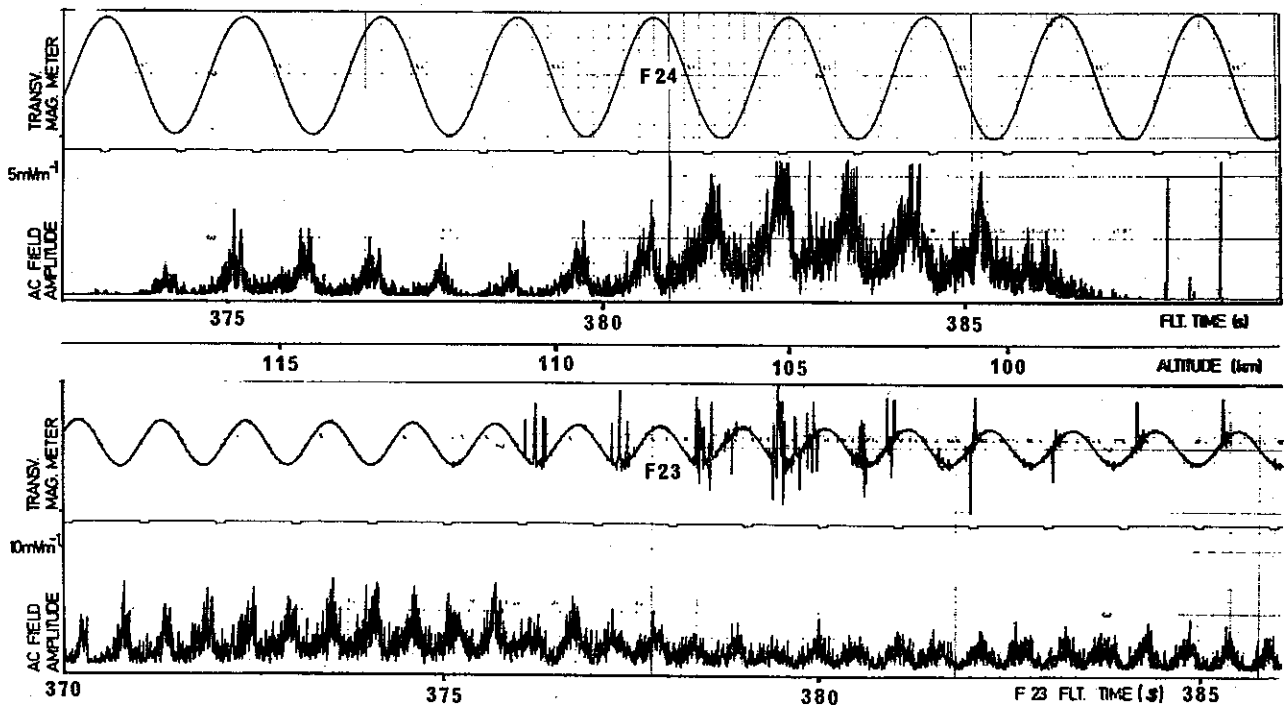

Fig. 2.9. Amplitudes of ELF *E*-layer noise and signals from the rocket's transverse magnetometer recorded as function of flight time for F24 (upper) and F23 (lower).

denser medium. The thickness of this 'diffusive region' is approximately 4 km (*cf.* Figs. 2.6, 2.7, and 2.9). Much finestructures, with large and rapid fluctuations, are, however, present in the amplitude *vs.* time record (Fig. 2.9). It can also be noted that in some cases the 'heaps' following the rocket spin have a double peak. This means that amplitude maxima occur in two directions close to each other. As this does not appear in all maxima it is supposed to be real effect and not caused by the antenna radiation pattern.

f: Maximum amplitude and widest frequency range are generally found when the direction of the antenna is near the magnetic east-west direction (*cf.* Fig. 2.10 which is based on data from F24).

g: The direction of maximum field strength is not constant in space, but can shift with altitude. This can be seen on data from F24 (Fig. 2.10), but is much more pronounced in the F23 measurements (Fig. 2.11) where a shift of approximately 30° occurs. In the F 23 measurements difficulties in determining the exact

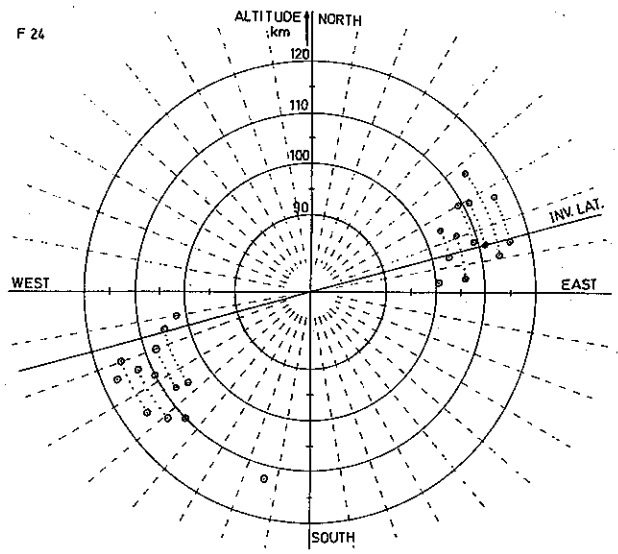

Fig. 2.10. Orientation of the *E*-field antenna in a topographical coordinate system at the times of maximum amplitude in the spin-varying ELF *E*-layer noise bursts (*cf.* Figs. 2.6 and 2.9). Two points connected by a dotted line indicate a double peak in the same burst. Distance from the centre gives the rocket altitude. The line marked INV. LAT. is the direction of constant invariant latitude at 100 km. Data from F24.

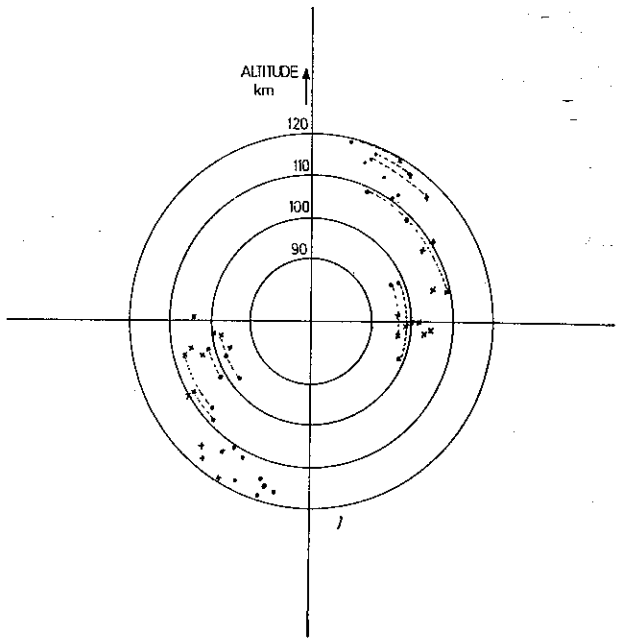

Fig. 2.11. Orientation of the *E*-field antenna in an arbitrary horizontal coordinate system at the times of maximum amplitude in the spin modulation of ELF *E*-layer noise. Points connected by a dotted line indicate multiple peaks in the same burst. Distance from the centre gives the rocket altitude. Data from F23.

orientation in space of the rocket from the magnetic aspect records have made it impossible to locate the electric fields accurately in a topographical coordinate system. However, the changes in direction seen in Fig. 2.11 are quite significant, but the location of the axis is arbitrary. A conspicuous feature in this plot is the division of the points of maximum signal into marked groups, shifted about 30° in direction. The transition takes place quite suddenly around 110 km. It should be noted that at the same altitude the rocket magnetometer showed strong fluctuations, giving evidence of a large local perturbations of the magnetic field (*cf.* Fig. 2.9).

Without listing it as a 'characteristic property' it can be noted that in both cases the enveloping curve for the amplitude *vs.* time (*i.e* the curve touching the peaks in this record) follows the same pattern and has two marked maxima. This is no artificial effect caused by variations in the rocket attitude. It can also be seen from Figs. 2.6 and 2.7 that the spectral impressions of the emis-

sions in these two bursts are somewhat different. The noise, in the lowest frequencies, is stronger in the second burst, and the spin modulation is less pronounced (*cf.* also point d above). The amplitude minimum of F23 appears approximately where the change in the direction for maximum amplitude takes place.

If we turn to the rocket NASA 14.383, which carried *E*-field instrumentation identical to that in F23 and 24, no *E*-layer noise was observed. The electric field recordings in this rocket were, however, disturbed by some interference, but as this disturbance was not present throughout the flight, sufficient good data were obtained to conclude that this special emission was not present. However, the general disturbance level (*cf.* Table 2.1) was lower at the launch of this rocket than in the two other events, and the rocket particle detectors showed hardly any precipitation of low energy ($E < 15$ keV) particles (Evans, priv. com.).

The rocket NASA 18.57 was launched January 16, 1973, 1959 UT, and was fired in the breakup phase of a substorm. Only preliminary data can be presented. However, a very clear case of ELF *E*-layer noise was recorded. The noise seems to be shifted somewhat down in frequency from the earlier cases, but the main characteristics are similar. Preliminary calculated directions of the antenna in the noise maxima are shown in Fig. 2.12. The east-west orientation is also found in this case.

2.5. *Other observations of ELF E-layer noise*

Recently we have become aware of observations made from a rocket, S70/1, flown from Kiruna, February 24, 1970 (Ungstrup, priv. com.). The launch took place during an auroral glow situation with weak discrete forms. The rocket was equipped with electric field instrumentation using spherical probes (Danish Space Research Institute). We had the opportunity to study these data; the recordings at *E*-region altitudes appeared to be very similar to those made in F23 and F24. On the upleg, *E*-layer noise was present between 98 and 115 km, and on the downleg from 120 to 99 km. The orientation of the antennas at maximum amplitude was mainly in the east-west direction, in agreement with the observations from the Andøya rockets. The S70/1 instrumentation also included magnetic antennas. It should be noted that no trace of the *E*-layer noise could be seen in the magnetic records.

Further support for the presence of ELF *E*-layer noise during aurora has been given from two rocket experiments flown in Canada (Maynard, priv. com.). In both these cases spin modulated ELF noise was seen when penetrating the *E*-region.

2.6. *Discussion of the raw data*

As far as the author knows, similar observations have not been reported in the literature. The recordings that bear most resemblance were made by a Japanese group (Iwai *et al.* 1966) and a group at the University of Iowa (Gurnett & Mosier 1969), who observed noise bursts in the same frequency range. It is, however, believed that the noise observed in these cases was not of natural origin, but was generated by an interaction between the rocket and the surrounding plasma (Gurnett & Mosier loc. cit). If we compare these observations with the *E*-layer noise, first of all the altitudes where the noise bursts appear do not agree. While we found this special emission exclusively in the *E*-layer, the other observers detected the noise bursts above 150 and 200 km, respectively, and noticed a systematic decrease in intensity with increasing altitude. This contradicted our findings. Furthermore, the noise showed a very pronounced precession modulation. This effect was not present in our measurements, and the attitudes of the two rockets were also quite different in the periods when the *E*-layer noise was present (*cf.* Figs. 2.3 and 2.5).

The *E*-layer noise thus diverges from the other observations of ELF noise bursts in so many respects that it can be concluded that these two phenomena are of a quite different nature. Electronic payload interference can in our case be excluded as a possible source of the noise. Other possible mechanisms for artificial generation of the field variations (*cf.* Appendix 1) have been examined and rejected.

It can therefore be concluded that the ELF *E*-layer noise is of natural origin. Additional sup-

port for this conclusion is provided by independent observations with different instrumentation, as in the case of our rockets and S70/1 described above.

It is important for the study of the wavefield and its origin to determine whether the waves are electrostatic or electromagnetic. The measurements from S70/1 seem to give evidence of electrostatic waves. This will be further discussed in Chapters 8 and 9.

One should, however, in these measurements be aware of the effects which could be caused by small-scale density gradients in the plasma (*cf.* Appendix I). Such variations will cause fluctuations in the probe contact potentials, which may give rise to detectable potential differences. This would be very difficult to distinguish from real field variations, as the two effects would most probably appear simultaneously. Thus an absolute determination of the amplitude of the field is difficult.

3. CHARACTERISTICS OF THE IONOSPHERIC MEDIUM

3.1. *Introduction*

For historical reasons the ionosphere is divided into three main parts: The *D*-region situated between approximately 50 and 90 km, the *E*-region continuing upwards to about 150 km, and the *F*-region extending further to about 500 km. Even though there are no sharp divisions between these layers, it is convenient to make this separation when discussing ionospheric properties. The present work will concentrate on small-scale irregularities in the *E*-region, but to get an impression of what is special for this region and the relations which establish its upper and lower limit, it is necessary to give a brief general view of the ionosphere, up to say 200 km. Our knowledge of ionospheric characteristics was until the mid-1950's derived mainly from ground-based radio and optical measurements. Development of reliable rocket instrumentation during the last two decades has, however, enlarged and revised our knowledge of the ionosphere considerably. New ground techniques, such as radar scattering, partial reflections, and VLF propagation studies, have also contributed with valuable results. However, several uncertainties and question-marks still remain, and the two basic techniques, in situ measurements by rockets and indirect, long-term observations from the ground, which can be 'calibrated' by rocket-measured values, must be joined to give more complete information about the ionosphere.

3.2. *The neutral atmosphere and its properties*

3.2.1. *Composition of the upper atmosphere.* The composition and distribution of the neutral components in the atmosphere are important not only for the production of the charged species and the ion chemistry, but also for the dynamics of

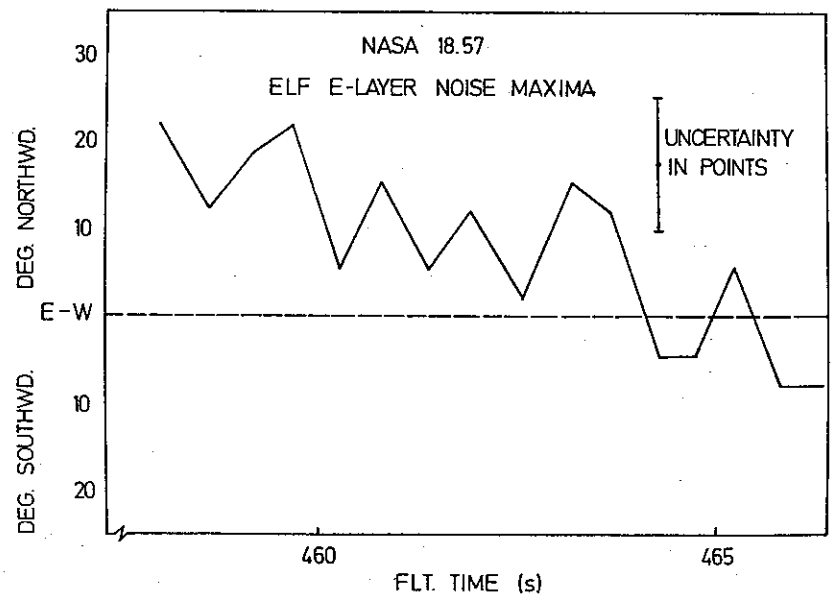

Fig. 2.12. Preliminary plot of direction of antenna in the maxima in the spin-modulated amplitude of ELF *E*-layer noise *vs.* flight time for the rocket NASA 18.57.

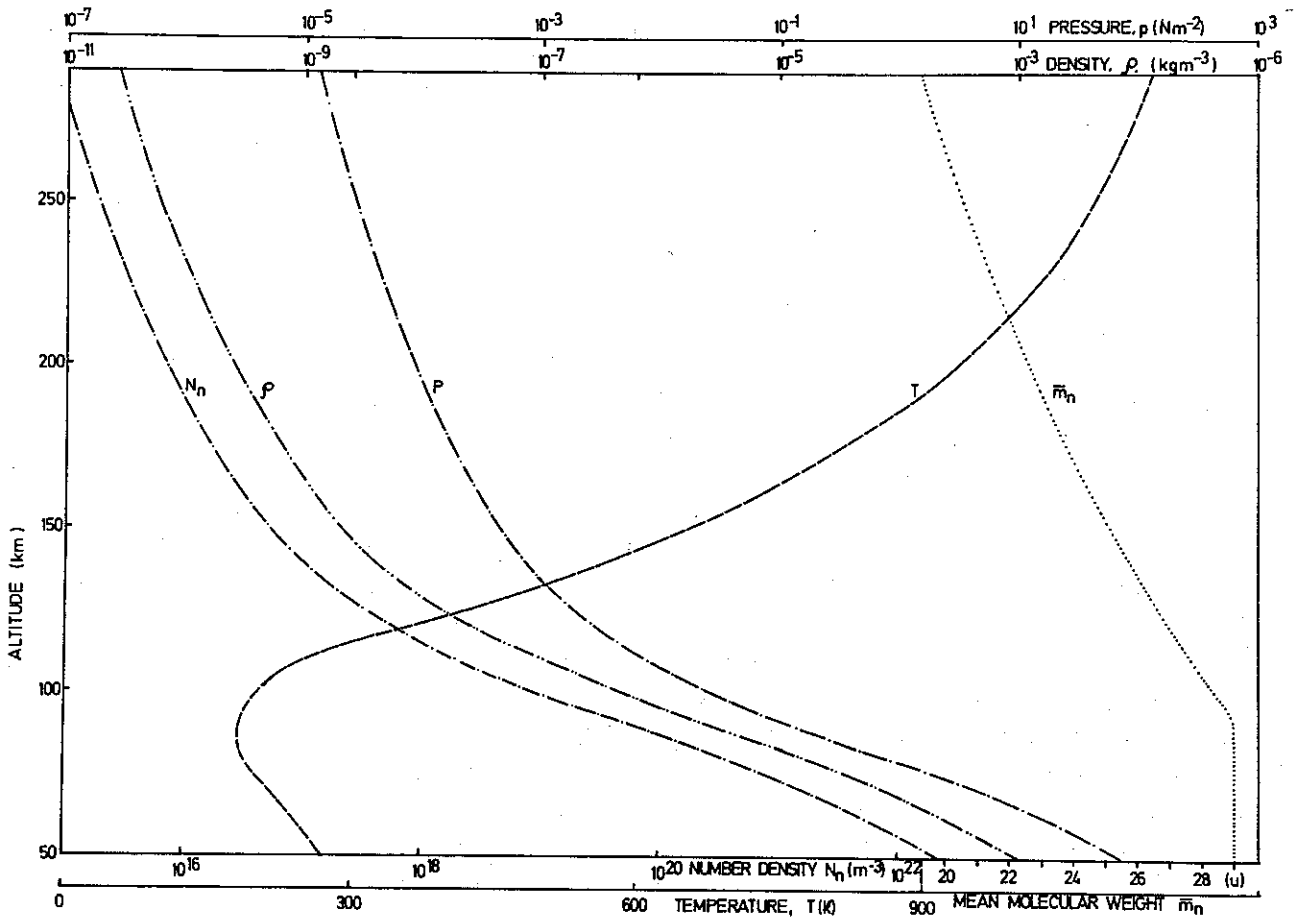

Fig. 3.1. Density (ϱ), pressure (p), number density (N_n), mean molecular weight ($\bar{m}_n$), and kinetic temperature (T_n) for the neutral constituents in a mean atmospheric model (CIRA, 1965).

the gases. Present knowledge about the upper atmosphere is far from satisfactory, especially concerning the minor constituents, some of which are very important for ion chemistry. Since we are more interested in the main features of the ionosphere than in ionic and molecular reactions, this will, however, not disturb our picture considerably. Furthermore, these components will mainly be of importance below 90 km, *i.e.* below the main region of interest in this context.

While direct measurements have given good information on the atmospheric properties up to say 60 km and fairly good up to about 90 km, the experimental data above 90 km are rather sparse. From the available information, standard atmosphere models have been defined; the most commonly used is the COSPAR International Reference Atmosphere Model 1965 (CIRA, 1965), even though this is no longer up to date. Figure 3.1. shows the vertical distribution of pressure, p, density, ϱ, total number density of neutral constituents, N_n, and mean molecular mass, $\bar{m}_n$, according to this model.

Up to about 80 km the major constituents are supposed to be present in constant proportions, so that the mean molecular mass will be constant. The dominating properties at these altitudes are: Nitrogen (N_2), which makes up about 78.1%, oxygen (O_2) 21.0%, and argon (A) 0.9%.

While turbulent convection gives a fairly homogeneous gas mixture up to about 80–90 km (the turbopause), there is a rather sudden change at this level, and photochemical dissociation and diffusive separation play the most important roles in disarranging the homosphere distribution above the turbopause.

Figure 3.2. shows the concentration of the total neutral density and the major neutral constituents above 90 km. In the E-region N_2 and O_2 are the two dominating molecules, but with increasing

altitude O will be more and more dominating. It should, however, be noted that these concentrations are rather poorly known.

3.2.2. *Transport in the upper atmosphere.* Irregular vertical transport, such as turbulence and eddy motion, is important for mixing the neutral constituents below 80 km. Eddy transport is also important for the H_2O budget of the ionosphere in bringing water vapour up from lower altitudes. Furthermore, turbulence will serve as an 'energy-sink', where larger-scale motions are degraded into small-scale turbulent motions and where the energy is finally lost as heat. Hines (1963) gives as typical parameters for small-scale motions at 80–90 km: size 20 m, velocity 0.5 m s^{-1}, time scale 40 s.

Horizontal transport includes large-scale wind systems. These may be set up by temperature differences, as large zonal wind systems, or driven by pressure gradients, due to daily temperature variations, or be caused by tidal oscillations, global in scale, with periods related to the solar and lunar days.

Smaller-scale effects can be caused by gravity waves with periods of minutes or hours, vertical wavelengths of a few km, and horizontal wavelengths up to thousands of km (Hines 1960). Local transports and irregularities can also be caused by sudden warmings of the lower ionosphere (*e.g.* Belrose 1967). In the *E*-region, large horizontal gradients in the wind velocity, wind shears, are frequently observed, often in connection with sporadic *E*-region ionization (*e.g.* Whitehead 1967).

3.3. *Production and loss of ionization*

The physical processes controlling the content of charged particles in the ionosphere can be divided into groups labelled production, destruction, and movement of ionization. A continuity equation for the variation of the density of species k, N_k, can be written as

$$\frac{\partial N_k}{\partial t} = q_k - l_k(N_k) - \nabla \cdot (N_k \mathbf{v}_d). \qquad (3.1)$$

The symbols q and l represent the production and loss, respectively, and $\mathbf{v}_d$ is the net drift velocity.

For the regions we are considering, *i.e.* below 200 km, the q and l terms dominate, and transport can usually be neglected or treated as a small perturbation. Furthermore, the time constants involved in the processes often make $\frac{\partial N}{\partial t} \ll q_k - l_k(N_k)$, and for slowly varying phenomena we can assume that the equation $q_k = l_k(N_k)$ is adequate.

The principal production process, at least at non-auroral latitudes, for creation of ion-electron pairs is generally accepted to be absorption of solar ultraviolet ($\lambda < 1340$ Å) and X-ray radiation. Although the electron production in the ionosphere involves rather complex processes, a quite good description of many of the main features can be obtained from a simplified theory developed by Chapman (1931). This theory gives a formula for production, q, as a function of height, h, and solar zenith angle, χ, (see *e.g*, Risbeth & Garriott 1969):

$$q(z,\chi) = \frac{\eta I_\infty}{eH} \exp\left[1 - z - e^{-z} \sec\chi\right]. \qquad (3.2)$$

η is the ionizing efficiency, *i.e.* number of electrons produced per photon absorbed, and z the reduced height $z = \frac{h - h_o}{H}$, h_o a reference height.

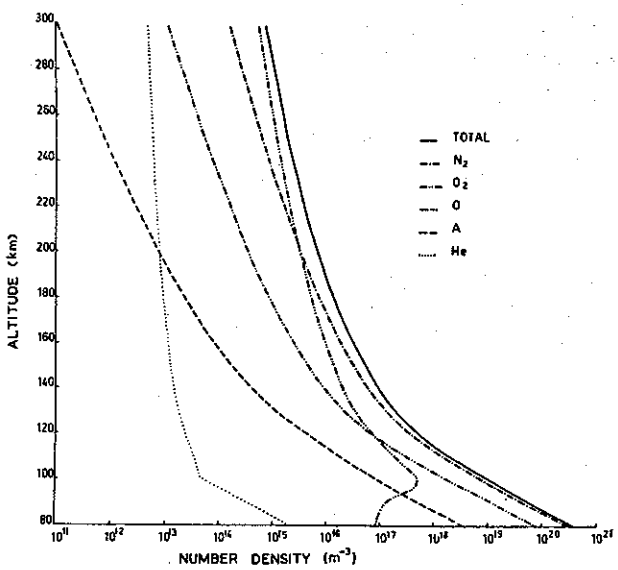

Fig. 3.2. Total density and densities of five major neutral constituents (N_2, O_2, O, A and He) as function of altitude for a mean atmospheric model (CIRA, 1965).

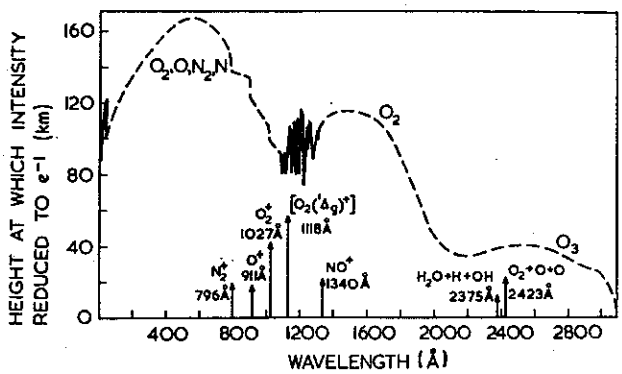

Fig. 3.3. Penetration depth of solar ultraviolet radiation. The curve shows the level where the intensity is reduced to e^{-1}. Wavelengths corresponding to the ionization potential for some important species are marked off (after Thomas 1972).

Several photochemical reactions will tend to neutralize or rearrange the ionization and will thus cause the necessary balance to the production process. The pertinent reactions can be listed as recombination, detachment/attachment, and ion-atom interchange (charge exchange). The most important loss reactions are outlined in Table 3.1. The symbols X,Y,Z, used in the reaction equations may denote either an atom or a molecule. (For more detailed information and references, see *e.g.* Bates 1970.)

To obtain photon-ionization of a species X, symbolized by $h\nu + X \rightarrow X^+ + e$, the photonenergy, $h\nu$, must exceed a critical value – the ionization potential of X. This energy threshold also defines a minimum frequency, or maximum wavelength, for the ionizing wave. In Table 3.2, the ionization potential and corresponding maximum wavelength for the most important ionospheric constituents are given. This, together with the penetration depth in the ionosphere for different wavelengths (Fig. 3.3), will define the processes which can possibly be caused by photon-ionization, if the composition of the neutral atmosphere and the radiation spectrum is known.

Table 3.2. Ionization potentials of the main molecules and atoms in the upper atmosphere and the corresponding upper limit of the wavelength of UV radiation capable of ionizing the species.

Constituent:	O_2	N_2	O	N	NO
Ionizing potential, eV	12.08	15.57	13.62	14.54	9.25
Maximum wavelength, Å	1027	796	910	853	1340

Using this we can deduce the following: The production in the lower *D-region* (<70 km) is caused by Lyman-α radiation and cosmic rays. The latter will also give rise to a weak night-time ionization. Between 70 and 80 km ionization of NO by Lyman-α is the most important contribution. In the upper part of the *D*-region (80–90 km), X-rays in the range 1–10 Å will cause ionization of the gases present. In addition, ionization of O_2 in the state ($^1\Delta_g$) by ultraviolet radiation is suggested as an important process (Henlen & McElroy 1968).

Recombination is believed to be the most important loss process in the *D*-region, at least

Table 3.1. Main reactions for loss of ionization

Recombination:	
Ion-ion	$X^+ + Y^- \rightarrow X + Y$
Electron-ion: Three-body	$X^+ + e + Z \rightarrow X + Z$
Radiative	$X^+ + e \rightarrow X + h\nu$
Dissociative	$XY^+ + e \rightarrow X + Y$
Detachment (→), attachment (←):	
Collisional d., three body a.	$X^- + Z \rightleftarrows X + e + Z$
Associative d., dissociative a.	$X^- + Y \rightleftarrows XY + e$
Photo d., radiative a.	$X^- + h\nu \rightleftarrows X + e$
Ion-atom interchange:	$X^+ + YZ \rightarrow XY^+ + Z$
	$X^+ + YZ \rightarrow YZ^+ + X$

during the day, but due to the presence of negative ions, the loss reactions at these altitudes are very complicated.

The predominant ions are NO^+, O_2^+, and, in the upper part, N_2^+. Water vapour complexes and negative ions are important for the chemistry in the region, but little is known about their concentrations.

The variations in the undisturbed daytime *E-region* can be described by a Chapman production function and with recombination as the dominating loss process. (This combination is often called an α-layer.) The ion production is mainly caused by photon-ionization from X-rays, 10–100 Å, and UV radiation in the 1000–1500 Å region. The chief ions are believed to be O_2^+, NO^+, N_2^+, and O^+. Recent rocket measurements have also shown that metallic ions may exist in appreciable quantities, often in very narrow layers (Chen & Harris 1971).

Although the general behaviour of the layer may be described by the α-layer function, a number of disparities have been observed. One of these is the existence of a night-time *E*-layer where the electron density does not fall below 10^9 m^{-3} (Chen & Harris 1971), while, according to the Chapman theory, the layer should vanish during night-time. This means that either the effective *E*-region recombination rate must change at night (Yonezawa 1968), or that a source of ionization exists. As a possible source for the night-time *E*-region, Lyman-β scattered to the dark side of the earth has been suggested (Swider 1965; Ogawa & Tohmatsu 1966). Transport effects, which to a great extent have been neglected in *E*-region studies, may also be responsible for several of the irregular features. However, the most important ionization source during disturbed conditions at high latitudes is found to be precipitating particles (see Sect. 3.4).

The ionization of the lower part of the *F-region* (150–200 km) is mainly caused by radiation in the range 170–910 Å, and the behaviour of the region is close to that of an α-layer. The primary ions are O^+ and N_2^+.

Table 3.3 and Figs. 3.4 and 3.5 give a summary of this section. The table lists the various production and loss processes and their importance in the different regions, while the figure gives the results of these reactions, *i.e.* the densities of the most important charged species in the lower ionosphere.

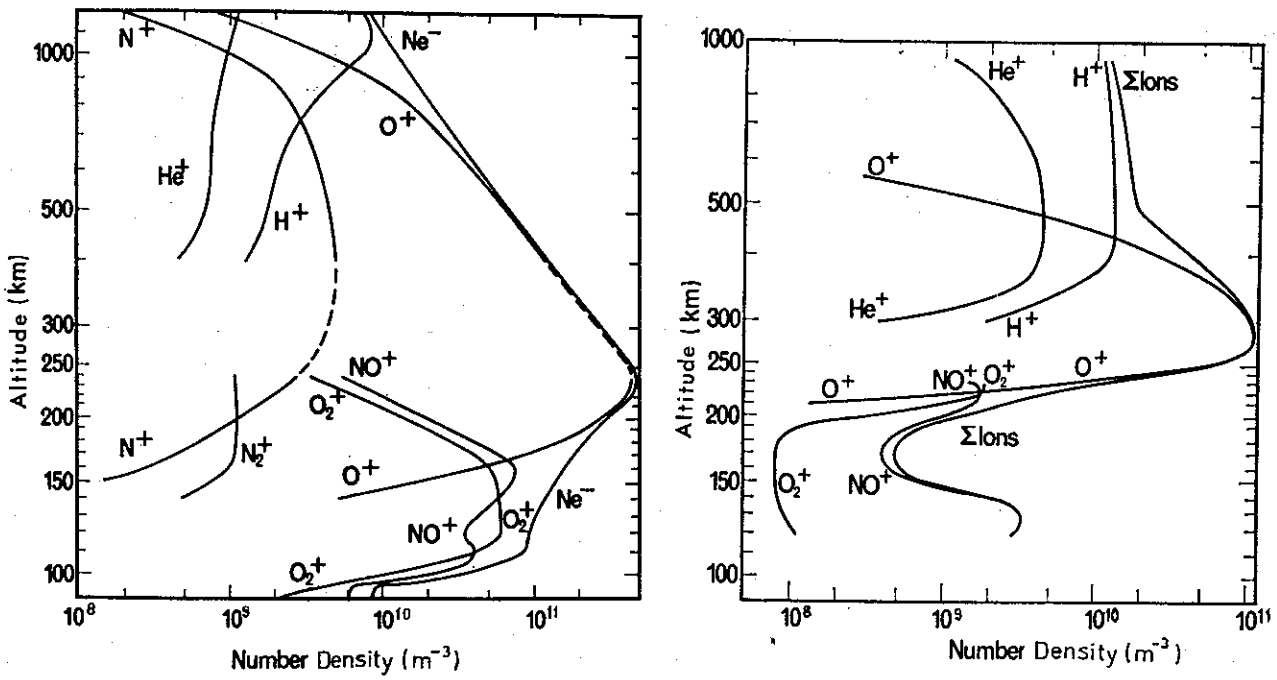

Fig. 3.4. Ionic composition of IQSY daytime (left) and night-time (right) ionosphere above 100 km (after Johnson 1969).

Table 3.3. Production and loss functions in the ionosphere

Process	Contribution to Eq. 3.1.	*D*-region Approx. 50–90 km	*E*-region Approx. 90–150 km	*F1*-region Approx. 150–200 km
PRODUCTION				
Solar photon-ionization	$q(h)$	Ly-α(1216 Å) $\rightarrow$ NO X-rays (1–10 Å) $\rightarrow$ N_2, O_2 UV(1027–1118 Å) $\rightarrow$ $O_2(^1\Delta_g)$	Ly cont. (800–910 Å) $\rightarrow$ N_2, O_2 Ly-β (1026 Å) $\rightarrow$ O_2 UV($\lambda < 1027$ Å) $\rightarrow$ O_2, N_2, O X-rays (10–170 Å)	EUV (170–911 Å) $\lambda < 910$ Å $\rightarrow$ O $\lambda < 796 \rightarrow N_2$
Ionization by particles (Mostly at high latitudes)	$q(h)$	Electrons > 30 keV Protons > 2MeV (PCA) Cosmic rays	Electrons 1–30 keV Very important	Electrons $\lesssim$1 keV (most important at night)
LOSS				
Ion-ion recombination	$\alpha N_+ N_-$	Important	Few. neg ions	Neg. ions can be neglected
Electron-ion recomb.				
Three-body	$\alpha_e N_+ N_e$	Important	Insignificant	Not important
Radiative	$\alpha_e = \alpha_e(h)$	Insignificant	Not important	Not important
Dissociative		Important	Principal loss mech.	Principal loss mech.
Attachment	$\beta_{eff} N_e$	Important	Can maintain some neg. ions at night	Weakly involved
Radiative				
Three body		Most important		
Dissociative				
Detachment	$\delta(h) N_e, \kappa N_-$			
Collisional				
Associative		Important	Weakly involved	Insignificant
Photo		Important, causes day/night change of N_-/N_e	Effective by day	Causes absence of neg. ion
Ion-atom interchange	$\gamma(h) N_+$	Weakly involved	Important	Important

3.4. *Ionization by precipitating particles*

Energetic particles precipitating into the atmosphere collide with neutral atoms and molecules and gradually lose their energy to these. A part of this energy goes to ionization – and excitation – of the neutral air. The approximate penetration depths for protons and electrons as a function of energy are shown in Fig. 3.6. As the collision process, and thus the penetration, is a statistical process, the values in this figure should be considered as average heights where most of the energy of the primary particles is lost. It can be seen that only electrons and protons with initial energies greater than 20 and 200 keV, respectively, can cause ionization at *D*-region altitudes. The *E*-region will mainly be influenced by 0.5–10 keV electrons and 10–200 keV protons, while the *F*-region ionization mainly comes from electrons with energy less than 1 keV. Figure 3.7. shows the energy loss rate for electrons with initial energy 6 keV as a function of altitude. It is seen that these particles lose almost all their energy within the *E*-region.

At low and medium latitudes only the *D*-region seems to be affected by ionization from precipitating particles (Whalen *et al.* 1971). This is also in accordance with the statistical picture of the particle spectrum *vs.* latitude (*e.g.* Søraas 1973).

While particle ionization at these latitudes plays a minor role, in the auroral zone during disturbed conditions it may be the main source of ionization. The energy spectrum of the precipitating particles on the night side of the auroral oval implies that the ionization will normally be most enhanced in the *E*-region and upper *D*-region; *i.e.* from approximately 80 to 150 km (Hultqvist 1972). Here the peak electron density may typically increase from say 10^{9-10} m^{-3} during quiet conditions to 10^{12} m^{-3} during an auroral event (McNamara 1969).

On the dayside, precipitating particles will mainly cause ionization in the *D*- and *E*-region equatorwards of the auroral oval, while the particle spectrum on the dayside of the oval, the polar cusp, is considerably softer, with a correspondingly increased altitude for the ionization. Inside the polar cap the particle spectrum is basically soft, and during normal conditions only the upper ionosphere will be affected by precipitation ionization.

This pattern will be changed by irregular and sporadic precipitation and during precipitation events with great fluxes of high energy particles (*e.g.* Polar Cap Absorption (PCA) events) when significant ionization can be present in the lower *D*-region from the polar cap to $\Lambda \sim 50°$.

To conclude it can be said that ionization by

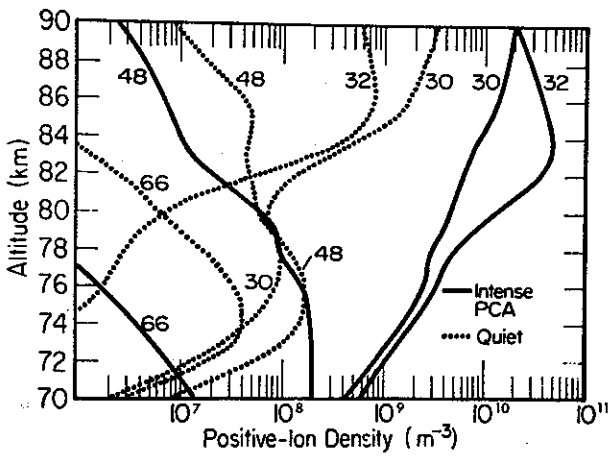

Fig. 3.5.a. Altitude profiles for molecular positive ions and hydrates during quiet and intense PCA conditions (after Reid 1972). Mass identifications are: 30 = NO^+, 32 = O_2^+, 48 = $NO^+ \cdot H_2O$, 66 = $NO^+ \cdot 2(H_2O)$.

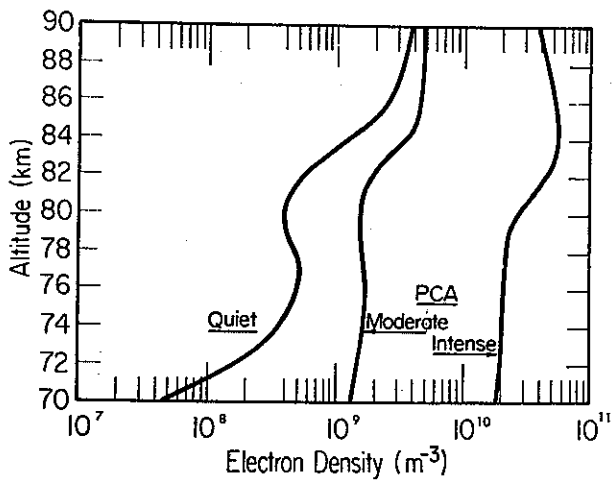

Fig. 3.5.b. Electron concentrations below 90 km during quiet conditions and during moderate and intense PCA conditions (after Reid 1972).

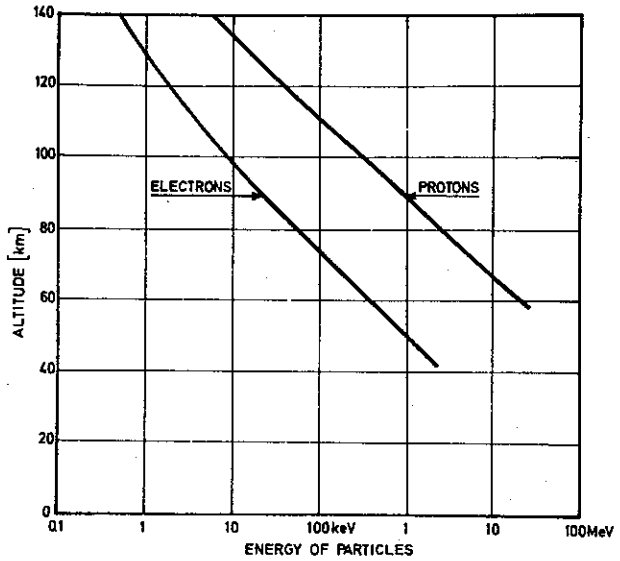

Fig. 3.6. Penetration depths in the earth's atmosphere as function of particle energy for vertically incident electrons and protons (after Mæhlum 1973).

particles plays a very important role in the production of the high latitude ionosphere, especially in the auroral *E*-region. Because of the great variations, both in time and space, which are present in the particle fluxes, this will involve large fluctuations in both the electron density and its altitude distribution.

3.5. *Ionospheric parameters*

In addition to composition and density several other parameters which can be measured directly or otherwise calculated are important in describing the behaviour of the plasma.

3.5.1. *Temperatures of the ionospheric constituents.* In dealing with ionospheric plasma it is necessary to distinguish between the temperature of the neutrals, T_n, and electron and ion temperatures, T_e and T_i. Assuming a Maxwellian velocity distribution, temperature is usually defined in terms of the mean energy, $E = \frac{3}{2}\kappa T$, where $\kappa =$ Boltzmann's constant.

It is widely accepted that up to 120–130 km thermal equilibrium is established, *i.e.* $T_e = T_i = T_n$, during undisturbed conditions. The numerical values of the temperature are, however, subjected to daily and latitudinal variations. At greater altitudes selective heating (Bowhill & Geisler 1966) and reduced collision rates lead to temperature differences, so that $T_e > T_i > T_n$. As energy transfer through collisions is most effective among particles of equal masses, the T_i and T_n curves will separate at higher altitudes than those for T_e and T_n. Figure 3.8 shows the altitude variation of T_n after CIRA (1965) and reasonably representative curves for T_i and T_e according to Evans & Mantas (1968) for quiet conditions. The picture, with $T_e \approx T_i$ in the *D*- and lower *E*-region, will be considerably changed, especially at high latitudes, during disturbed conditions (*cf.* the T_d-curves in Fig. 3.8). Precipitation of energetic particles will not only cause in-

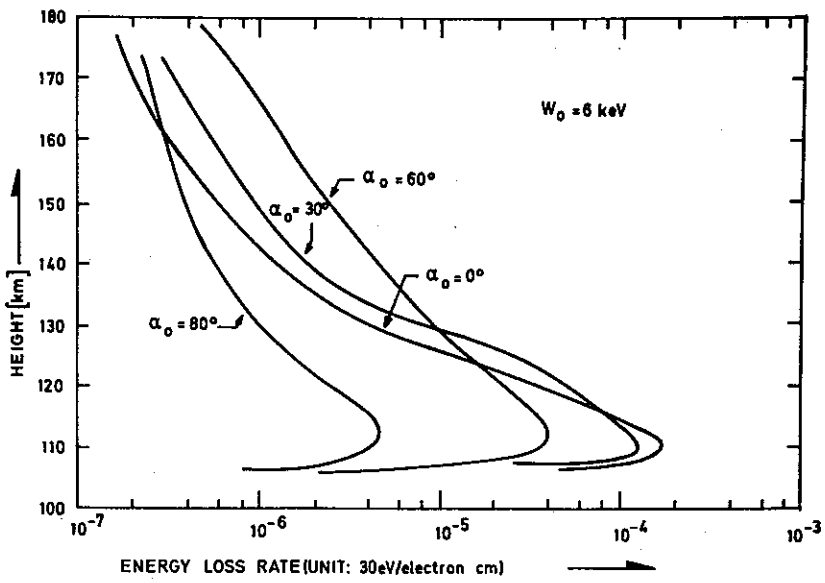

Fig. 3.7. Energy loss rate profiles for electrons with initial energy 6 keV and with impact angle α (after Wedde 1970).

creased temperatures at the penetration altitudes, but also change the ratio T_e/T_i, and lower the altitude where this ratio becomes larger than one (*cf. e.g.* McNamara 1969).

3.5.2. *Collision frequencies.* Collision processes are very important in the ionospheric plasma both for energy transfer and because they will have influence on and modify several of the other plasma parameters. In the study of ionospheric irregularities, collisions are involved both in the generation and motion of the irregularities, and it is therefore necessary to have information about variations in the collision rates for the various species. A thorough discussion of collision phenomena in atmospheric gases is very complicated and beyond the scope of this paper. However, for most applications simplified methods can be used.

Under the term 'collision' several processes involving energy transfer between particles, such as elastic ('classical') collisions, scattering in a Coulomb field, ionization, dissociation, excitation of particular states, *etc.*, can be involved. For a constituent, k_1, each interaction process, γ, has a specific cross section, $\sigma_{k_1k_2}(\gamma, v)$, which is also a function of velocity, v, and target particle, k_2, with its corresponding collision frequency, $\nu_{k_1k_2}$. In ionospheric studies it is convenient to introduce a weighted cross section, $\sigma^m_{k_1k_2}$, where change in momentum transfer with scattering angle is taken into account, and a corresponding 'momentum transfer collision frequency', $\nu^m_{k_1k_2}$. As the cross sections depend on the velocity, 'effective' collision frequencies, $\langle \nu^m_{k_1k_2} \rangle$, are obtained by averaging over the velocity distribution.

The collision processes which will predominate in this context are:

i) Elastic collisions between electrons and neutrals, $\langle \nu^m_{en} \rangle$.
ii) Elastic collisions between ions and neutrals, $\langle \nu^m_{in} \rangle$.
iii) Coulomb collisions between electrons and ions, $\langle \nu^m_{ei} \rangle$.

From a general expression of the rate of energy transfer between two gases with Maxwellian velocity distributions (Desloge 1962), Banks (1966 *a*, *b*) derived the following expression for the average momentum transfer collision frequency between species k_1 and k_2

$$\langle \nu^m_{k_1k_2} \rangle = \tfrac{4}{3} N_{k_2} \left(\frac{8\kappa}{\pi} \right)^{1/2} \left[\frac{T_1}{m_1} + \frac{T_2}{m_2} \right]^{1/2} \bar{Q}_m, \quad (3.3)$$

where $\bar{Q}_m$, the average momentum transfer cross section for the reaction between k_1 and k_2 is defined as:

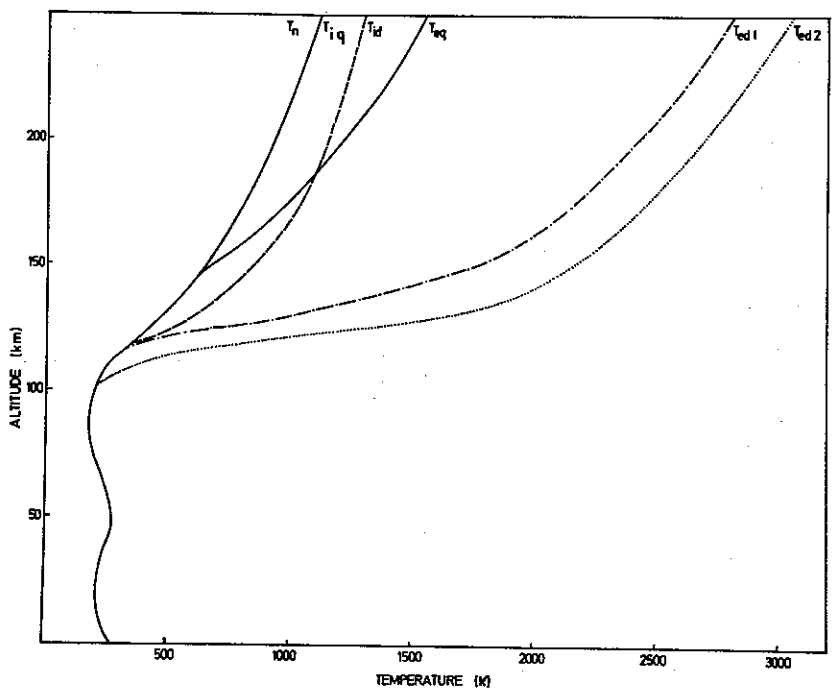

Fig. 3.8. Height profiles for ionospheric temperatures. T_n is the temperature of neutral constituents (after CIRA 1965), T_{eq} and T_{iq} the electron and ion temperatures for quiet conditions (after Evans & Mantas 1968). T_{ed1} and T_{id} are electron and ion temperatures for moderately disturbed conditions and T_{ed2} electron temperatures for strong disturbance (after Walker & Rees 1968).

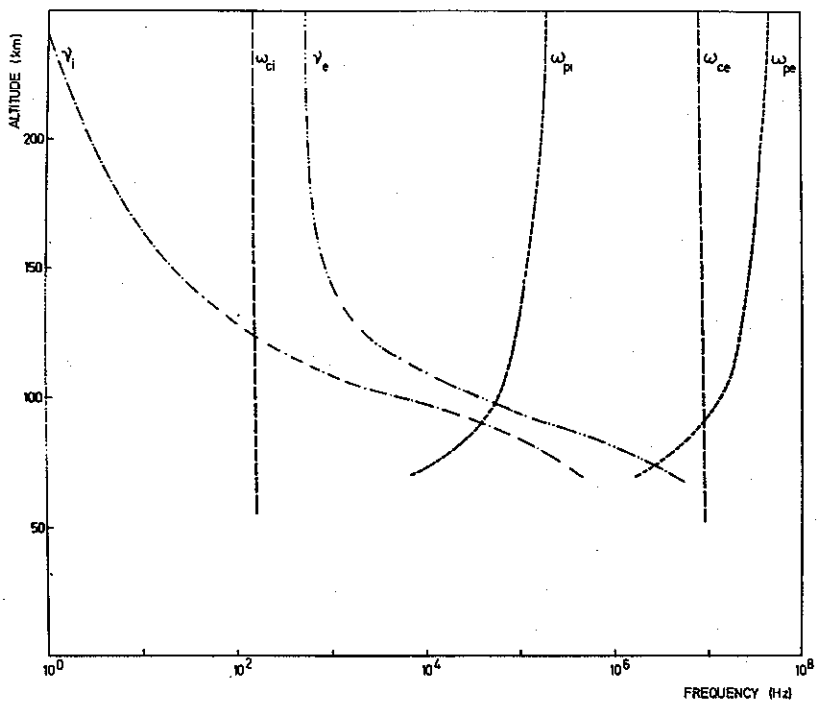

Fig. 3.9. Variations with altitude of electron and ion collision frequency (ν_e and ν_i), electron and ion gyro frequency (ω_{ce} and ω_{ci}) and electron and ion plasma frequency (ω_{pe} and ω_{pi}) calculated for a mean model ionosphere.

$$\bar{Q}_m = K^3 \int_0^\infty v^5 \, \sigma^m_{k_1 k_2} \exp(-Kv^2) dv, \qquad (3.4)$$

with

$$K = \left[\frac{2\kappa T_1}{m_1} + \frac{2\kappa T_2}{m_2}\right]^{-1}.$$

For the lower ionosphere, where our main interest is directed, rough numerical values for the collision frequencies can be obtained from the simplified expressions (Boström 1972)

$$\{\nu_{en}\} = 1.5 \cdot 10^{-17} \{N_n\} \{T\}, \qquad (3.6)$$

$$\{\nu_{ei}\} = [59.0 + 1.82 \, ln(\{T^3\}/\{N_e\})] \cdot 10^{-6} \{N_e\} \{T^{-3/2}\}, \qquad (3.7)$$

$$\{\nu_{in}\} = 4.2 \cdot 10^{-16} \{N_n\}. \qquad (3.8)$$

These are only numerical equations, and symbols in { } represent the values of the various parameters measured in the SI system.

The relative importance of the two different collision processes for electrons will vary with altitude according to variations in composition and temperatures. In an attempt to appreciate the relative importance of electron-neutral and electron-ion collisions, Banks (1966*a*) found that the latter will make a significant contribution to the total collision frequency when $\frac{N_+}{N_n} > \frac{T_e^2}{1.3 \cdot 10^{11}}$. From the values of densities and temperatures given earlier in this chapter it is found that electron-ion collisions will be important in the upper part of the *E*-region and above this region.

Collision frequencies calculated from Eqs. (3.6), (3.7), and (3.8) using ionospheric parameters given earlier in this chapter, are shown in Fig. 3.9.

3.5.3. *Characteristic frequencies and dimensions in the ionospheric plasma.* The introduction of a magnetic field, *B*, will influence the plasma in several ways. The first detectable effect is that it will cause a gyrating motion of the charged particles, the frequency of which is given by

$$\omega_{ck} = \frac{Z_k e B}{m_k}. \qquad (3.9)$$

The ratio ω_{ck}/ν_k indicates whether the particle motion is dominated by the magnetic field or if collision processes play the most important role. Figure 3.9 gives the altitude variation of the gyro frequency for electrons and an ion with mass 30 together with the collision frequencies for the same species as a function of altitude. The

magnetic field for an auroral station (Tromsø) has been used in the ω_{ck} calculations.

Another characteristic frequency is the so-called plasma frequency, defined by

$$\omega_{pk} = \left(\frac{N_k Z_k^2 e^2}{\varepsilon_o m_k}\right)^{1/2}. \tag{3.10}$$

The magnitude of the plasma frequency characterizes the rate at which the electrostatic restoring forces in a plasma eliminate deviations from neutrality. The height variation of the ionospheric electron and 'mass-30-ion' plasma frequency is also shown in Fig. 3.9.

Fig. 3.10 gives the magnitudes of several length parameters pertaining to the ionospheric plasma. They will be defined in the following.

The radius of the gyrating motion of a k-particle, the cyclotron radius (or Larmor radius) r_{ck}, is

$$r_{ck} = \frac{v_\perp}{\omega_{ck}} = \frac{v_\perp m_k}{Z_k e B} \tag{3.11}$$

where $v_\perp$ is the component of the particle velocity transverse to the magnetic field. On average, if the velocity distribution is isotropic, $v_\perp$ can be set equal to the mean thermal velocity for Maxwellian distribution, and the following expression for the mean cyclotron radius is obtained

$$\langle r_{ck}\rangle = \left(\frac{8 m_k \kappa T_k}{\pi Z_k^2 e^2 B^2}\right)^{1/2}. \tag{3.12}$$

A k-particle moving with velocity v_k will on the average move a distance $\frac{v_k}{\nu_k}$ between each collision. This distance, the mean free path, λ_{vk}, will for a Maxwellian velocity distribution not correspond exactly to the expression obtained when putting $v_k = \langle v_k\rangle$. One will instead get (Morse 1964)

$$\lambda_{vk} = \left(\frac{\pi \kappa T_k}{2 m_k \nu_k^2}\right)^{1/2}. \tag{3.13}$$

As for the ratio ω_{ck}/ν_k, the ratio r_{ck}/λ_{vk}, will contain information about the influence of the magnetic field relative to collisions on the particle motion. If, for instance, $r_{ck}/\lambda_{vk} \ll 1$, trajectories of the k-particles can be regarded as almost straight lines between consecutive collisions without being significantly affected by the magnetic field, and the diffusion in the plasma can be considered isotropic.

The length parameter corresponding to the plasma frequency is the Debye length, λ_D, which for a non-isothermal plasma is defined as (see Frank–Kameneski 1967)

$$\lambda_D = \left[\frac{e^2}{\varepsilon_o \kappa}\left(\frac{\sum_i Z_i^2 N_i}{T_i} + \frac{N_e}{T_e}\right)\right]^{-1/2}. \tag{3.14}$$

Subscripts i refer to ions of type i, and a summation is made over all ionic species.

In application, the effects from the ions are usually neglected, and this gives the following simple expression for the Debye length:

$$\lambda_D = \left(\frac{\varepsilon_o \kappa T_e}{e^2 N_e}\right)^{1/2} = \left(\frac{\kappa T_e}{m_e}\right)^{1/2} \frac{1}{\omega_{pe}}. \tag{3.15}$$

The Debye length is thus the distance a particle with velocity $\left(\frac{\kappa T_e}{m_e}\right)^{1/2}$ will travel within a time interval $\frac{1}{\omega_{pe}}$. This velocity is frequently used as the electron thermal velocity instead of the mean velocity in the Maxwell distribution, $\left(\frac{8}{\pi}\frac{\kappa T_e}{m_e}\right)^{1/2}$.

The Debye length is also often called the 'Debye

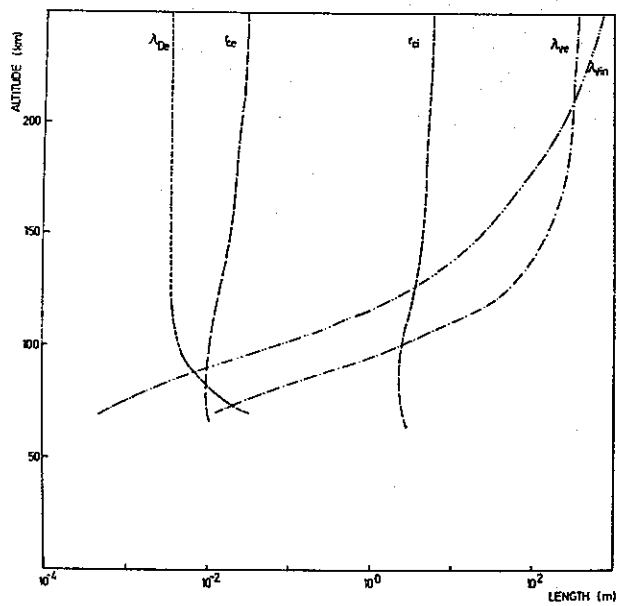

Fig. 3.10. Altitude profiles of electron and ion gyroradius (r_{ce} and r_{ci}), electron and ion mean free path (λ_{ve} and λ_{vi}), and electron Debye length (λ_{De}) for a mean model ionosphere.

shielding distance'. The charged particles in a plasma have a tendency to rearrange themselves in such a way as to shield any electrostatic fields due either to a surface at some non-zero potential or to a charge within the plasma. In the 'classical' approach it appears that this rearrangement of charged particles effectively cancels out any electrostatic fields within a distance of the order of λ_D. However, in several cases, for instance in a plasma far from thermal equilibrium, the Debye length is not always well defined, and it has also been shown (Öpik 1965) that the effective shielding in practical circumstances may deviate considerably from the classical Debye length.

4. ELECTRODYNAMICS OF THE IONOSPHERE

4.1. *Introduction*

The introduction of an electric field in the ionosphere will set charged particles into motion, and cause a drift of the ionization as a whole as well as of ionization irregularities, and electric currents will be flowing. However, the relation between the direction and magnitude of the field and the resulting particle velocity is not a simple one, as effects caused by the magnetic field and collisions will give different mobilities in different directions. In this chapter we will not discuss the origin of the electric field, but just postulate its presence and see how the motion of the charged species is influenced.

Instead of starting out with the equations of motion and calculate the mobility of the particles, we will follow a more qualitative, physical derivation, making use of a procedure given by *e.g.* Baker & Martyn (1953), Ratcliffe (1959*a*), and Boström (1973). This method has the advantage that it more easily gives an impression of how variations of the different parameters result in changes in directions and magnitudes of velocities and currents.

4.2. *Particle motions and conductivities*

In the presence of a magnetic field an electric field is defined only with reference to a coordinate system. From one frame of reference to another both **E** and **B** will change according to Lorentz transformations (*cf. e.g.* Møller 1952). If we operate in a coordinate system where the electric and magnetic fields are **E** and **B**, an object with velocity **v** will experience a field **E′**, given by

$$\mathbf{E}' = \mathbf{E} + \mathbf{v} \times \mathbf{B}, \tag{4.1}$$

in non-relativistic formulation. This field will cause a drift of the particles which in turn will give rise to an electric current. In analogy to the simple Ohm's law for the current density in a linear conductor, one can introduce a 'generalized Ohm's law'

$$\mathbf{j} = \underset{\sim}{\sigma}(\mathbf{E} + \mathbf{v} \times \mathbf{B}). \tag{4.2}$$

Here the conductivity, σ, is a tensor, where the tensor elements depend on the mobility of the particles.

Between collisions the motion of a k-particle will only be affected by the electric and magnetic field, and its equation of motion will be

$$m_k \frac{d\mathbf{v}_k}{dt} = q_k(\mathbf{E} + \mathbf{v}_k \times \mathbf{B}). \tag{4.3}$$

If the collision frequency is ν_k the probability of a collision taking place in the time interval from t to $t+dt$ will be $\nu_k \exp[-\nu_k t]dt$. From the equation of motion the velocities in the collisionless case can be found, and from this also the mean velocity components when collisions are taken into account (*cf. e.g.* Boström 1973). In the case where **B** is directed along the negative z-axis and **E** is in the xz-plane these are

$$v_{kx} = \frac{\varepsilon_k \nu_k \omega_{ck}}{\nu_k^2 + \omega_{ck}^2} \frac{E_x}{B}, \tag{4.4a}$$

$$v_{ky} = \frac{\omega_{ck}^2}{\nu_k^2 + \omega_{ck}^2} \frac{E_x}{B}, \tag{4.4.b}$$

$$v_{kz} = \frac{q_k}{m_k \nu_k} E_z. \tag{4.4.c}$$

Taking the motion of the neutral gas into account, Eqs. (4.4) can be presented in the more general form

$$\mathbf{v}_k - \mathbf{v}_n = \frac{\varepsilon_k \nu_k \omega_{ck}}{\nu_k^2 + \omega_{ck}^2} \frac{\mathbf{E}_\perp + \mathbf{v}_n \times \mathbf{B}}{B} + \frac{\omega_{ck}^2}{\nu_k^2 + \omega_{ck}^2} \frac{(\mathbf{E}_\perp + \mathbf{v}_n \times \mathbf{B}) \times \mathbf{B}}{B^2} + \frac{q_k}{m_k \nu_k} \mathbf{E}_\parallel. \tag{4.5}$$

Subscripts $_\perp$ and $_\parallel$ refer to components perpendicular and parallel to the magnetic field, and $\varepsilon_k \equiv q_k/|q_k|$.

The difference between the electron and ion velocities will result in an electric current. Assuming charge neutrality and neglecting effects from negative ions, *i.e.* setting $N_e = N_i$, the current density becomes

$$\mathbf{j} = N_e\, e(\mathbf{v}_i - \mathbf{v}_e). \tag{4.6}$$

Combination of Eqs. (4.2) and (4.5) gives the following expression for the current density:

$$\mathbf{j} = \sigma_p(\mathbf{E}_\perp + \mathbf{v}_n \times \mathbf{B}) + \sigma_H\, \mathbf{B} \times (\mathbf{E}_\perp + \mathbf{v}_n \times \mathbf{B})/B + \sigma_\parallel \mathbf{E}_\parallel\,. \tag{4.7}$$

The conductivity tensor has thus the form

$$\underset{\sim}{\sigma} = \begin{pmatrix} \sigma_P & \sigma_H & 0 \\ -\sigma_H & \sigma_P & 0 \\ 0 & 0 & \sigma_\parallel \end{pmatrix} \tag{4.8}$$

The three different tensor elements, σ_P, σ_H and $\sigma_\parallel$, called the Pedersen, Hall, and parallel conductivity, respectively, are found to be

$$\sigma_P = \left(\frac{\nu_e \omega_{ce}}{\nu_e^2 + \omega_{ce}^2} + \frac{\nu_i \omega_{ci}}{\nu_i^2 + \omega_{ci}^2}\right) \frac{eN_e}{B}, \tag{4.9.a}$$

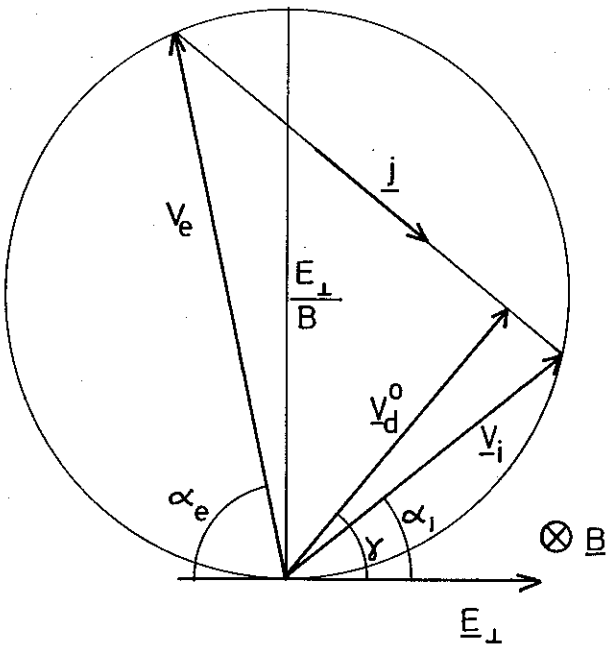

Fig. 4.1. Graphical construction of direction and magnitudes of drift velocities of electrons ($\mathbf{v}_e$) and ions ($\mathbf{v}_i$) due to an electric field $E_\perp$. The resulting current is in the direction of $\mathbf{j}$, neutral ionization drift in the $\mathbf{v}_d^0$ direction.

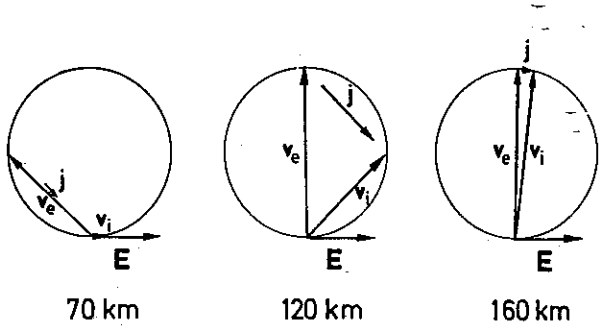

Fig. 4.2. The direction of the drift velocities and electric current, $\mathbf{j}$, relative to the electric field, $\mathbf{E}$, at three different heights of the ionosphere (Boström 1973).

$$\sigma_H = \left(\frac{\omega_{ce}^2}{\nu_e^2 + \omega_{ce}^2} - \frac{\omega_{ci}^2}{\nu_i^2 + \omega_{ci}^2}\right) \frac{eN_e}{B}, \tag{4.9b}$$

$$\sigma_\parallel = \left(\frac{1}{m_e \nu_e} + \frac{1}{m_i \nu_i}\right) e^2 N_e\,. \tag{4.9.c}$$

The perpendicular conductivities, σ_P and σ_H, appear as a result of the collisions and will be related to currents parallel (σ_P) and perpendicular (σ_H) to $\mathbf{E}_\perp$. On the other hand, collisions will reduce $\sigma_\parallel$.

The directions and magnitudes of the transverse velocities and current may be visualized as in Fig. 4.1. The magnetic field is directed into the paper plane, and the x-axis is in the direction of $\mathbf{E}_\perp$. The velocity vectors will then form the angles $\alpha_k = \arctan \frac{v_{ky}}{v_{kx}}$ with the x-axis. From Eqs. (4.4) these are found to be

$$\alpha_k = \arctan \frac{\omega_{ck}}{\nu_k}\,. \tag{4.10}$$

The diameter of the circle circumscribing the triangle formed by the vectors $\mathbf{v}_e$ and $\mathbf{v}_i$ is

$$D = \frac{v_k}{\sin \alpha_k} = \frac{v_k^2}{v_{ky}} = \frac{E_\perp}{B}, \tag{4.11}$$

and the velocities can thus also be expressed as

$$v_k = \frac{E_\perp}{B} \sin \alpha_k\,. \tag{4.12}$$

The current will be in the direction of the line between the arrowheads of $\mathbf{v}_e$ and $\mathbf{v}_i$.

In this way we can, by making a circle with diameter $\frac{E_\perp}{B}$ and drawing two chords in the directions α_e and α_i, get an impression of the

motion of the charged particles and the direction and magnitude of the current density.

Figure 4.2 shows these properties for three different heights. It can be seen how the directions, with a constant electric field, will change, corresponding to a change in the ratio between the Pedersen and Hall conductivities. In Fig. 4.3 the variation of the conductivities for a normal nighttime ionosphere, based on parameters given in Chapter 3, is plotted. From these two figures it can be seen that at *E*-region altitudes the current is mainly a Hall current. The shift in the ratio between the perpendicular conductivities is important in the study of ionospheric currents (*cf.* Chapter 5) and irregularities (Chapter 8).

Figure 4.3 also shows that except for the lowest part of the ionosphere the parallel conductivity, $\sigma_\parallel$, is much higher than the perpendicular components, and consequently $\mathbf{E}_\perp \gg \mathbf{E}_\parallel$. This means that at high latitudes, where the geomagnetic field lines are nearly vertical, the ionospheric layers are effectively coupled together, so that large-scale electric fields will spread in altitude without significant damping. Horizontal electric fields will thus become almost height independent.

Under such conditions it is meaningful to define a height-integrated linear current density as

$$\mathbf{J}_\Sigma = \int \mathbf{j}\, dh\,. \tag{4.13}$$

Provided $\mathbf{v}_n$ is height independent or negligible, integration of Eq. (4.7) gives

$$\mathbf{J}_\Sigma = \Sigma_P(\mathbf{E}_\perp + \mathbf{v}_n \times \mathbf{B}) + \Sigma_H \mathbf{B} \times (\mathbf{E}_\perp + \mathbf{v}_n \times \mathbf{B})/B\,, \tag{4.14}$$

where

$$\Sigma_P = \int \sigma_P\, dh, \text{ and } \Sigma_H = \int \sigma_H\, dh\,, \tag{4.15}$$

are known as the height-integrated conductivities.

It should be noted that the above only concerns DC conductivities. When it comes to small-scale electric fields and AC conductivities, the situation is quite different – drastic damping occurs for fields with horizontal scale of 1 km or less (Spreiter & Briggs 1961).

It is furthermore supposed that particle motions and currents are unlimited in all directions. In cases where currents are prevented from flowing in the directions associated with the primary electric field, secondary polarization fields can arise and cause an enhanced effective conductivity (*cf. e.g.* Boström 1972).

4.3. *Drift motion of ionization irregularities*

The drift velocities of electrons and ions, $\mathbf{v}_e$ and $\mathbf{v}_i$, which are caused by the imposed electric field, will have a common component, $\mathbf{v}_d^o$, in the direction γ with the field (*cf.* Fig. 4.1). This velocity, which is called the neutral ionization drift, is perpendicular to both **B** and **j**. By use of Fig. 4.1 we find

$$v_d^o = v_e \sin \alpha_i = \frac{E_\perp}{B} \sin \alpha_i \sin \alpha_e\,, \tag{4.16}$$

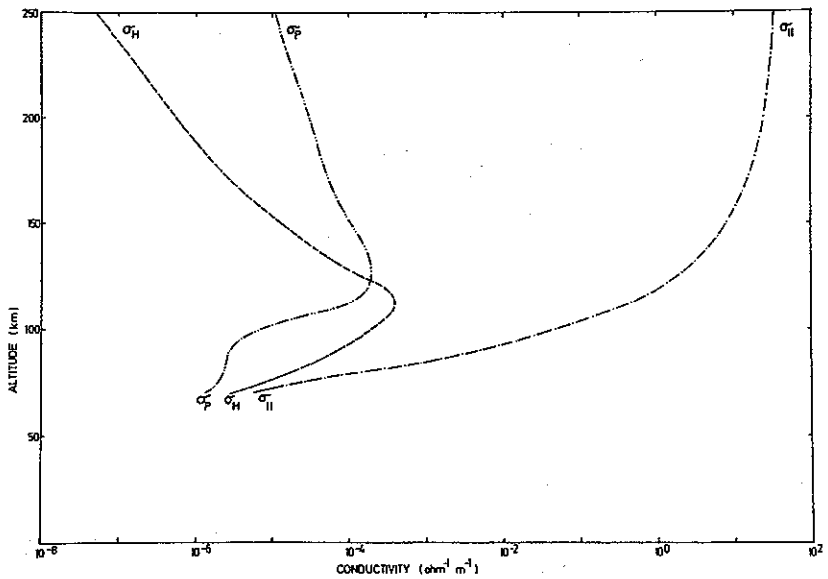

Fig. 4.3. Variation of the ionosphere conductivities with height for the mean ionospheric model used in Chapter 3.

and

$$\gamma = \frac{\pi}{2} - \alpha_e + \alpha_i \,. \tag{4.17}$$

Supposing that the driving Ampere force, $\mathbf{j} \times \mathbf{B}$, balances the collisional friction, one will obtain further

$$\mathbf{v}_d^o = \frac{\mathbf{j} \times \mathbf{B}}{N_e(m_e \nu_e + m_i \nu_i)} \,. \tag{4.18}$$

Although this neutral ionization drift, which denotes the drift of an uniformly distributed ionization, has a well-defined physical meaning, it is not easily measured. Another quantity which is more readily traced, and therefore of more practical interest, is the motion of an ionization irregularity, where the boundaries are defined by gradients in N_k. This has been studied by, for example, Kato (1963, 1964), whose method will be used in the following.

The drift velocity of the irregularity can be composed of two parts, one perpendicular to $\mathbf{j}$ corresponding to the neutral ionization drift, and one along $\mathbf{j}$. If displacement currents are neglected, $\nabla \times \mathbf{B} = \mu \mathbf{j}$ and consequently $\nabla \mathbf{j} = 0$. The variation of electron density due to the motion is then

$$\begin{aligned} \frac{\partial N_e}{\partial t} &= -\frac{\nabla \cdot (\mathbf{j} \times \mathbf{B})}{m_e \nu_e + m_i \nu_i} \\ &= -\frac{1}{m_e \nu_e + m_i \nu_i} [\mathbf{B} \cdot (\nabla \times \mathbf{j}) - \mu \mathbf{j}^2] \,. \end{aligned} \tag{4.19}$$

(Density variations due to production and loss processes, see Chapter 3, will in the following be neglected.)

If we only consider the motion in a plane perpendicular to $\mathbf{B}$ the current is expressed as

$$\mathbf{j} = \sigma_P \mathbf{E} + \sigma_H \frac{\mathbf{B} \times \mathbf{E}}{B} \,. \tag{4.20}$$

From this one obtains

$$\begin{aligned} \mathbf{B} \cdot (\nabla \times \mathbf{j}) &= [\sigma_P (\mathbf{E} \times \mathbf{B}) + \sigma_H B \mathbf{E}] \cdot \frac{\nabla N_e}{N_e} \\ &\quad + \sigma_H B \nabla \cdot \mathbf{E} - \sigma_P \mathbf{B} \cdot \frac{\partial \mathbf{B}}{\partial t} \,, \end{aligned} \tag{4.21}$$

using Maxwell's equation $\nabla \times \mathbf{E} = -\frac{\partial \mathbf{B}}{\partial t}$ together with vector identities (*cf. e.g.* Rottman 1961) and assuming σ_P and $\sigma_H \propto N_e$. Furthermore, from Eq. (4.20) one gets

$$\nabla \cdot \mathbf{E} = -\frac{\mathbf{j} \cdot \nabla N_e}{\sigma_P N_e} - \frac{\sigma_H}{\sigma_P} \frac{\mathbf{B}}{B} \cdot \frac{\partial \mathbf{B}}{\partial t} \,. \tag{4.22}$$

Using this in Eq. (4.21) we obtain

$$\mathbf{B} \cdot (\nabla \times \mathbf{j}) = \sigma_C \left[(\mathbf{E} \times \mathbf{B}) \cdot \frac{\nabla N_e}{N_e} - \mathbf{B} \cdot \frac{\partial \mathbf{B}}{\partial t} \right], \tag{4.23}$$

where $\sigma_C = \sigma_P + \frac{\sigma_H^2}{\sigma_P}$, also known as the Cowling conductivity.

Substitution of Eq. (4.23) into (4.19) then finally gives

$$\frac{\partial N_e}{\partial t} = K(\mathbf{E} \times \mathbf{B}) \cdot \nabla N_e + K N_e \left(\frac{1}{2} \frac{\partial B^2}{\partial t} + \frac{\mu \mathbf{j}^2}{\sigma_C} \right), \tag{4.24}$$

with

$$K = \frac{\sigma_C}{N_e(m_e \nu_e + m_i \nu_i)} = \frac{1}{B^2} \frac{\omega_{ce} \omega_{ci}}{\omega_{ce} \omega_{ci} + \nu_e \nu_i} \,. \tag{4.25}$$

In the derivation of the last form of K we have used

$$\sigma_C = \frac{e N_e}{B} \frac{\omega_{ce} \nu_i + \omega_{ci} \nu_e}{\omega_{ce} \omega_{ci} + \nu_e \nu_i} \,,$$

which is obtained from algebraic manipulations after inserting the expressions for σ_P and σ_H (Eq. 4.9) in the equation defining σ_C.

In Eq. (4.24) the term containing $\mathbf{j}^2$ contributes to constant increase in N_e caused by the Ampere force due to the current and the induced magnetic field, *i.e.* a pinch effect (see *e.g.* Singleton 1962). The $\frac{\partial B}{\partial t}$ – term is related to density variation by magnetic pressure. If we neglect these two terms, that is the same as assuming that the fields are electro- and magnetostatic, *i.e.* $\nabla \times \mathbf{E} = -\frac{\partial \mathbf{B}}{\partial t} = 0$ and $\mathbf{B} = \mathbf{B}_o$, which can be done at least under moderately disturbed conditions, Eq. (4.24) appears as

$$\frac{\partial N_e}{\partial t} = -\mathbf{v}_d \cdot \nabla N_e \,, \tag{4.26}$$

showing that the irregularity propagates with the velocity

$$\mathbf{v}_d = K(\mathbf{E} \times \mathbf{B}) = \frac{\omega_{ce} \omega_{ci}}{\omega_{ce} \omega_{ci} + \nu_e \nu_i} \frac{\mathbf{E} \times \mathbf{B}}{B^2} \,. \tag{4.27}$$

It should be noted that **E** here is the total electric field, and that it thus also contains terms due to polarization fields in the irregularity. This component depends on $\frac{\nabla N_e}{N_e}$ and **j** (*cf.* first term in Eq. (4.22)) and will highly modify the motion of the irregularities and can also cause deformations of the shapes (*cf. e.g.* Kato 1963, 1964).

Using the first version of K (Eq. (4.25)), $\mathbf{v}_d$ appears as

$$\mathbf{v}_d = \frac{\mathbf{j}\times\mathbf{B} - \frac{\sigma_H}{\sigma_P} B\left(\sigma_P \mathbf{E} + \sigma_H \frac{\mathbf{B}\times\mathbf{E}}{B}\right)}{N_e(m_e\nu_e + m_i\nu_i)}$$

$$= \mathbf{v}_d^o + \left(\frac{\sigma_H}{\sigma_P} B\right) \frac{\mathbf{j}}{N_e(m_e\nu_e + m_i\nu_i)}. \quad (4.28)$$

The drift velocity of an ionospheric irregularity in a plane perpendicular to the magnetic field will thus consist of two components. The first corresponds to the motion of the ambient ionization, $\mathbf{v}_d^o$. The second is in direction antiparallel to the current and in magnitude $\frac{\sigma_H}{\sigma_P}$ times v_d^o, so that for the regions where $\frac{\sigma_H}{\sigma_P} \gg 1$ the last term will dominate the drift. While the v_d^o - component corresponds to a real body motion, the other velocity, $\frac{\sigma_H}{\sigma_P} v_d^o$, is associated with a wave motion. This will be further discussed in Chapter 8.

5. CURRENT SYSTEMS AND LARGE-SCALE ELECTRIC FIELDS IN THE HIGH LATITUDE IONOSPHERE

5.1. *Introduction*

The presence of ionospheric currents was postulated long before any measurements of electric fields were made. We will therefore first briefly review the present picture of the auroral current systems. In the last, and main part of the chapter, large-scale electric fields will be considered. We will summarize the present knowledge of high latitude *E*-fields, and present the technique for direct probe measurements of electric fields. Finally, the DC fields observed during two specific events, and the relation between electric fields and optical aurora, will be examined in more detail.

5.2. *Ionospheric current systems*

Historically, interest in this topic was raised from the observations of geomagnetic phenomena. Short-time variations in the earth's magnetic field were discovered in 1722 by George Graham (Graham 1724) and later verified in 1740 by Andreas Celcius (Celcius 1741). In 1741 Celcius also noted that there was a close connection between aurora and magnetic disturbance. The first to suggest that atmospheric currents might produce these variations was Carl F. Gauss, in his *Algemeine Theori des Erdmagnetismus* in 1839, even though he could not understand how such currents could possibly exist. A conducting layer in the upper atmosphere was predicted by Balfour Stewart in 1882 (20 years before the experimental radio 'discovery' of the ionosphere), and he ascribed the daily magnetic variations to electric currents flowing in this layer.

Studying high latitude magnetic perturbations, Kristian Birkeland in 1908 proposed a *system* of currents in the upper atmosphere to explain the observed variations in the magnetic field during 'polar elementary storms' (now known as polar magnetic substorms). Combining magnetic data from several stations he inferred a horizontal distribution of currents causing the perturbations. The complete system consisted of horizontal currents in the upper atmosphere supplied by vertical (geomagnetically field aligned) currents from the magnetosphere. He was, however, fully aware that this system was only one of many possible models, and that it did not necessarily represent the actual current flow (Birkeland 1908, pp. 43–44).

In 1935, Chapman launched a competitive current system to explain the magnetic disturbances. This system, which was taken up by Vestine (Vestine & Chapman 1938) and others, grew to dominate the picture of ionospheric currents in the coming three decades. (Schematic illustrations of the Birkeland and Chapman currents systems are shown in Fig. 5.1.) Chapman's current pattern is entirely two-dimensional and is composed of a strong bimodal current, electrojet, along the

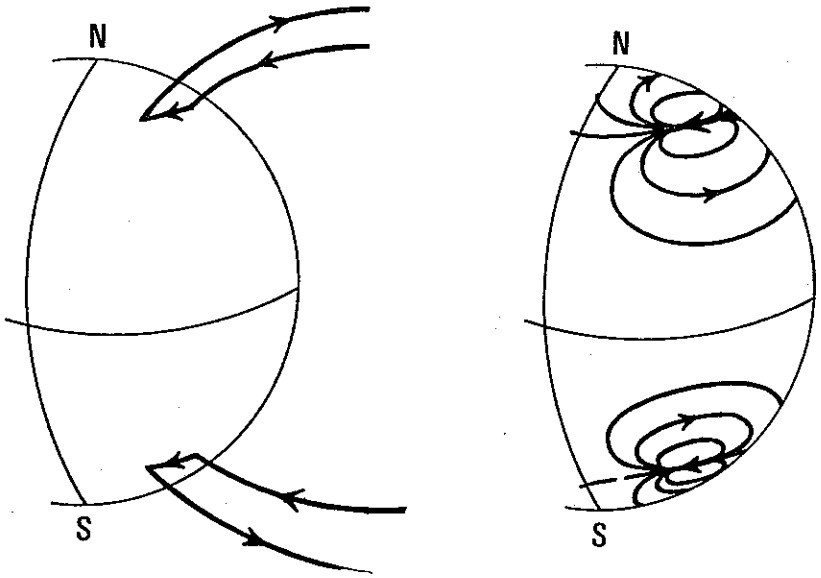

Fig. 5.1. Schematic illustration of the Birkeland (left) and Chapman (right) current systems for a polar magnetic substorm (after Fukushima 1969).

auroral oval, tied together with return currents at higher and lower latitudes. The magnetic effects as observed on the ground at auroral and middle latitudes, are, however, the same for both systems (Fukushima 1969), and for several reasons the Chapman–Vestine view was preferred by most workers in the field rather than the Birkeland system, which was mainly advocated by Alfvén (*e.g.* Alfvén 1939, 1940, 1950).

In recent years, with observations from rockets and satellites, several independent investigations have, however, provided experimental evidence for field-aligned currents (Zmuda *et al.* 1966; Hoffman & Evans 1968; Armstrong & Zmuda 1970; Cloutier *et al.* 1970; Park & Cloutier 1971), and three-dimensional current-systems based on Birkeland's ideas were again brought forward (Boström 1964, 1968; Cunnings & Dessler 1968). (In 1972 it was suggested by the International Geophysical Union that field-aligned currents in the ionosphere and magnetosphere should be called Birkeland currents.) Figure 5.2 shows a current configuration deduced by Park & Cloutier (loc. cit.) from rocket observations.

Besides the change from a two-dimensional to a three-dimensional model, the picture has also changed from a completely static pattern of the kind shown in Fig. 5.3, where the earth is rotating under a fixed current system, to a more dynamic and variable pattern. We will in the following tie together in a descriptive form some of the latest ideas, in an attempt to give an up-to-date picture of the auroral electrojet. (For a definition of the various terms used in connection with the substorm concept, see *e.g.* Davis 1972.)

The direction of the electrojet changes, not only

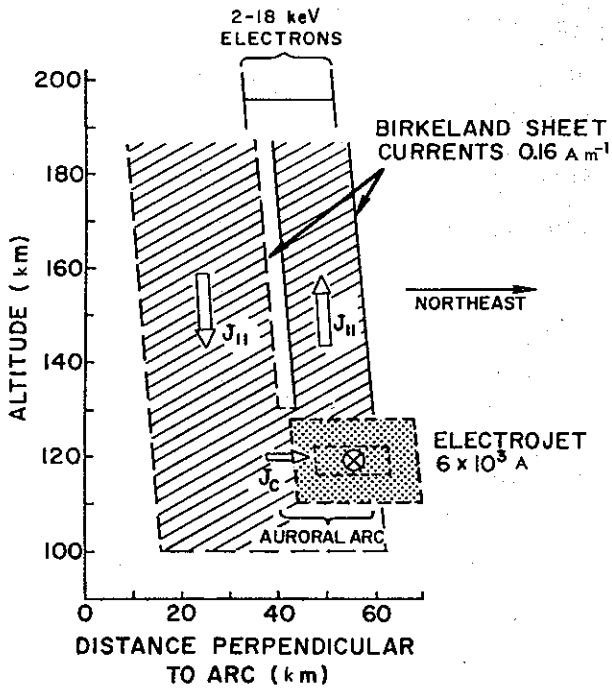

Fig. 5.2. Current system deduced by Park & Cloutier (1971) from rocket measurements of particles and magnetic fields. The complete current configuration consists of an east-west electrojet, two Birkeland sheet currents, $J_{\parallel}$, at the edges of an auroral arc, and a closing current, J_C, between the Birkeland currents.

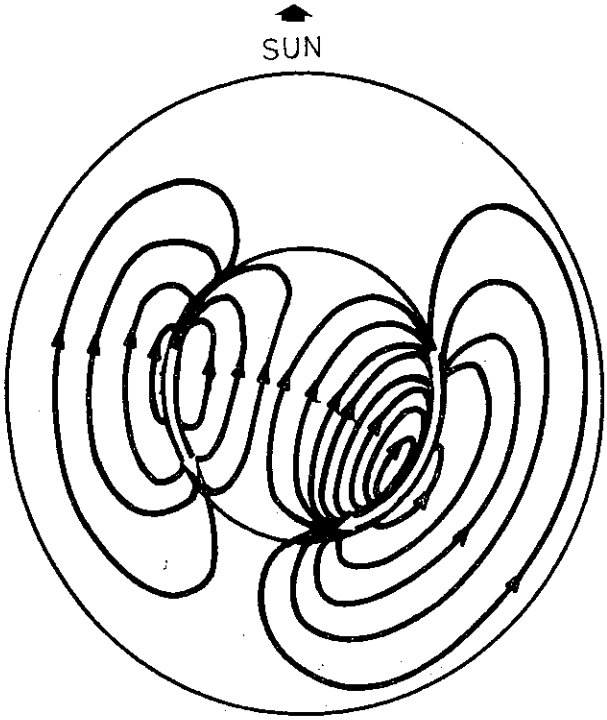

Fig. 5.3. Old model of current system for polar magnetic substorm, view from above the magnetic north pole.

with local time, as in the old picture, but also with the development of the substorm. During the quiet phase there is strong evidence of a bimodal electrojet pattern, with eastward currents in the afternoon end evening sectors, and westward currents in the morning sector, as in the old picture. This configuration will also exist during the growth phase of the storm. The picture in the midnight sector is, however, particularly uncertain, and the mapping of the flow in this discontinuity region, where a reversal of the electrojet takes place, is quite ambiguous and variable. Since Harang (1946) was the first to draw attention to the structure of the currents in this sector, it has been suggested (Heppner 1972*a*) that the region should be called the 'Harang discontinuity'.

At the start of the expansive phase (breakup, $t = 0$ in Akasofu's substorm picture (Akasofu 1968)), the picture apparently changes to a unimodal westward current. Figure 5.4 gives a picture of the configuration during this phase.

The recovery phase will also bring about a recovery of the auroral electrojet. There is a widespread current in the morning sector, and a growth of the eastward current along the auroral zone in the afternoon and evening sectors, with a gradual transition to a quiet-phase picture.

Measurements of drift motions of artificial ion clouds (see Sect. 5.5) in the magnetosphere (Haerendel & Lüst 1970) and polar-cap ionosphere (Westcott *et al.* 1970) have produced strong evidence against the existence of return currents over the polar cap. Further analysis of measurements of electric fields and magnetic perturbations led Heppner *et al.* (1971*a*,*b*) to the conclusion that practically all polar-cap horizontal disturbances in the magnetic field had to be explained in terms of non-ionospheric currents. A mid-latitude ionospheric current to close the auroral electrojet was ruled out for the reasons that both the night-time electron density and electric field were too low to support a current of sufficient intensity. The model proposed for a continuation of the auroral electrojet is shown in Fig. 5.5. Field-aligned currents complete the electrojet circuit, and their general ionospheric pattern of current flow gives an inward current in the morning sector and an outward current in the Harang discontinuity region.

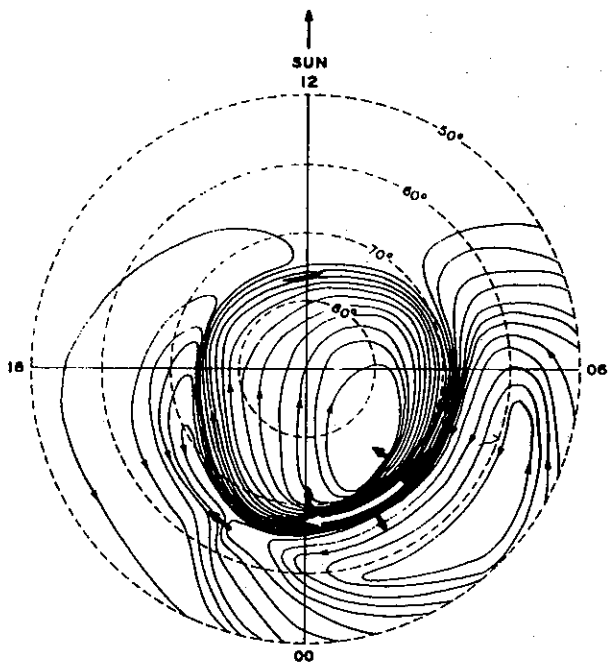

Fig. 5.4. New model of current system during the expansive phase of a substorm, view from above magnetic north pole (after Akasofu 1966).

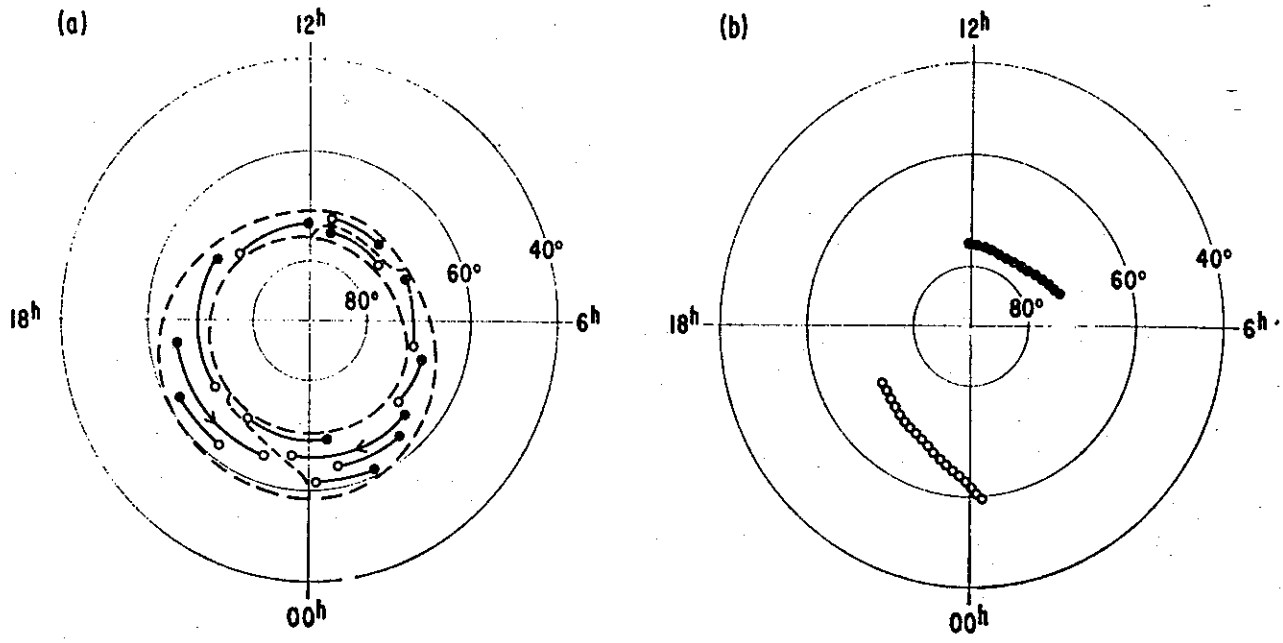

Fig. 5.5. Schematic illustration of electrojet Hall currents terminated in Birkeland currents (part (*a*)). Part (*b*) shows the net distribution of Birkeland currents, resulting in sheet configurations of net field-aligned current. Open and filled circles indicate currents 'out of' and 'into' the ionosphere, respectively (after Heppner *et al.* 1971*a*).

Figures 5.6 and 5.7 will then give a representative picture of the present model of the auroral current system. During the quiet, growth, and the last part of the recovery phase of the substorm, the electrojet is bimodal, and is continued in field-aligned currents, which give an inward net current flow in the morning sector and an outward flow in the Harang discontinuity (Fig. 5.6). The closure of the system in the magnetospheric equatorial plane is consistent with an asymmetric ring current. The ionospheric polar cap and mid-latitude return circuits are weak. In the expansive phase and the first part of the recovery phase, the current system consists of an unimodal westward electrojet (Fig. 5.7). Field-aligned currents, flowing into the ionosphere from the morning sector and out to the magnetosphere in the evening sector, establish a connection between the magnetospheric ring current and the ionospheric system.

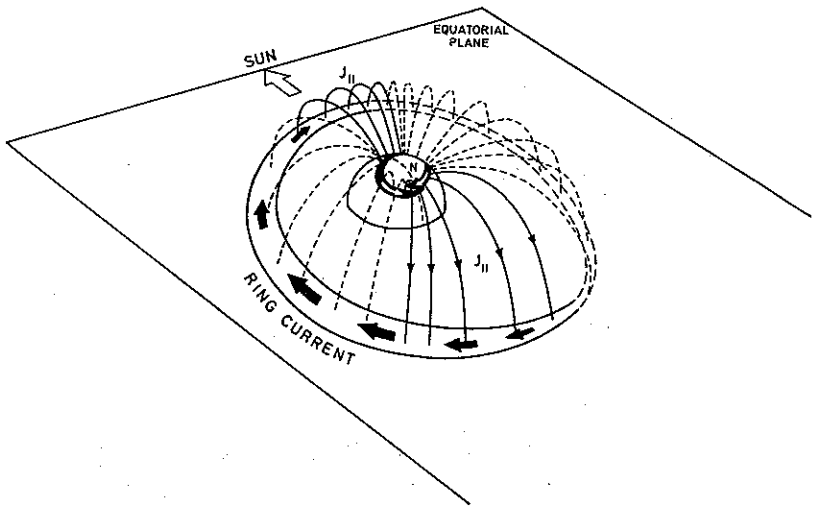

Fig. 5.6. Schematic three dimensional model of a current system for the quiet, growth, and recovery phase of a substorm. The system consists of a bimodal electrojet, linked to Birkeland currents giving a net inward current flow in the morning sector and an outward flow in the midnight sector. The closure of the Birkeland currents is in an asymmetric ring current in the magnetosphere. Fully drawn lines represent regions with major net currents.

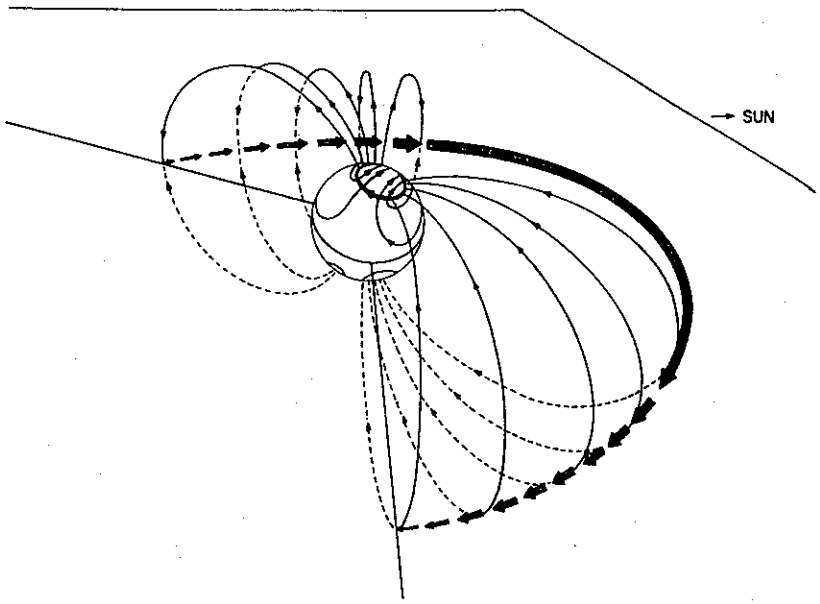

Fig. 5.7. Three dimensional current system for the expansive phase of the substorm, consisting of an unimodal electrojet, Birkeland sheet currents and an asymmetric ring current (after Akasofu & Meng 1969).

5.3. *Sources of DC electric fields*

The driving forces of the auroral electrojet will be electric fields of global structure. The sources of the fields will primarily be found in the magnetosphere, but one must also consider fields of more local character.

Electric fields in the magnetosphere can be produced by several mechanisms. Magnetic field curvature and gradients cause the electrons and ions to move with slightly different velocities, which in turn will bring them into different regions. The charge separation will produce an electric field, and it has been suggested that this should be the primary mechanism for magnetospheric fields (Fejer 1961; Kern 1962). In another theory, introduced by Alfvén (1960) and later taken up and modified by several others (*e.g.* Karlson 1963; Block 1966), the magnetospheric electric field was supposed to be the field induced within a magnetized solar plasma beam.

These mechanisms will certainly have influence on the electric fields in the magnetosphere and ionosphere. However, recent investigations of *e.g.* auroral motions (*e.g.* Davis 1971), dynamics of the plasmasphere (*e.g.* Carpenter 1970), and electric fields (*e.g.* Caufman & Gurnett 1971) have called new attention to convection processes proposed by Axford & Hines (1961) and Dungey (1961) as the principal source of magnetospheric electric fields. Energy and momentum from the solar wind may be transferred to the magnetosphere by a viscous-like interaction at the boundary of the magnetosphere. This energy induction will cause a convection of the magnetospheric plasma, *i.e.* the low-energy plasma experiences a large-scale circulation in the geomagnetic field, as shown in Fig. 5.8a. Another possible

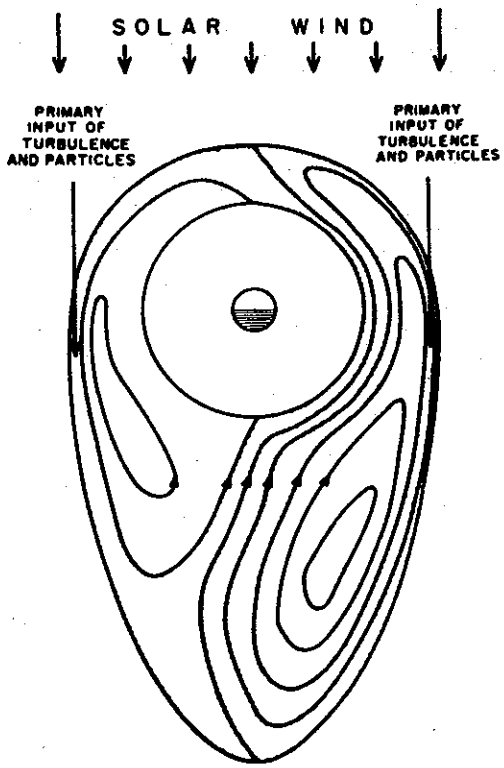

Fig. 5.8.a. Model of magnetospheric convection patterns as originally suggested by Axford & Hines (1961).

energy input is through reconnection of magnetic field lines in the tail section as illustrated in Fig. 5.8b (*cf.* Dungey 1961). However, regardless of the type of interaction which takes place, the result will be a convection of the plasma inside the magnetopause. This motion of the charged particles will induce an electric field (*cf.* Eq. (4.1)) $\mathbf{E} = -\mathbf{v} \times \mathbf{B}$, and a connected electrical potential, φ. If $\partial/\partial t = 0$, i.e. steady motion, we will have $\mathbf{E} = -\nabla\varphi$ and hence the streamlines of the convective motion and the magnetic field lines will be equipotential. However, the behaviour of the magnetosphere during a substorm has clearly demonstrated that the convection is not steady and that $\partial B/\partial t \neq 0$, and instead of the simple relationship between field and potential we will have $\mathbf{E} = -\nabla\varphi - \frac{\partial \mathbf{A}}{\partial t}$, where $\mathbf{A}$ is the magnetic vector potential defined by $\mathbf{B} = \nabla \times \mathbf{A}$. However, Eq. (4.1) is still valid, so that $\mathbf{E}$ will remain perpendicular to $\mathbf{v}$ and $\mathbf{B}$.

Without going any further into the processes of generation, in the following we will pay attention to the behaviour of the electric field.

Due to the high parallel conductivity (*cf.* Sect. 4.2) the electric field will propagate along the magnetic lines of force. Although the large scale fields are little attenuated in this propagation (*cf. e.g.* Farley 1959), the mapping onto the ionosphere cannot, as is frequently done, be assumed as perfect. It has for instance been shown (Mozer 1970) that the direction of the field will not be exactly preserved, due to different attenuation of the different components. Furthermore, finite potential drops will occur along the field lines. If the voltage drop is different along different field lines, this will give horizontal potential differences in the ionosphere not due to magnetospheric fields. Any convection pattern generated outside the ionosphere can also be strongly affected by regions of high conductivity (*e.g.* an auroral arc). The magnetospheric plasma may tend to flow around and thus avoid such regions (Baker & Hammel 1962). An alternative way to regard this is to consider the *E*-field source as a constant current generator (Aggson 1969). A high conductivity region in the ionosphere will load the generator, thus causing a voltage drop.

Differences in propagation conditions and conductivities will thus disturb the image of magnetospheric fields exposed in the ionosphere. On a large scale, however, the distribution of electric fields in the ionosphere and in the equatorial plane of the magnetosphere must be related.

5.4. *Characteristics of large-scale electric fields*

Up to about 1960 the interest in ionospheric electric fields was very low, and no serious attempt was made to accomplish direct field measurements. The main reason for this was that infinite conductivity was generally assumed along the magnetic field lines. The fields could therefore be obtained straightforward from measurements of **B**. This attitude has completely changed, and the

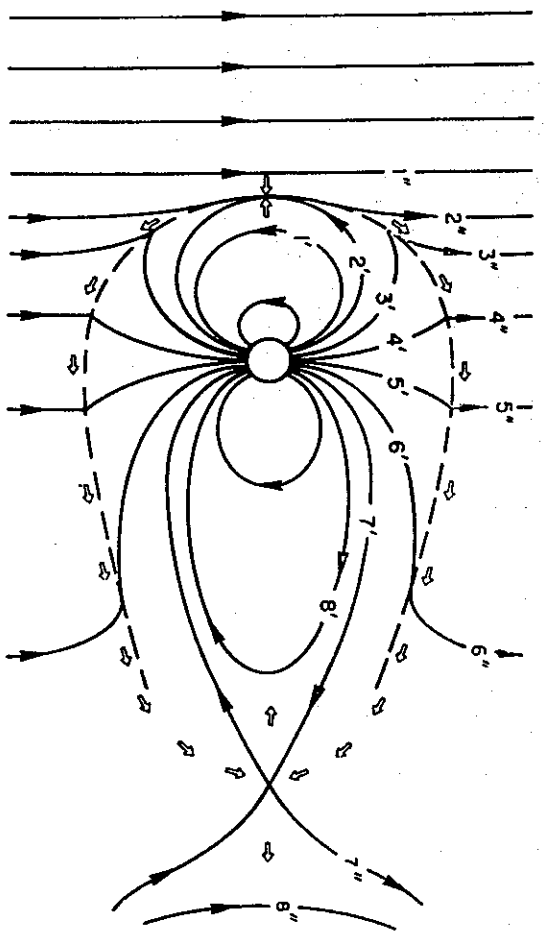

Fig. 5.8.b. Interaction between interplanetary and geomagnetic field and the resulting plasma flow (open arrows) as proposed by Dungey (1961). Numbers indicate motion of individual field lines with the motion progressing toward higher numbers. Reconnection occurs at the contacts 2'-2'' and 7-'7'' (Levy *et al.* 1964).

electric field is now regarded as an important and necessary parameter in the understanding of the physics of the ionosphere. The last decade's direct and indirect determinations of ionospheric *E*-fields have increased our knowledge of the nature of fields considerably. However, when combining the various groups of information, the resulting picture is far from unambiguous. In this section we will review its main aspects.

There is general agreement concerning the magnitude of the fields. Typical values in the auroral oval are 30–50 mV m^{-1}, but variations from less than 10 to 150 mV m^{-1} are not unusual. The field can, however, undergo large variations in magnitude and direction over short distances and times (*cf.* Fig. 5.17). In most cases there seems to be no systematic variation with altitude of fields perpendicular to **B** (Potter 1970; Maynard 1972), but *e.g.* Mozer & Fahleson (1970) have published results contradicting this.

The field has been shown (*e.g.* Wescott *et. al.* 1969; Fahleson *et. al.* 1971) to be predominantly poleward during positive bays and equatorward during negative bays (Figs. 5.9 and 5.13). This confirms that the currents causing the magnetic perturbations at auroral latitudes are mainly Hall currents. It has, however, been clearly demonstrated (*e.g.* Haerendel *et al.* 1969; Wescott *et al.* 1969) that there is no simple relation between the magnitudes of the electric field and the magnetic perturbation. This means that the conductivities, which are as important for the determination of the current as the field itself, are subjected to great variations. As the surface magnetic observatory will only see integrated effects of the regional ionospheric current, it is clear that the possibility of deducing information about the fields from observed magnetic disturbances is very limited.

The electric field in the midnight sector will, in the same way as the current configuration, undergo large variations. The instantaneous form and location of this discontinuity region, where convection patterns, motion of auroral forms, and the direction and magnitude of the fields are rather confused, are frequently changing (Heppner 1972*a*).

The question of what happens to the electric field near and inside an auroral form has also been subject to discrepancies. Aggson (1969) deduced from probe experiments that the field in an arc was greatly reduced, and this seemed to be confirmed by other experiments (Wescott *et al.* 1969; Potter & Cahill 1969). However, Mozer & Fahleson (1970) found cases were the field on average remains constant when crossing the boundary of an arc, but large amplitude fluctuations can be present, both at the boundary and inside the arc. Other measurements have given examples where the field stays rather constant in the transition of the aurora (Ungstrup, priv. com.). Thus the results are controversial, and the situation seems to change from one case to the other. It should, however, be noted that none of these authors made in situ measurements of the optical emissions, but used particle detectors and television cameras (Mozer & Fahleson), triangulation from several ground camera sites (Wescott *et al.*), particle detectors (Potter & Cahill), or particle detectors, ground photometers and cameras (Aggson, Ungstrup) to identify the location of the optical forms. (We will return to this subject later in this chapter.)

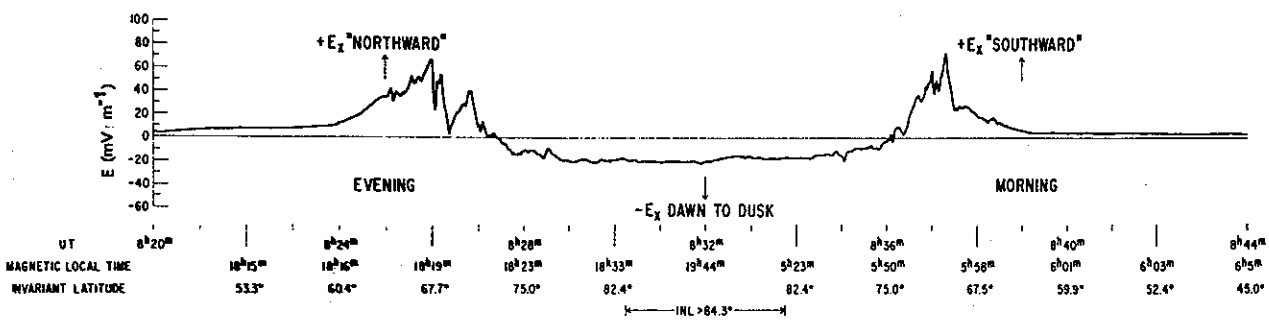

Fig. 5.9. A northern polar pass of OGO-6, showing the electric field at auroral latitudes and over the polar cap (after Heppner 1972*b*).

The existence of electric fields parallel to **B** in the auroral zone is another controversial question. Important as such fields would be for particle acceleration and precipitation, they have been suggested by many theorists (*cf. e.g.* Alfvén & Fälthammar 1963; Persson 1967). Probe measurements by Mozer & Bruston (1967, later re-examined by Mozer & Fahleson 1970) seemed to verify the existence of a parallel field. However, their value of ≈ 20 mV m^{-1} seems to be too high, compared to theoretical values. Mozer and Fahleson also found an increase with altitude of the perpendicular field, which maintains $\nabla \times \mathbf{E} = 0$ required in the steady-state condition assumed in their derivation.

On the other hand, several other workers (*e.g.* Mende 1968; Wescott *et al.* 1969; Potter 1970) using different observation techniques, deduced that no parallel fields of any importance (< 60 μV m^{-1}) existed. Some of the assumptions made in the pro-parallel-field papers were also thrown into doubt.

Recent probe measurements from the satellite Injun-5 have, however, shown that weak parallel fields may be present (Cauffman & Gurnett 1971). Hultqvist (1971) has also obtained new experimental evidence for the existence of parallel fields in observations of field-aligned anisotropy in ion pitch-angle distribution in the auroral zone and over the polar cap.

Thus the dispute on parallel fields continues. However, the bulk of the evidence seems to support the statement that parallel fields do exist, but that they are generally markedly less (order of magnitude) than the perpendicular component. In addition, electrostatic waves and short duration electric fields of much greater amplitude can be found.

Measurements of electric fields in the polar cap have led to a revised conception of the current configuration in these regions (*cf.* Sect. 5.2). From release experiments (Wescott *et al.* 1970) and satellite data from OGO-6 (Heppner 1972*b*) it was found that in the polar cap the convection velocity was away from the sun and the resulting

Table 5.1. Characteristics of high latitude electric fields

PROPERTY	CONCLUSION	KEY REFERENCE
Magnitude	30–50 mV m^{-1} (typical) 10–150 mV m^{-1} (freq. obs.)	Wescott *et al.* 1970
Amplitude variation	Variable over short dist. and time	Haerendel *et al.* 1969
	No systematic variation with altitude	Potter 1970, pro; Mozer & Fahleson 1970, contra.
Auroral electrojets	Hall currents	Wescott *et al.* 1969.
Relation **E**, Δ**B**	Complex. Conductivities important	Haerendel *et al.* 1969.
E in aurora	Reduced in magnitude inside forms	Aggson 1969, pro; Mozer & Fahleson 1970, contra.
Parallel fields	Exist, but less than perp. fields	Mozer & Fahleson 1970, pro; Potter 1970, contra.
Polar cap fields	Directed dawn-dusk	Heppner 1972.
	Polar cap currents: field aligned	Heppner *et al.* 1971.

electric field pointing toward the evening sector, thus giving rise to a field reversal at the poleward boundary of the auroral zone (Fig. 5.9). The observed ground magnetic variations excluded Hall or Pedersen currents as a possible explanation, and a field-aligned current system completing the electrojet circuit is proposed (Sect. 5.2).

The polar-cap field was found to be quite uniform in space and time (Heppner loc. cit.), but small scale changes are very evident (Maynard & Heppner 1970). The magnitude of the polar-cap field is typically 20–40 mV m^{-1}.

Conclusions from the measurements of high-latitude electric fields in the ionosphere are summarized in Table 5.1. Improved experimental techniques have provided new information about the magnitude and structure of the fields and their associated currents. This in turn has given a better understanding of the origin of the electric fields. However, important questions, such as the existence of fields parallel to **B** and the configuration in the noon and midnight sectors, are still unanswered.

5.5. *Experimental techniques for in situ measurements of electric fields*

In situ measurements of electric fields are cluttered by several difficulties and have historically lagged behind the theories for fields and current systems in the ionosphere. Indirect determinations, mainly based on measurements of drift velocities, magnetic perturbations, and particle parameters, suffer from a lack of exact information about other properties involved in the field calculations.

During the last few years two different techniques, the release technique and the double floating probe technique, have, however, proved capable of giving dependable results.

The principle of the *release technique* is that an artificial cloud, usually barium, is injected into the ionosphere. This cloud will be partly ionized by photon-ionization. While the neutral cloud drifts along with the wind system, the ionized cloud will be under the additional influence of electric and magnetic fields (*cf.* Sect. 4.3). By determining the velocity of the Ba^+-cloud relative to the neutral constituents it is possible to deduce information about the direction and magnitude of the electric field.

The technique has proved to be very useful for studying long-time variations of DC fields in the ionosphere and magnetosphere. However, the requirement of twilight conditions (sunlight for photon-ionization, but dark enough for optical tracking), severely restricts local time coverage. The presence of the ion cloud may also disturb the medium and give rise to plasma instabilities. (For details and a theoretical background for such measurements, see, for example, Haerendel *et al.* 1967.)

The electric field measurements performed in this investigation were based on *the double floating probe technique*, and in the following we will concentrate on the principles behind this kind of observation.

5.5.1. *Probe design.* Intuitively one has the feeling that the most straightforward way to accomplish a determination of electric field strengths is to establish two reference points in the plasma and measure the voltage between these. As the potential of the spacecraft is poorly defined, a monopole using the vehicle itself as reference point is generally unsuitable. A monopole will also be unduly sensitive to technological interference of various kinds.

The electric field can in principle be calculated from the voltage measured between two (or more) electrodes in contact with the plasma, if the geometry of the electrodes is known. There are, however, several practical difficulties involved in these measurements. A conducting body inserted into a plasma will in most cases attain a potential different from that of the surrounding plasma. This causes an attraction of charged particles with one sign, while particles with opposite charge will be repelled. Thus, a layer will be established near the probe where charge neutrality does not exist. The thickness of this plasma sheath will depend on the shape, surface, and dimension of the probe, the Debye length, and a function monotonically increasing with the ratio probe potential to plasma thermal energy (Storey 1963). The voltage drop in the sheath is very difficult to determine both theoretically and in plasma laboratories. It will

also most probably be different for differently shaped and oriented probes. A fundamental rule for probe measurements is therefore that the sensors should be equally shaped, that they should be made from the same material and that their electrical connections should be identical. Another requirement is that the electrical mid-points of the probes should be far away from each other (several metres). This provides a long baseline for the measurements, giving a potential difference which is large compared to voltages from disturbing effects, and removes the active parts of the antennas away from interference sources and regions screened off by the spacecraft.

The types of probes used for electric field measurements can be designated either as 'long cylindrical booms' or 'spherical antennas'. The first group can be long metal rods, either plain metal, insulated, or partly insulated, while the second type of probes consists of small metal spheres supported by insulating rods. The probes used in our measurements were of the first kind, and the following considerations will therefore be limited to the long cylindrical boom technique.

With the *STEM* technique (*STEM*: Storable Tubular Extendible Member) originally developed for the Alouette satellites (*cf. e.g.* Mar & Garrett 1969), it is possible to attain a large separation between the electrical centres of an antenna system consisting of two cylindrical booms. As the antenna elements in most cases are erected from the vehicle itself, the difficulty with a long connection line between the electronics and antenna is avoided. The disadvantages with this probe system arise mainly from the extension of the contact area between the electrode and the plasma. One may thus have variations over the dimension of the probes which make the geometry of the system somewhat uncertain. The steady electric field will also have influence on the AC properties of the antenna, creating a displacement between the electrical and geometrical centres of the antenna (Storey 1963). For a symmetrical dipole system of two similar elements extended in opposite directions, the displacement of the electrical centres should in theory be the same so that the total effective length will remain constant. But, even so, the probe system may be unbalanced with respect to the spacecraft body, making the measurements more exposed to technological interference. Another circumstance which can affect the signal from the booms is that a part of the antenna will be in a region perturbed by the spacecraft body (*cf.* Appendix I).

Both these effects can be eliminated by coating the antenna elements with insulating material. This will, however, introduce the defect that the antenna impedance will be high at extremely low frequencies and also make the probes inapplicable for DC measurements. Where DC and low frequency response is wanted, one has therefore to adopt a compromise solution where part of the antenna element is left uninsulated.

5.5.2. *Probe potential and induced potential difference.* The potential of the probe with respect to the surrounding plasma will govern the currents in the plasmasheath. These currents, J_e: electron current, J_i: ion current and J_{ph}: current caused by photon-emission of electrons from the electrode, must under stationary conditions satisfy the current balance equation

$$J_e + J_i + J_{ph} = J\,. \qquad (5.1.a)$$

J will then be the current flowing away from the probe (to the measuring apparatus). Other charging currents such as secondary emissions have been omitted.

When no current is drawn from the probe it will attain its 'floating potential', φ_o, and the current balance will be

$$J_e(\varphi_o) = J_i(\varphi_o) + J_{ph}(\varphi_o)\,. \qquad (5.1.b)$$

If a Maxwellian velocity distribution is assumed, the electron and ion currents to a surface element dS of a cylindrical probe will be for retarding potentials (*cf.* Mott–Smith & Langmuir 1926)

$$dJ_k = j_{ko} \exp\left[\frac{-e\varphi}{\kappa T_k}\right] dS\,, \qquad (5.2.a)$$

while the expression for accelerating voltages appears as

$$dJ_k = j_{ko}\left\{\frac{b}{a}\left[1 - \operatorname{erf}\left(\frac{a^2 e\varphi}{(b^2-a^2)\kappa T_k}\right)^{1/2}\right] + \operatorname{erf}\left(\frac{b^2 e\varphi}{(b^2-a^2)\kappa T_k}\right)\right\} dS\,. \qquad (5.2.b)$$

The function erf(x), the error function, is defined by

$$\mathrm{erf}\,(x) = \frac{2}{\sqrt{\pi}} \int_x^\infty \exp\,(-y^2)\,dy\,.$$

b and a are the sheath and probe radii, respectively, and j_{ko} denotes the surface current density at $\varphi = 0$. This is the same as the random current density in the gas, and can thus be expressed as a function of particle density and mean thermal velocity (*cf.* Sect. 3.5.3),

$$j_{ko} = \varepsilon_k \tfrac{1}{4} e N_k \langle v_k \rangle = \varepsilon_k \tfrac{1}{4}\, e N_k \left(\frac{8\kappa T_k}{\pi m_k}\right)^{1/2}. \quad (5.3)$$

$\varepsilon_k = +1$ for ions (regarded positively charged) and -1 for electrons.

As $j_{eo} \gg j_{io}$ it is necessary to have $\varphi < 0$ to establish the current balance, except for very high and very low altitude where j_{ph} may dominate over j_e (Fahleson 1967). In the following only negative probe potentials will therefore be considered. Under the conditions existing in the ionosphere the ion current density will not be much changed from j_{io} (Storey 1963) so that the currents can be expressed as

$$\begin{aligned} dJ_e &= j_{eo} \exp\left[\frac{-e\varphi}{\kappa T_e}\right] dS\,, \\ dJ_i &= j_{io} dS\,, \\ dJ_{ph} &= \gamma j_{pho}\, dS\,. \end{aligned} \quad (5.4)$$

The photon current density will be given by an expression similar to Eq. (5.3), and γ is a geometrical factor (< 1) which is mainly determined by the position of the sun with respect to the probe. The integration for J_{ph} goes over the illuminated probe surface.

The probe potential can now be found by combining Eqs. (5.1.b) and (5.4) which gives

$$\varphi_o \approx -\frac{\kappa T_e}{e} \ln \frac{j_{eo}}{j_{io} + j_{pho}}\,. \quad (5.5)$$

Estimating the value of φ_o in a night-time rocket where $j_{pho} = 0$ for the simple case $T_e = T_i$, $N_i = N_e$ and $m_i = 30$ u one gets the rough value $\varphi_o \approx -5.4 \cdot \frac{\kappa T_e}{e}$. In general one can expect a floating potential of the order $\frac{\kappa T}{e}$. However, φ_o will vary with the plasma parameters, a fact which must be taken into account in connection with measurements from rockets and satellites traversing regions with different properties.

If a potential gradient over the probe dimension exists in the plasma, or if the probe is moving in a magnetic field, the current balance will not necessarily be fulfilled for a small surface element. However, in equilibrium the total current to the probe must also in this case be zero, and

$$\int j_e(r, \varphi_o)\, dS = \int j_i(r, \varphi_o)\, dS + \gamma \int j_{ph}(r, \varphi_o)\, dS\,. \quad (5.6)$$

The probe system considered in the following will consist of two cylindrical booms, A and B, symmetrically orientated with respect to an origin. The boom radius is a, and the active surface extends from d_1 to d_2. The electric field in the plasma is $\mathbf{E}$ and the probes are moving with a velocity $\mathbf{v}$. If the potential of the booms with respect to the plasma potential at the origin is $\varphi_{A,B}$, the expression for the electron current through a surface element at distance r will for probe A be

$$dJ_e(r)_A = j_{eoA} \times \exp\left[-\frac{e}{\kappa T_{eA}} (\varphi_A + (\mathbf{E} + \mathbf{v} \times \mathbf{B}) \cdot \mathbf{r})\right] dS\,, \quad (5.7)$$

and similar for probe B (*cf. e.g.* Aggson *et al.* 1965).

Substituting this on the left side of Eq. (5.6) gives

$$2\pi a j_{eoA} \int_{d_1}^{d_2} \exp\left[-\frac{e}{\kappa T_{eA}} (\varphi_A + (\mathbf{E} + \mathbf{v} \times \mathbf{B}) \cdot \mathbf{r})\right] dr = \int_{d_1}^{d_2} j_{iA} dS + \gamma \int_{d_1}^{d_2} j_{phA} dS\,, \quad (5.8)$$

and by integration

$$2\pi a j_{eoA} \exp\left[-\frac{e\varphi_A}{\kappa T_{eA}}\right] \left(-\frac{\kappa T_{eA}}{e(\mathbf{E} + \mathbf{v} \times \mathbf{B}) \cdot \hat{\mathbf{r}}}\right)$$

$$\times\left\{\exp\left[\frac{-e}{\kappa T_{eA}}(\mathbf{E}+\mathbf{v}\times\mathbf{B})\cdot\mathbf{d}_2\right]\right.$$
$$\left.-\exp\left[\frac{-e}{\kappa T_{eA}}(\mathbf{E}+\mathbf{v}\times\mathbf{B})\cdot\mathbf{d}_1\right]\right\}=J_{iA}+J_{phA}\,. \tag{5.9}$$

Rearranging this gives the following expression for the probe potential

$$\varphi_A=-\frac{\kappa T_{eA}}{e}\ln\left\{\frac{\kappa T_{eA}}{e}\frac{2\pi a j_{eoA}\left\{\exp\left[\frac{-e}{\kappa T_{eA}}(\mathbf{E}+\mathbf{v}\times\mathbf{B})\cdot\mathbf{d}_1\right]-\exp\left[\frac{-e}{\kappa T_{eA}}(\mathbf{E}+\mathbf{v}\times\mathbf{B})\cdot\mathbf{d}_2\right]\right\}}{(\mathbf{E}+\mathbf{v}\times\mathbf{B})\,(J_{iA}+J_{phA})}\right\}. \tag{5.10}$$

In a similar way the potential with respect to the plasma potential at the origin can be calculated for the boom B extending from $-d_1$ to $-d_2$.

If exact symmetrical conditions are supposed for the two probes, *i.e.* $T_{eA}=T_{eB}=T_e$, $j_{eoA}=j_{eoB}$, $J_{iA}=J_{iB}$ and $J_{phA}=J_{phB}$, the following expression for the potential difference between the probes appears

$$\varphi_A-\varphi_B=-\frac{\kappa T_e}{e}\ln\left\{\frac{\exp\left[\frac{-e}{\kappa T_e}(\mathbf{E}+\mathbf{v}\times\mathbf{B})\cdot\mathbf{d}_1\right]-\exp\left[\frac{-e}{\kappa T_e}(\mathbf{E}+\mathbf{v}\times\mathbf{B})\cdot\mathbf{d}_2\right]}{\exp\left[\frac{e}{\kappa T_e}(\mathbf{E}+\mathbf{v}\times\mathbf{B})\cdot\mathbf{d}_1\right]-\exp\left[\frac{e}{\kappa T_e}(\mathbf{E}+\mathbf{v}\times\mathbf{B})\cdot\mathbf{d}_2\right]}\right\}. \tag{5.11}$$

By series expansions and algebraic manipulations this can be further reduced to

$$\varphi_A-\varphi_B=(\mathbf{E}+\mathbf{v}\times\mathbf{B})\cdot(\mathbf{d}_1+\mathbf{d}_2)$$
$$=(\mathbf{E}+\mathbf{v}\times\mathbf{B})\cdot\mathbf{d}\,. \tag{5.12}$$

where $\mathbf{d}$ is the vectorial separation between the electrical midpoints of the probes.

It should be pointed out that these calculations should only be regarded as guiding. Nevertheless, this rough analytical treatment is accurate enough to give an understanding of the probe technique, its principles and pitfalls, and it gives a basis for considering the sources of error attached to this kind of measurements.

First of all it should be stressed that the expression for potential difference in Eq. (5.12) appeared under the assumption of exact symmetry in boom orientation and construction. Furthermore, it can be seen that the probe system does not, in general, measure the electric field of an AC wave. It detects only a combination of the field (*i.e.* the gradients of electric potentials) and of the gradients of the various plasma properties which fluctuate under the influence of the wave and thus give rise to variations in the contact potential of the probe. To distinguish between these two contributions is in most cases difficult, as it is necessary to know the complete structure of the wave, and the way the plasma and the probes react to it.

5.5.3. *Error analysis.* Since the theory for probe measurements of electric fields closely follows the theory for Langmuir probes, most of the pitfalls present in such measurements (*cf. e.g.* Willmore 1970) will also appear in this context. However, as the aims of the experiments are different, the importance of the various errors will be different.

In general, one can say that, since the derivation of the expression for the potential difference between the probes (Eq. (5.12)) depended on the assumption that the probes and their environments could be regarded as exactly alike, the measurements are very sensitive to any effects which will cause asymmetries in the probe configuration. Besides, the presence of the spacecraft and probes will disturb the plasma, and one must consider to what extent this will influence the measurements. Of potential importance for the results will be

i) The $\mathbf{v}\times\mathbf{B}$ term.
ii) Disturbances due to finite voltmeter current.
iii) Effects from spacecraft wake.
iv) Work function errors.
v) Sheath overlap.
vi) Spacecraft potential and interference.
vii) Asymmetrical photon-emission, shadowing.
viii) Thermal and aerodynamical bending.

ix) Contact potentials; errors due to variations in ambient plasma; temperature gradients and particle fluxes.

These various effects and their contributions to the measured voltage will be discussed in Appendix I. It turns out that with careful construction of the probes and with a reasonable dimension of the baseline, it is possible to almost eliminate most of the errors, and to keep the most serious ones down on an acceptable level, $< 10\%$ of the total field. However, for vectorial measurements of the field, the $\mathbf{v} \times \mathbf{B}$ term will place requirements on the determination of the rocket attitude which may be difficult to fulfill.

As a concluding remark it can be said that the probe theory in itself leads to equations and expressions with limited region of validity and great uncertainties. In spite of this it is possible, with the double floating probe technique, to eliminate most of the uncertainties as long as a symmetrical probe configuration can be maintained, and the method has proved to give dependable results (*cf. e.g.* Maynard 1972, and references given there).

5.5.4. *Experimental set-up for rocket-borne electric field measurements.* This section will give a description of the instrumentation used for the DC and AC electric field measurements performed in the present study. A modified Mini-*STEM* anten-

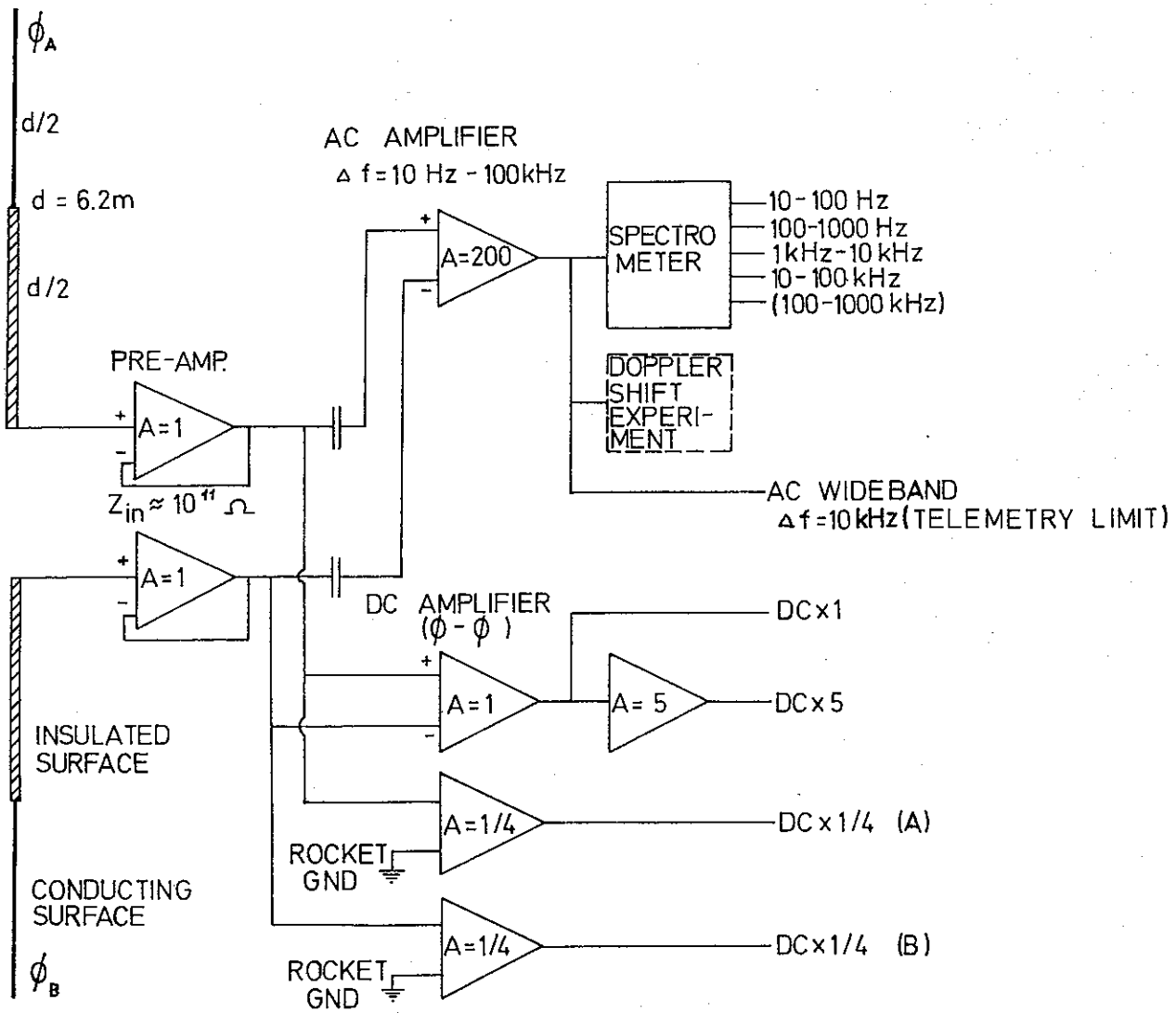

Fig. 5.10. Block diagram of the electronics of the electric field experiment flown in the rockets F23, F24, NASA 14.383 and NASA 18.57. (In the two last rockets the 'Doppler shift' and 'Wideband Channel' were not included.)

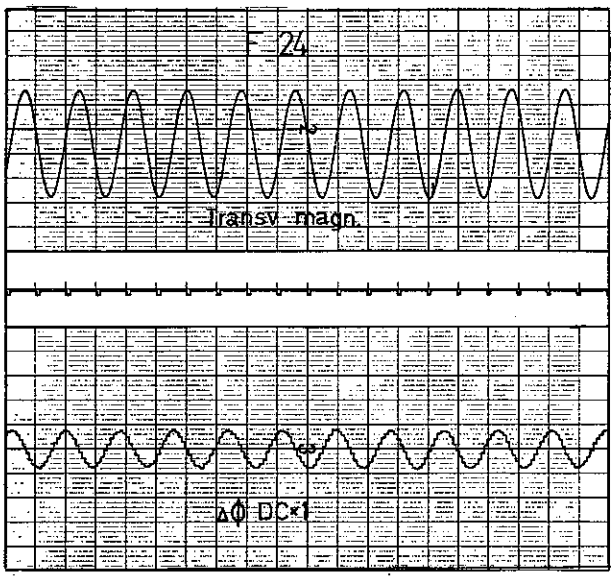

Fig. 5.11. Example of signal from the DC *E*-field experiment. The sinusoidal form of the record appears from the rotation of the probes, which results in a shift in polarization. The upper curve shows the signal from the rocket's transverse magnetometer.

na has been utilized. In this version the deployment of both antenna elements is controlled by one and the same motor, which assures an even extension for the two booms. The elements, made from beryllium-copper, have noble metal plating to obtain an even work function. The inner half of each element has a special coating, providing DC insulation between the conducting element and the plasma. The boom diameter is 0.007 m and the length 6.2 m, giving a $d_{DC} = 9.1$ m.

The electronics are shown in block diagram form in Fig. 5.10. Precision voltage followers with very high input impedance monitor the antenna voltages. The output of these followers are, in the DC part, subtracted through a precision unity gain differential amplifier giving the desired signal, $\Delta\varphi = \varphi_A - \varphi_B$. By an additional amplifier $5\Delta\varphi$ is also monitored. The AC response of the DC electronics goes up to 1 kHz, but in most cases this will be limited by the telemetry capacity.

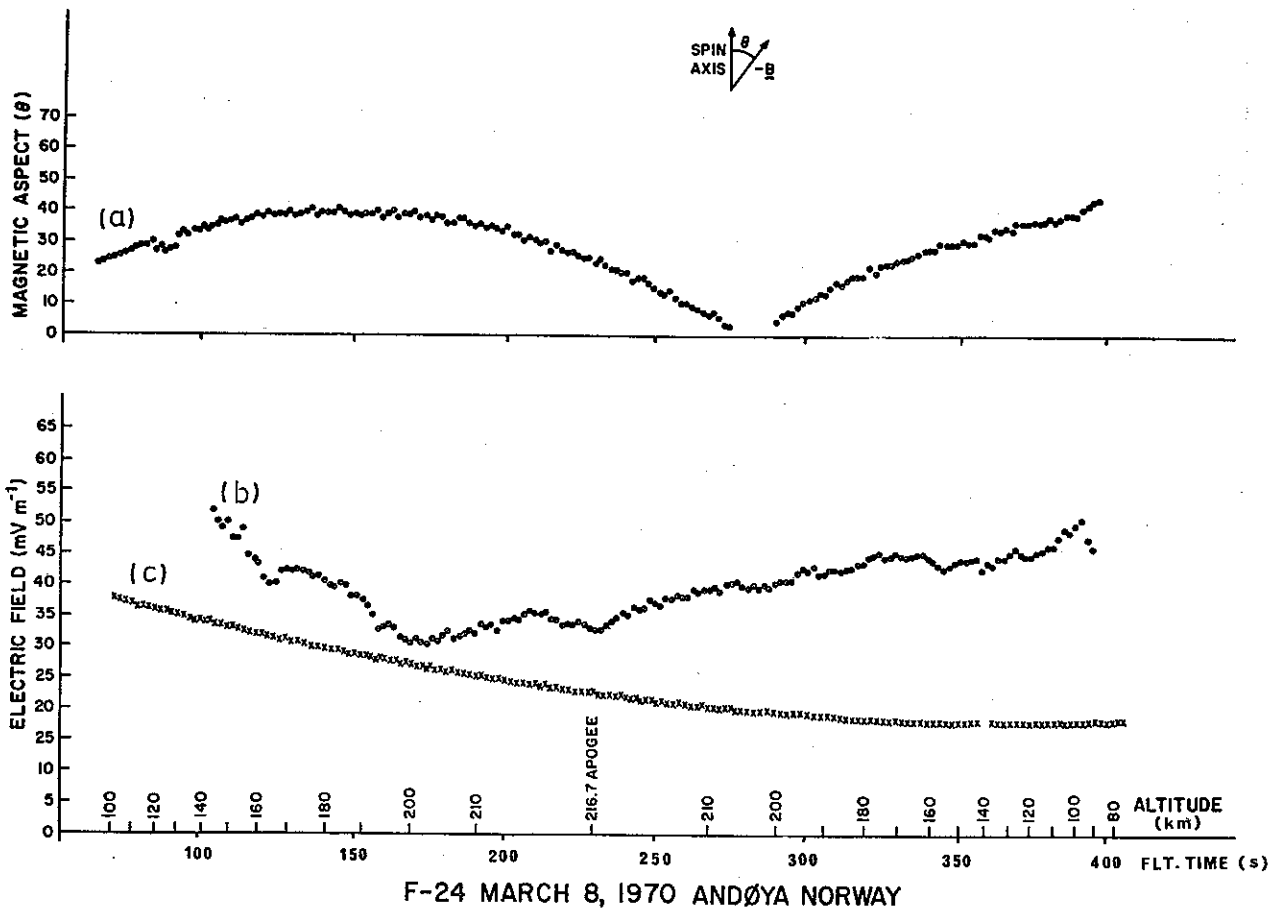

Fig. 5.12. The angle between the rocket spin axis and the negative *B* is shown in curve (*a*). Curve (*b*) shows the total measured field $\mathbf{E}+\mathbf{v}\times\mathbf{B}$, while the calculated $|\mathbf{v}\times\mathbf{B}|$ component is plotted in curve(*c*). Data from F24.

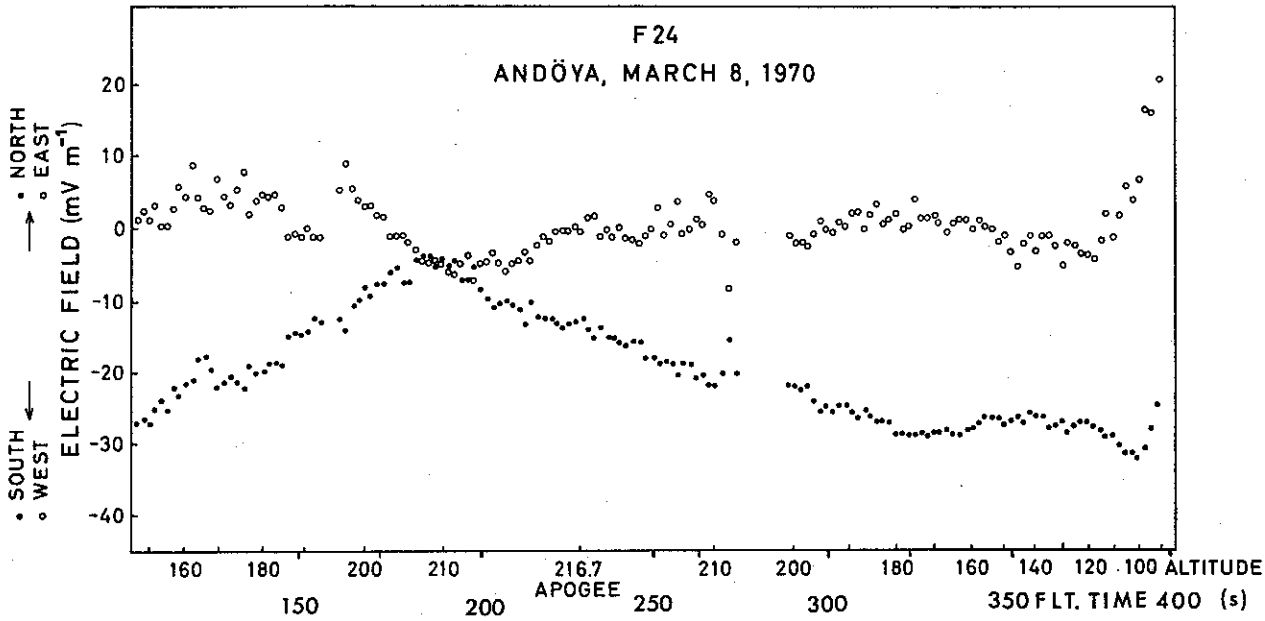

Fig. 5.13. North-south (●) and east-west (○) components of the DC electric field measured during the F24 event. The drop-out in data points between 275 and 290 s is from the part of the flight when the rocket axis was about parallel to the earth's magnetic field, so that determination of the attitude of the probes in a plane perpendicular to **B** was very uncertain. The apparent change in the field-components in the last data points is due to bending of the antenna elements caused by atmospheric drag (*cf.* Appendix I).

In addition, the voltage differences between each of the probes and spacecraft ground are also monitored, giving a check on the probe symmetry and variations in contact potentials. The input resistance of the system is greater than 10^{11} ohms and input current leakage less than 10^{-11} A. The capacitance is approximately 50 pF. Comparing this with the findings in Appendix I, one will see that no disturbances from the voltmeter current should be expected. A broadband amplifier with frequency response 10 Hz to 100 kHz is AC coupled to the voltage followers. The AC differential voltages can be monitored directly in broadband analogue form. The AC signal is also recorded by a spectrum analyzer. The number of channels and frequencies covered are subjected to alterations, but in the present version the spectrometer consists of five channels, each covering one decade in the frequency range 10 Hz to 1 MHz. The integrators have a nonlinear response, and the dynamic range is somewhat less than 40 dB.

The sensitivity is of the order of 1 mV m^{-1} for the DC experiment, and 10 μV m^{-1} peak to peak for the spectrometer and broadband experiment. The part in the block diagram called 'VLF Doppler' is a wave propagation experiment which will be further described in Chapter 6.

In the data reduction the magnitude and phase of the total measured DC fields ($\mathbf{E}+\mathbf{v}\times\mathbf{B}$) in the rocket spin plane were determined from the sinusoidally varying voltage from the differential amplifier (see Fig. 5.11) and the lateral aspect magnetometer. To get $\mathbf{v}\times\mathbf{B}$ it is necessary to know the trajectory, which was calculated from slant range Doppler data. The value of **B** was taken from the Cain & Cain (1968) model. Vector subtraction of $\mathbf{v}\times\mathbf{B}$ and location of the field in a topographic coordinate system require detailed information on the attitude of the vehicle, which is obtained from the magnetic aspect data.

The errors in the vectorial computations can be large, especially concerning a component that is small compared to the major component (*i.e.* the east-west field in our case). A five-degree attitude error can result in an error of 9% of the spin plane $\mathbf{v}\times\mathbf{B}$. Similarly, the error in the measurement of the phase of ($\mathbf{E}+\mathbf{v}\times\mathbf{B}$) is ± 1 degree, adding another 2% error. Trajectory errors are estimated as $\pm 2°$ in phase $\mathbf{v}\times\mathbf{B}$ calculation or another 4% on the east-west component (making

a total of 15%). The corresponding error from all sources on the main component is +1%. The $\mathbf{v} \times \mathbf{B}$ magnitude early in these flights is about 30 mV m^{-1}. Thus, the confidence level in the results after calculation for the topographic components is ± 5 mV m^{-1}. An additional overall error of ± 1 to to 2 mV m^{-1} in total magnitude may be present from considerations of the physical technique (*cf.* Appendix I).

5.6. *Event studies of DC electric fields*

While Sect. 5.4 presented the main characteristics from a great number of electric field measurements, we will in this section examine in more detail the observations from two specific events, with special emphasis on the relation between auroral particles and variations in the field amplitude. The data originate from the two rocket flights (F23 and F24) described in Chapter 2.

5.6.1. *Electric fields and optical emissions in the F24 event.* Figure 5.12 shows the total measured field in the spin plane ($\mathbf{E}+\mathbf{v} \times \mathbf{B}$) throughout the flight. In Fig. 5.13 the calculated east-west and north-south components of the field are plotted. The measurements seem to reflect the stable PCA launch conditions, with almost total lack of short period variations. The field amplitude varied from a few mV m^{-1} to near 40 mV m^{-1}, with the lowest values recorded from 150 to 250 s (flight time). No systematic altitude dependence was observed. The field was, within the accuracy of the attitude determination, southwards, consistent with the established picture of a westward Hall current during a negative bay.

The optical instrumentation in the payload consisted of three photometers, mounted with their optical axis parallel to the rocket's longitudinal axis. The emissions N_2^+ 1N (4278 Å), OI(5577 Å) and N_2 1P (6705 Å) were measured. The measured photon emission rate above the rocket at 4278 Å during the flight is shown in Fig. 5.14. The observed asymmetry of the curve about apogee cannot be explained by temporal variations of

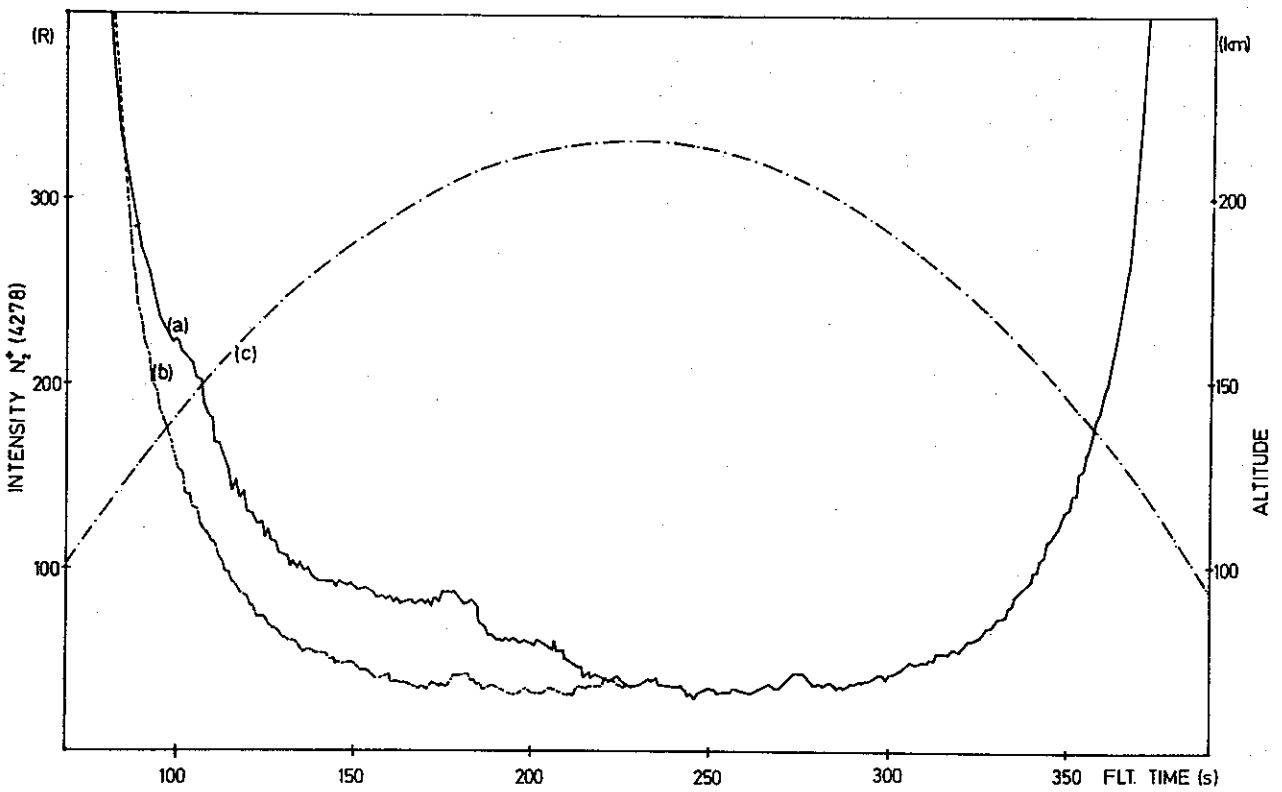

Fig. 5.14. Curve (*a*) shows photometric recordings of the intensity of N_2^+ (4278 Å) as measured above the rocket *vs.* flight time. In curve (*b*) the intensity measured during the descent part of the flight is mirrored about apogee (228 s) to show the asymmetry in the recordings. The rocket altitude *vs.* time is plotted in curve (*c*). Data from F24.

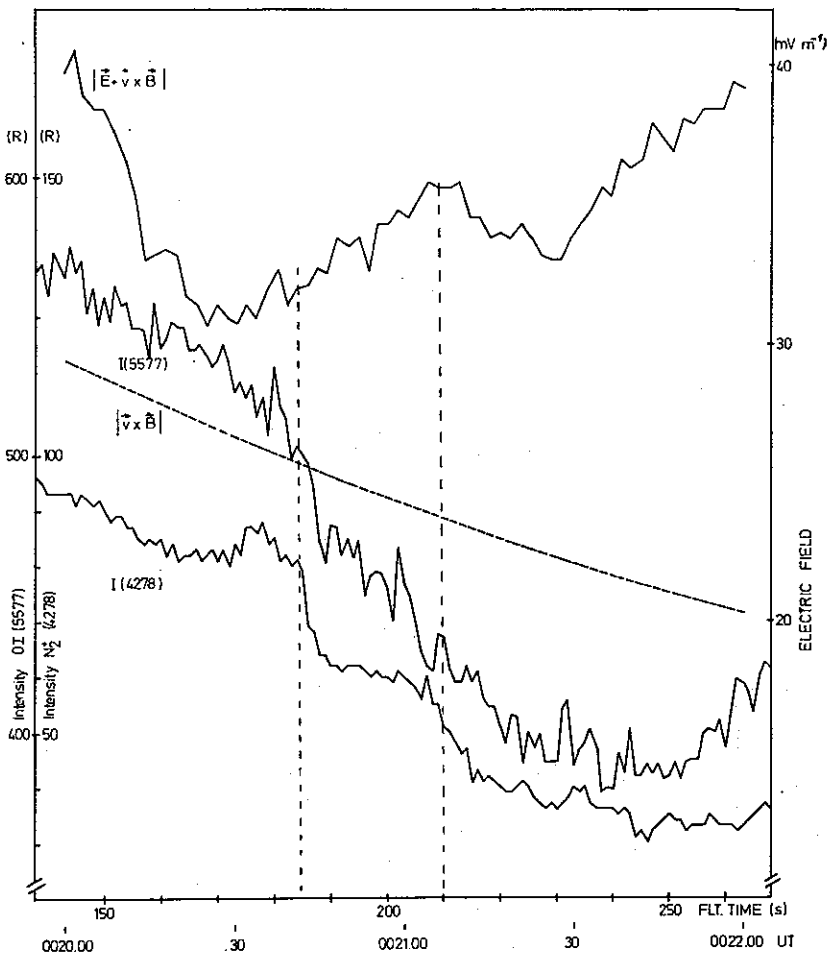

Fig. 5.15. Observed variations in auroral intensities and the electric field when the rocket F24 penetrated the structural region. The field values are averaged over one spin period (1.8 s) while 1 s smoothing is used for the optical emissions. The locations of the auroral forms are indicated by the vertical lines.

the aurora (*cf.* Fig. 2.1.c), or variations in the rocket attitude, and it is therefore concluded that the rocket in the flight period 150 to 220 s penetrated a region where auroral structures were superimposed on the homogeneous glow (*cf.* Måseide *et al.* 1973).

Figure 5.15 shows a high time-resolution plot of the field and photometer recordings at 5577 Å and 4278 Å when the rocket was in the structural region. The electric field is averaged over one spin period (1.8 s) while the optical recordings are smoothed over 1 s. It can be seen that the rocket passed through a double structure in the DC electric field, with two minima at 175 and 230 s separated by a small maximum at 210 s. Notice also, especially between 160 and 200 s, that some small-scale fluctuations in the range 0.1 to 0.3 Hz are observed.

The main features in the optical recordings are:

i) During the two intervals, 150–170 s and 190–210 s, the light intensity decreases fairly steadily.
ii) Two abrupt changes at 185 and 210 s, respectively, are seen in the 4278 Å emission, while the 5577 Å intensity decreases markedly slower.
iii) A small maximum is found between 175 and 185 s in the N_2^+ emission which is not observed in the oxygen line.

The assumed auroral situation can be represented in a somewhat simplified picture, qualitatively shown in the geometrical sketch in Fig. 5.16. Two auroral structures of roughly 5 km widths and separated by about 20 km are penetrated by the rocket. This picture explains the 4278 Å observations fairly well. Comparisons

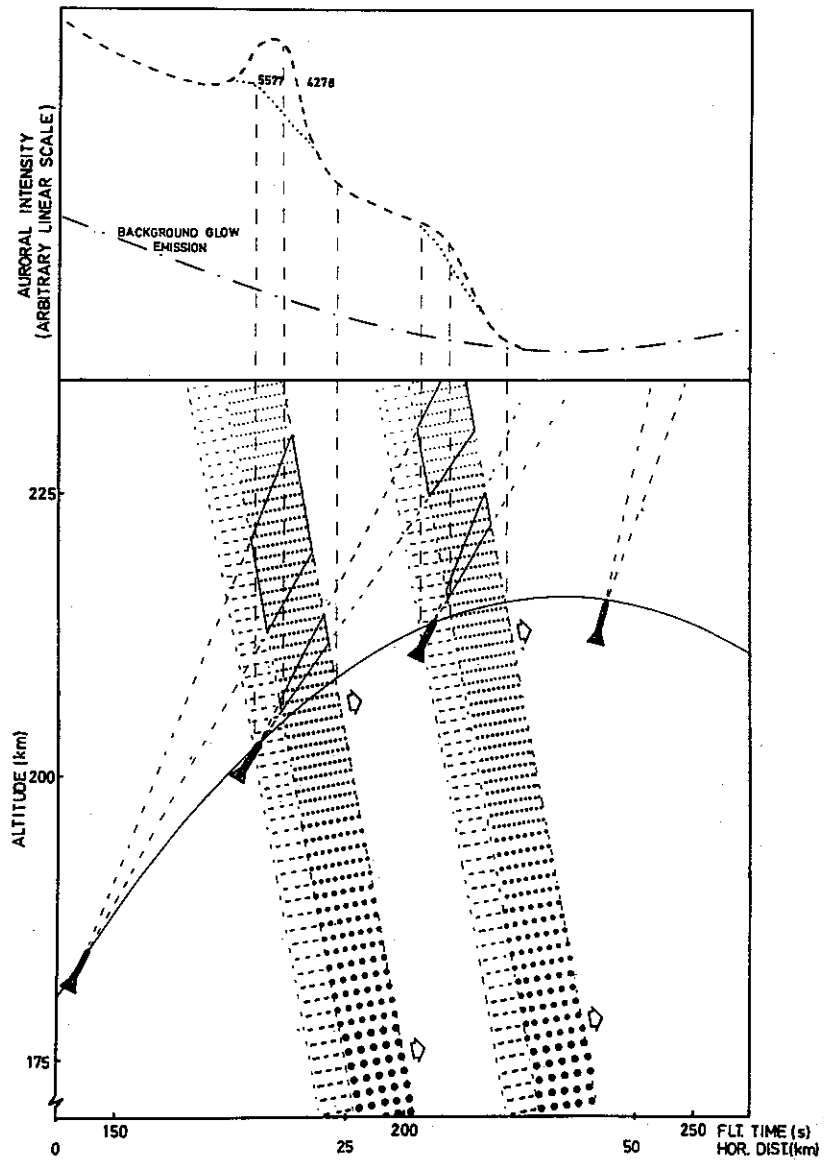

Fig. 5.16. A qualitative sketch for the F24 event, showing the assumed geometrical configuration between the auroral structures and the photometer's field of view when the rocket penetrates the auroral forms. The corresponding optical recordings are shown at the top of figure in a simplified version. The auroral structures are represented by dashed (5577 Å) and dotted (4278 Å) areas, indicating a partly spatial separation of the OI (5577 Å) and the N_2^+ (4278 Å) emitting regions due to auroral movement.

with the green oxygen line indicate that the auroral structures move in the same direction as the rocket (*i.e.* northward motion). This conclusion is based on the fact that the lifetime for the excited OI (^1S) is about 0.7 s compared to a lifetime of the $N_2^+(B^2\Sigma_u^+)$ being of the order of 10^{-7} s (*cf. e.g.* Omholt 1971); thus the OI (5577) emission has a natural time lag compared to the N_2^+ (4278) emission. This time lag together with a northward movement of the auroral forms can explain the difference observed between the two emissions.

From Figs. 5.15 and 5.16 the following conclusions concerning the DC electric field in and near the auroral forms can be drawn.

a) The field decreases as the rocket approaches the auroral structure and it reaches a minimum of just a few mV m^{-1} when the rocket enters the first auroral form. The field minimum is actually observed when the rocket is in the 5577 Å time lag structure.
b) Between the two forms, the field increases slightly, and a peak is observed when the rocket enters the second auroral form.
c) Again the field starts to decrease and a minimum is observed when the rocket passes the northern edge of the second form.
d) During the rest of the flight the field increases slowly while the overall auroral emissions decrease correspondingly.

In comparing these results with previous findings of *E*-field behaviour in auroral forms (*cf.* Sect. 5.4) the overall glow aurora must be considered in addition to the weak enhancements. Any model using loading of a current generator depends on enhanced ionization in the *E*-region, since the perpendicular conductivities in the *F*-region will be too low, due to reduced collision frequencies, to permit a significant increase in the current. The increase in *E*-field and the reduced auroral intensity during the last part of the flight indicate this effect. The observed relation between the aurora and the *E*-field is, however, somewhat confused, with a minimum of the field inside the first form and a local maximum inside the second one. Even though the rocket was above the *E*-region when penetrating the auroral forms, the particle spectrum in these forms will most probably also contain particles with sufficient energy to penetrate to lower altitudes and cause *E*-region ionization. The particle flux and the extent of the ionization can, however, be different in the two forms. A more unified picture may also be obtained if the whole region, from the southernmost boundary of the first form to the northernmost rim of the second one, is defined as *one* 'auroral region'. In this case the overall behaviour of the field will be that it increases with decreasing glow aurora. However, in the auroral forms superimposed on the glow, the field has local minima at the edges of the structured region. The direction of the field is, in the main, preserved inside the aurora, but a slight shift towards southwest can be seen.

5.6.2. *Electric fields and particle measurements in the F23 event.* The electric field observed in the F23 event is, in accordance with the general ionospheric conditions, much more variable over short distances and/or time. Figure 5.17 shows the total field measured in the spin plane, together with the magnitude of the $\mathbf{v} \times \mathbf{B}$ component. The conspicuous change in field strength which takes place around 2223.45 UT naturally divides the record in two parts, a low intensity region before this change and a more vigorous last section of the flight. In the first part variations in the field from a few mV m^{-1} to approximately 20 mV m^{-1} takes place, and the general trend in the record is towards a steadily increasing field.

With the sudden change in field strength the amplitude reaches a magnitude of almost 100 mV m^{-1}. From this peak value a decrease of the field, with rapid fluctuations with peak to peak amplitude of about 5 mV m^{-1} superimposed, takes place. Towards the end of the flight some more violent field variations again appear.

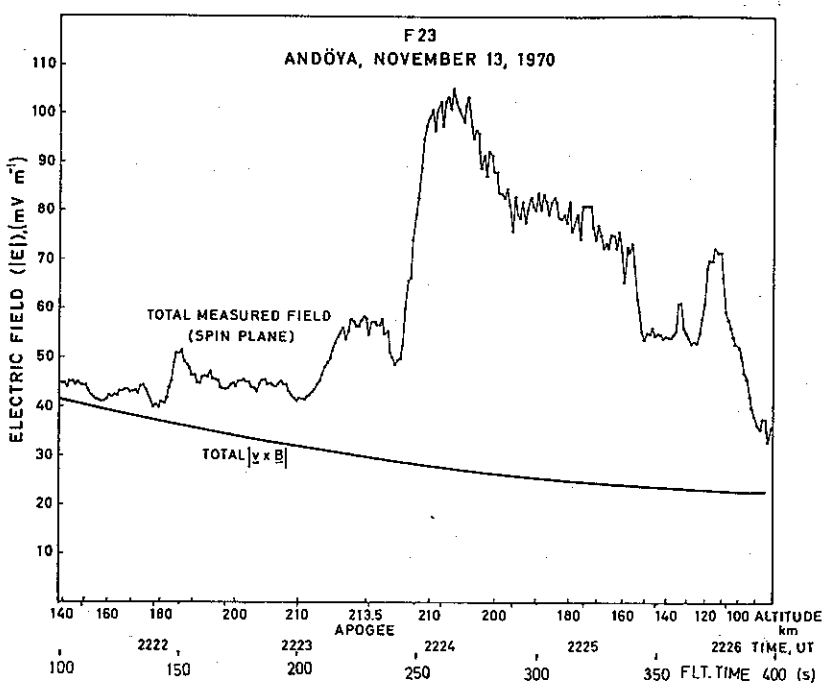

Fig. 5.17. Total DC electric field measured in the spin plane for the rocket F23. The calculated $|\mathbf{v} \times \mathbf{B}|$ contribution is also shown.

The drastic change in electric field strength happened approximately at the same time as the sudden increase in magnetic H-deviation and riometer absorption started. According to the onboard low energy particle detectors this event did not give rise to an increased precipitation of low energy (< 15 keV) electrons (*cf.* Maynard *et al.* 1973). The ground observed magnetic field variations are therefore in this case believed to be more associated with an increased electric field, than with changes in the ionospheric conductivities.

Before the abrupt change in the field strength the general tendency in the record was for the field to slowly increase. The detectors monitoring low energy particles (protons and electrons in the range $\sim 0.5 - \sim 15$ keV) showed at the same time on the average a steady decrease in the countrate (Maynard *et al.* 1973). Superimposed on this declining curve are, however, several short time variations, most having no obvious relation to the changes in the electric field. Of interest is, however, a peak in the electron spectrum between approximately 3 and 6 keV which appears between 150 and 200 s in flight time (Fig. 5.18). If we compare this with the E-field record we find that around these two times small minima appear in the field strength and that the amplitude stays at a somewhat increased level in the interval between. As electrons in just this energy range are most actively involved in the production of oval aurora (Deehr et al. 1970), this region may well be associated with an auroral structure. If this is the case a situation quite similar to that which appeared in the F24 event is present, *i.e.* the field has a minimum value near the boundaries of an auroral region.

5.6.3. *Concluding remarks.* The observations do not bring forward any clear relation between the electric fields, aurora, and auroral particles. In the main they seem to support the assumption of a decreased field in auroras, but this picture can be rather mixed up. One should, however, be aware of the importance of the height of the auroral emissions, or the energy of the primary particles, in this connection. Local effects, such as polarization fields and potential differences caused by different parallel conductivities along different L-shells must also be taken into account. Plasma instabilities may also give rise to perturbations in the large-scale electric field (*cf.* Sect. 8.2).

An interesting feature in the observations is the apparent minima seen in the field at the edges of an auroral region. Although small, these seem to be significant. In the current model proposed by Park & Cloutier (1971) (*cf.* Fig. 5.2), antiparallel Birkeland currents flow at the sides of an auroral region. It thus appears that the observed minima in the field may coincide with the location of Birkeland current regions. To make further con-

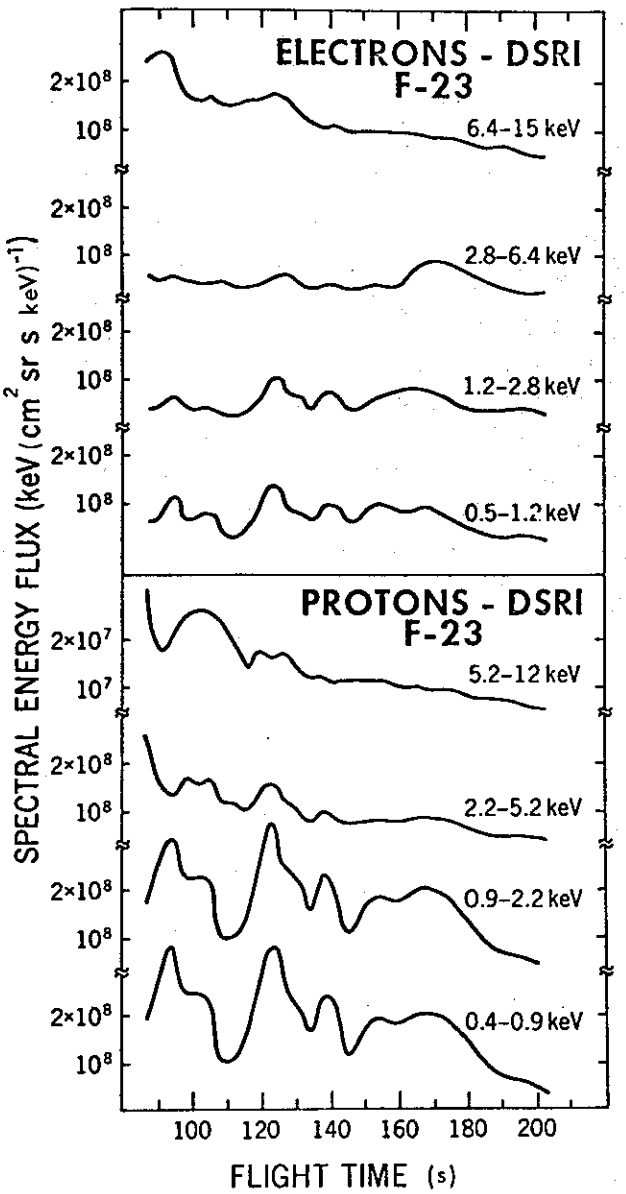

Fig. 5.18. Spectral energy fluxes as function of flight time for various electron and proton energies, measured during the flight of F23 (after Maynard *et al.* 1973).

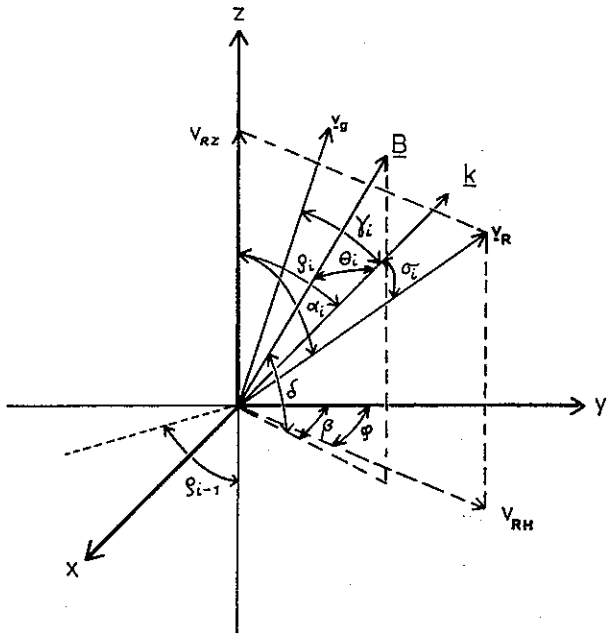

Fig. 6.1. Coordinate system and geometry of the propagating VLF wave and the rocket velocity used in evaluation of the Doppler shift data. The wave propagates in the *yz*-plane, the *xy*-plane is parallel to the bottom of the ionosphere.

clusions concerning this relationship it is, however, necessary to have more detailed information about the electric field, particle fluxes, and energies, together with precise vectorial measurements of the magnetic field.

6. VLF DOPPLER OBSERVATIONS OF IONIZATION MICROSTRUCTURES

6.1. *Introduction*

The AC experiment also provides possibilities for receiving signals from ground-based VLF transmitters. The received frequency, f', will, however, generally be different from the transmitted value f_o. The frequency shift is a function of the linear (v_R) and angular velocities of the rocket receiver, and the phase velocity of the wave (v_{ph}); properties of the medium along the propagation path will also have influence on the received wave (*cf.* Holt 1973). As $v_{ph} = f(n)$ (n is the refractive index), it is in principle possible to calculate the local electron density from Δf ($= f' - f_o$) when the other quantities determining n, in addition to wave path, receiver attitude and velocity are known. These requirements are rather severe and difficult to fulfill, due to the fact that VLF propagation in the lower ionosphere is not fully understood. For interpretation of the data one will therefore have to restrict oneself to regions and cases where a simplified theory can be used.

One advantage of this technique is that it is technically simple. For slowly varying ionospheric conditions, temporal variations in the propagation medium over the duration of a rocket flight can be neglected. If effects caused by the fact that the wave path is not coincidental with the rocket trajectory is disregarded (this will mainly cause a systematic error), variations in the frequency shift can be ascribed local effects. The technique is therefore well suited for studying small-scale structures. Both earlier use of the technique (*e.g.* Egeland *et al.* 1970) and the behaviour of the frequency shift around the top of the trajectory show that our assumptions lead to reasonable results.

6.2. *The Doppler technique – theoretical background*

In the following we will make use of a Cartesian coordinate system with a vertical z-axis. The geometrical configuration is as shown in Fig. 6.1. The wave propagates in the yz-plane, and horizontal stratification is assumed.

With the assumptions introduced above, the frequency shift experienced by the rocket-borne receiver will partly be due to the rocket spin frequency, f_s, and partly due to classical Doppler shift, Δf_D. For a homogeneous, isotropic medium this can be expressed as

$$f' - f_o = \Delta f_D \pm f_s = -f_o \frac{v_R}{v_{ph}} \cos\sigma \pm f_s$$

$$= -f_o \frac{v_R}{c} n \cos\sigma \pm f_s , \qquad (6.1)$$

where σ is the angle between wave normal, **k**, and $\mathbf{v}_R$ (*cf.* Fig. 6.1).

If the ionosphere is divided into thin slabs where the refractive index is constant, Snell's law states

$$n_i \sin\varrho_i = \text{constant} = \sin\varrho_o . \qquad (6.2)$$

ϱ_o is the incident angle of the wave normal at the bottom of the ionosphere and ϱ_i is the angle be-

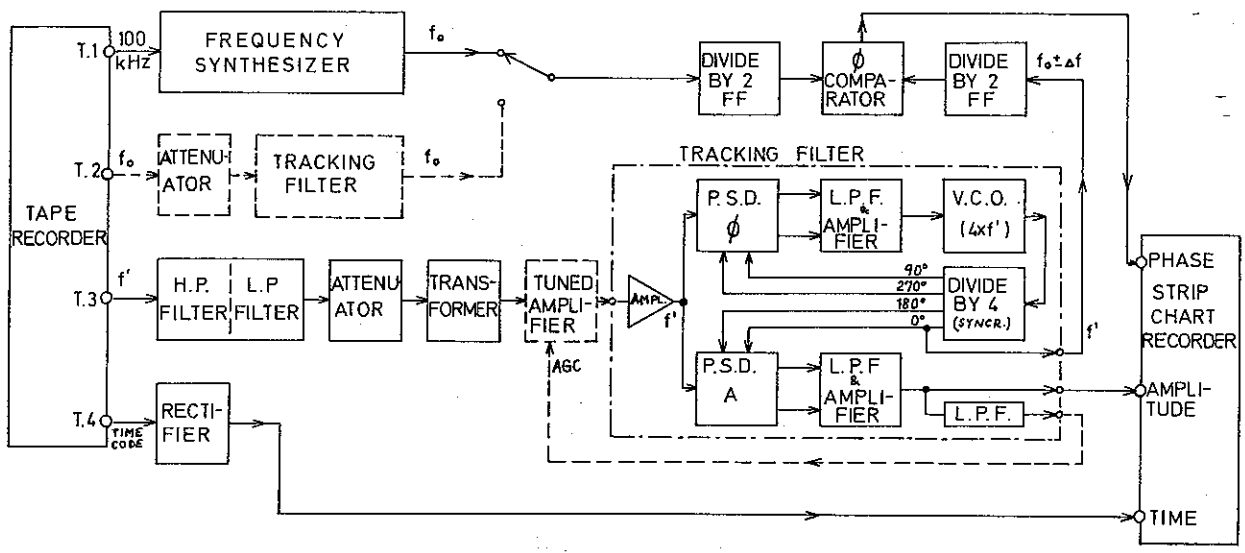

Fig. 6.2. Block diagram of analyzing equipment for VLF Doppler shift measurements.

tween the z-axis and $\mathbf{k}$ in slab number i. σ can be found through the product of the two unit vectors defining the angle. Using Fig. 6.1 one arrives at the following relation:

$$\cos \sigma_i = \hat{\mathbf{k}} \cdot \hat{\mathbf{v}}_R = \sin \varrho_i \sin \alpha_i \cos\varphi + \cos \varrho_i \cos \alpha_i \,. \quad (6.3)$$

In a similar way the angle between $\mathbf{k}$ and $\mathbf{B}$ can be found,

$$\cos \theta_i = \hat{\mathbf{k}} \cdot \hat{\mathbf{B}} = \sin \varrho_i \cos \delta \cos \beta + \cos \varrho_i \sin \delta \,. \quad (6.4)$$

The inclination of the magnetic field, δ, the angle between the plane of propagation and the meridian plane, β, the angle between the plane of propagation and the plane of the rocket trajectory, φ, and the angle between the rocket velocity vector and the vertical, α, are either known or can be read out from the rocket data.

From Eqs. (6.1), (6.2), and (6.3) the following expression can then be derived for the refractive index:

$$n_i^2 = \sin^2 \varrho_o + \left(\frac{\Delta f_D \, c}{f_o \, v_R \cos \alpha} - \frac{\sin \varrho_o \sin \alpha \cos \varphi}{\cos \alpha} \right)^2 . \quad (6.5)$$

The refractive index can thus be found from the Doppler shift of the received wave if the angle of incidence at the bottom of the ionosphere is known. From this we can further calculate ϱ_i and σ_i.

The relation between the electron density and the refractive index in the classical magneto-ionic theory is expressed in the Appleton–Hartree (A–H) equation (*cf. e.g.* Ratcliffe 1959*b*). As $f \gg f_{ci}$ in our case, the effects of ions are neglected. Because of the complexity of the complete A–H expressions we will only look for regions where the quasi-longitudinal (QL) approximation is valid, *i.e.* when the direction of propagation is sufficiently close to the earth's magnetic field to permit dropping terms containing $\sin \theta$ in the A–H equation.

The validity of the QL approximation for VLF waves has been investigated by *e.g.* Jørgensen & Ungstrup (1966) for various ionospheric conditions. They found the approximation valid for a great range of angles, and that it is quite easily satisfied above the *D*-region during disturbed conditions, and from the upper *E*-region in a quiet ionosphere. Even though A–H theory is not strictly applicable on VLF propagation in the lower ionosphere, it has been shown to give good results in and above the *E*-region (Egeland *et al.* 1970). The A–H formula for the refractive index for the whistler mode can in the QL approximation be written in the simple form (Ratcliffe *loc. cit.*)

$$n^2 = \frac{f_{pe}^2}{f\left(f_{ce} \cos \theta + \dfrac{\nu}{2\pi} \right)} , \quad (6.6)$$

where θ can be found from Eq. (6.4). Combining Eqs. (6.1), (6.6), and (3.15), N_e can be expressed explicitly as

$$N_e = \frac{4\pi^2 \varepsilon_o c^2 m_e}{e^2} \frac{(f_{ce} \cos\theta + \nu/2\pi) \Delta f_D^2}{f_o v_R^2 \cos^2\sigma}. \quad (6.7)$$

6.3. *Recording and analyzing instrumentation*

The rocket instrumentation for these measurements was connected directly to the AC electric field experiment (*cf.* Fig. 5.13). Direct modulation of the rocket transmitter by the received signal instead of via a subcarrier oscillator made it possible to transfer the raw signal to the ground station. We thus avoided any reduction of the data in the rocket, where this process is difficult to control and where systematic and random errors can easily be introduced, for instance by drifts in crystals providing reference signals. The rocket electronics could then be made fairly simple, and consisted in principle of band-pass filters and tuned AGC amplifiers.

On the ground the analogue VLF rocket signal was recorded together with the ground wave from the VLF transmitter and a local reference frequency (100kHz).

To determine the Doppler shift the following technique is used (*cf.* Fig. 6.2): After band-pass filtering and proper amplification the data are fed into a tracking filter. The phase-locked signal thus obtained is then compared in a linear phase comparator with a reference frequency, which either can be the ground-recorded VLF wave, or it can be derived from the recorded 100 kHz by a frequency synthesizer. The linear ramp output from the phase comparator is fed to a strip chart recorder together with the tracking filter amplitude and the time-code.

In the present investigations two VLF transmitters in Northern Norway, JXZ at 16.4 kHz and OMEGA at 12.3 kHz (F24 only), were received. The transmitters are located approximately 250 (JXZ) and 400 km geomagnetic southwest of the launch site. During the rocket flights the transmitters were operated in continuous wave mode. The frequency stability is better than 10^{-10} for both transmitters.

Figure 6.3 shows an example of data recorded during the F23 flight. It can be seen that the amplitude is spin modulated, but this is not very pronounced. The saw-tooth shape of the phase trace appears as the comparator is reset when its value surpasses 4π. (The large oscillations at the beginning and end of each ramp are inherent in the analyzer as it makes a transition from one phase range to another.)

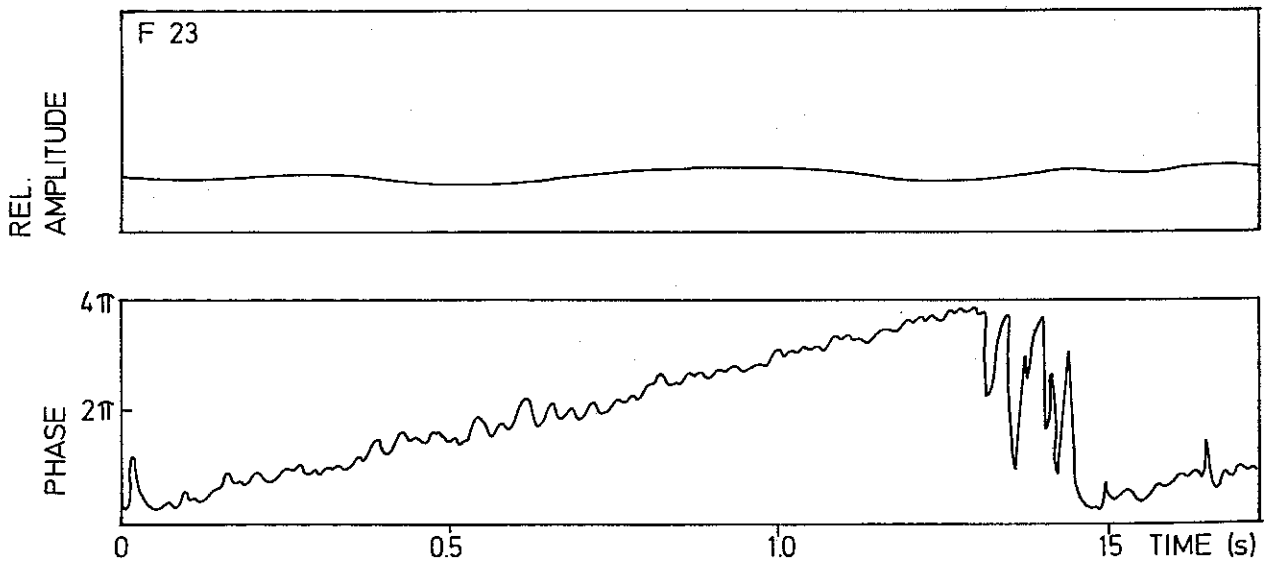

Fig. 6.3. Example of data from the Doppler shift analyzer. The upper curve shows the amplitude of the signal, while the slope of the lower curve represents the phase shift of the received wave relative to a reference signal. In this case the reference was the ground wave from the VLF transmitter received simultaneously with the rocket signal.

The Doppler shift is the first derivative of the phase with respect to time. Thus, one can obtain a good estimate of Δf by evaluating the slope of each ramp. For the example shown in Fig. 6.3, Δf is, for instance, 1.47 Hz. By this simple technique the Doppler shift as a function of time can be obtained, and from geometrical considerations, information about the rocket trajectory, and using Eq. (6.7) the mean electron density profile can be derived.

6.4. *Microstructures in the electron density distribution.*

This method for deriving the Doppler shift (cf. Sect. 6.3) smooths out small-scale variations in the trace, variations which visual inspection of the record clearly shows are present. Besides this, there is also a fundamental objection to the use of such a subjective procedure as drawing a straight line fit.

To provide more objective measurements with better time resolution, the phase data from F23 have been digitized at 8 ms intervals using a semi-automatic chart digitizer. (An 8 ms sampling interval means a Nyquist frequency $\left(f_N = \frac{1}{2\Delta t}\right)$ of 62.5 Hz, and low pass filtering prevents aliasing.) The data processing is then accomplished by a computer, after spurious and 'bad' elements in the phase data have been identified and rejected.

Examples of Doppler frequencies derived in this way are shown in Fig. 6.4. This sample is recorded near 100 km on the downleg of F23. The average Doppler shift during this interval was 1.44 Hz, which corresponds to a mean electron density of $3 \cdot 10^{10}$ m^{-3}. The striking thing in this display is the variability of the frequency shift, giving evidence of a highly irregular electron distribution. This seems to be characteristic of the processed phase data between 110 and 95 km. Typical values of a few per cent are found for the relative density variation in these fluctuations.

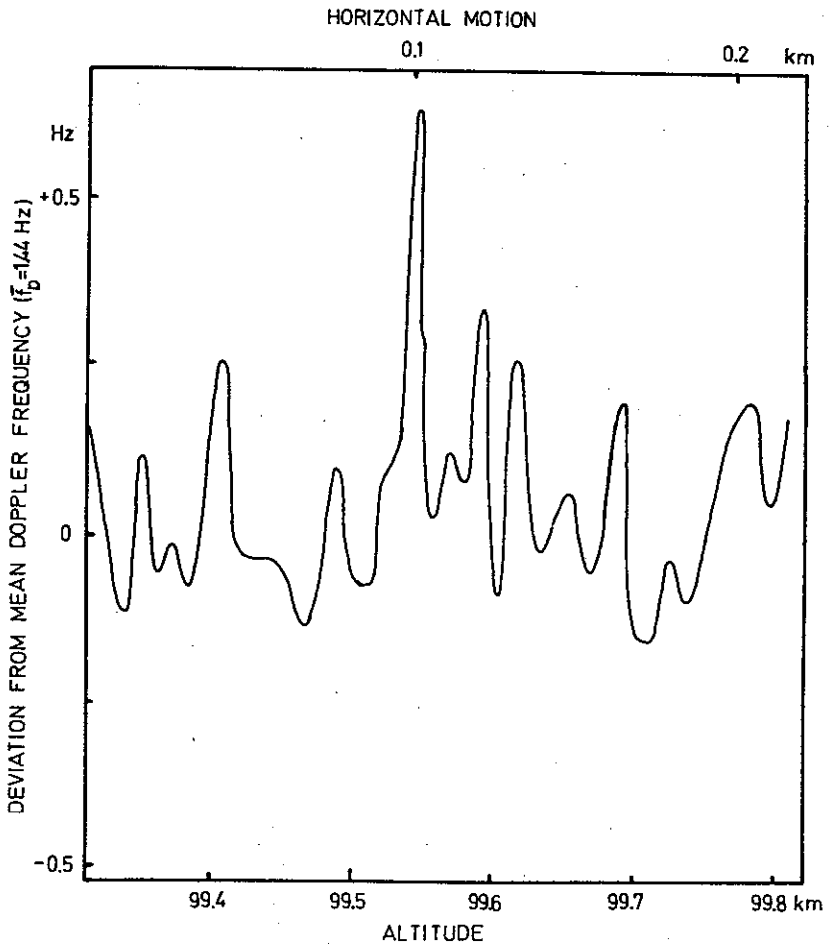

Fig. 6.4. Small-scale fluctuations in the observed Doppler shift as function of altitude measured from F23. The horizontal motion of the rocket is given at the top of the figure.

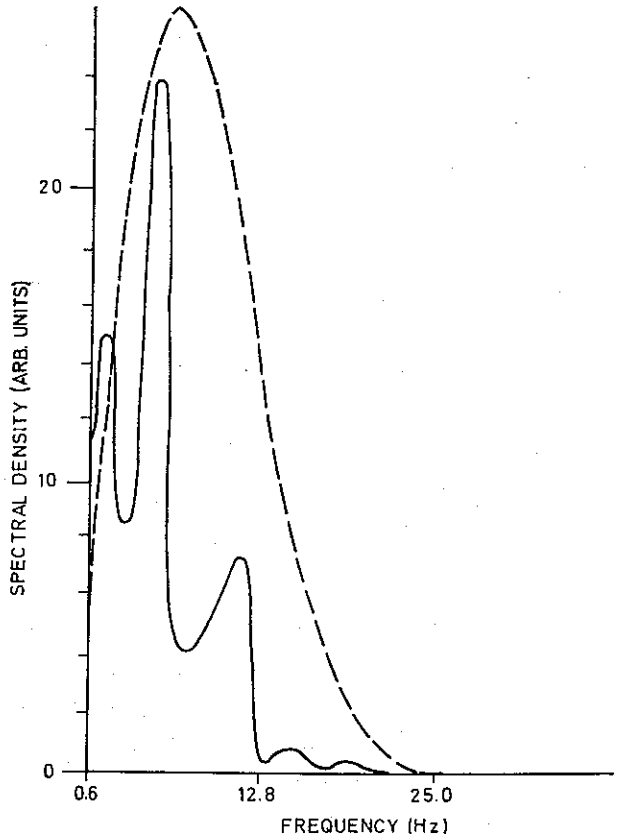

Fig. 6.5. Spectral density of the variance of the Doppler shift around the part of the measurements shown in Fig. 6.4. The amplitude response of the processor is shown in the dashed curve.

The variance spectral density for an altitude just above 100 km is shown in Fig. 6.5. The peaks occurring at 1.83, 5.47, and 11.55 Hz are all statistically significant and appear to be fairly typical for the variance also at other altitudes. It may be noted that the first and second peak is about 2 and 6 times the spin frequency. From Fig. 6.4 it can, however, be seen that variations more rapid than those corresponding to the 11.55 Hz peak are present, but these fluctuations do not possess the necessary regularity to give peaks in the integrated power spectrum.

In an attempt to interpret these observations we will assume that temporal variations can be neglected. If the fluctuations are caused by time variations in the medium along the ray path, this should also give effects on the phase data at other altitudes. The observed effects are thus believed to give a picture of spatial structures.

The first question is how the spin dependence can come into the data. The location of the transmitter with respect to the receiver will introduce a direction effect. This should, however, only show up on the amplitude (where it also can be seen (*cf.* Fig. 6.3)) and not on the phase records. Artificial effects can be introduced if the instrumentation goes into saturation, but this was far from being the case in the present situation. Another place where such effects could leak in is through the saw-tooth form of the phase record, which actually is a sum of sinusoids. This possibility has been investigated, and rejected.

If we take the spin-controlled phase variations to be real, and have the other observed structures in mind, it is difficult to explain the spin variations if the irregularities are supposed to be present as horizontal slabs, *i.e.* microstructures in the vertical electron distribution. In such a case the rocket would descend through micro-layers with dif-

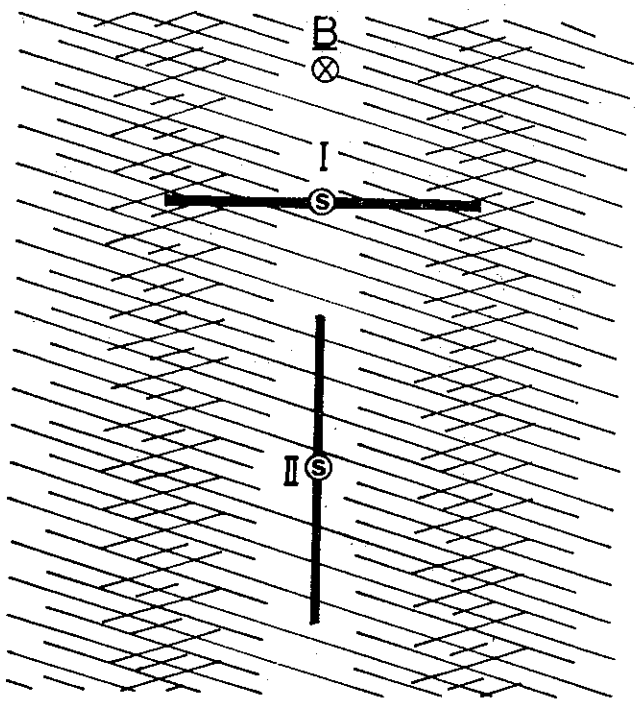

Fig. 6.6. Schematic illustration of how rotation of the spacecraft (S) in a medium with field-aligned structures can result in variations in the density seen by the probes. The situation is viewed along the magnetic field lines, and the instrument carrier is in a region with low electron concentration. In position I the probes will feel a dense plasma, while a 90° rotation to position II will bring the probes into a thinner medium. The forms of the structures are stylized. These are probably of more elliptic shape (Egeland 1962b) with length of the shortest axis of the same order as the probe dimension.

ferent density, and within each layer the orientation of the antenna would be of no importance. If, however, the structures consist of field-aligned ellipsoids, with shortest horizontal dimensions of the same order as the antenna length, a spin effect will be introduced. In this case the rotation of the antenna will take it through regions of different density (*cf.* Fig. 6.6), causing variations in the phase of the wave. If the rocket is in a region of maximum density, *i.e.* inside an ellipsoid, a rotation of the probes from a direction parallel to the major axis of the ellipse to a direction perpendicular to this, will move the probes from a position completely within a maximum region to where it is partly outside this. This will give a phase variation with period twice the spin period. The first two peaks in the variance spectrum corresponds to the first and third harmonics of this frequency. The horizontal motion of the rocket, which takes it through the slabs, will complicate the picture, and this may give rise to 'odd' peaks, as the one at 11.55 Hz.

The spin modulation in the phase data will thus favour the assumption that field-aligned microstructures were present in the electron distribution. Figure 6.4 shows that the dimensions of these irregularities were at least down to 10 m. This is also the spatial resolution of the recording and analysing technique used.

If we compare this with the AC electric field measurements described in Chapter 2, we will find that these two observations strongly support each other. The AC measurements showed the presence of ELF wavefields at *E*-region altitudes. These fields which are supposed to have their origin in electrostatic waves propagating within a horizontal layer, may modify the electron distribution and bunch electrons in field-aligned structures, just as shown by the Doppler shift measurements.

The presence of such microstructures in the electron distribution in the auroral *E*-region has also been reported by McNamara (1971). His recordings were based on in situ measurements with rocket-borne Langmuir probes. In connection with visual auroras irregularities with dimensions from 10^{1} to 10^{-1}m were detected in the altitude region from 95 to approximately 120 km.

7. STRUCTURES IN THE AURORAL *E*-REGION

7.1. *Introduction*

The auroral ionosphere is subjected to so many structural variations that it may seem odd to talk about irregularities, because it is hard to find any 'regular' ionosphere, even during quiet conditions. Looking for other registrations of ionospheric structures which may be related to our findings, and which may add to the understanding of the ELF *E*-layer noise, observations showing horizontal structures in the *E*-region with dimensions less than 100 m will be briefly reviewed.

The phenomena which will be considered in this chapter are: 1) optical aurora, because this gives the most conspicuous forms of *E*-region irregularities; 2) particle precipitation, because this is the most direct way of producing irregularities; and 3) VHF and UHF scattering (radio aurora), because radio scattering provides information about microstructures in the ionization. However, when comparing measurements of various kinds one should always be aware of the limitations implied in the physical nature of the observations. This will not only include spatial and temporal limitations. Production of visible aurora requires a fairly large flux of particles within a certain energy range. Thus, the aurora only maps out the patches in the precipitation pattern where these conditions are satisfied. In particle measurements one is also in practice working with a limited number of energy ranges, while in radio measurements the scattering process is highly sensitive to the dimension of the irregularities compared to the radar wavelength. Thus, what stands out as a dominating effect in one type of investigations may not be a major feature in the total picture.

7.2. *Small-scale structures in optical aurora*

Although structures and forms are almost always present in auroral displays and can easily be observed visually, it is not easy to perform accurate measurements of these properties. The main reasons for this paradox is the limited instrumental resolution both in space and time in the most commonly used observation techniques,

photometers, and photographic cameras, and the difficulty in distinguishing between spatial and temporal variations. This has been improved considerably by the development of television (TV) techniques for auroral observations (*cf. e.g.* Davis 1966). With this method the resolution is about 0.03° during favourable auroral conditions, which corresponds to 70 m at an altitude of 100 km.

Maggs & Davis (1968) have made an extensive study of the thickness of auroral structures by means of a TV image orthicon system. All observations were made strictly in magnetic zenith, and besides the TV, all-sky cameras were used to classify the aurora according to brightness and form. An important result from these measurements was that the aurora often appeared more rayed and structured than when observed visually. The range of thickness was found to extend from the instrumental resolution limit (70 m) to approximately 4.5 km, with the median value being 230 m. The distribution of thickness of all forms is shown in Fig. 7.1. As all systematic errors in the observations will go in the direction of too large values, it is clear from this figure that structures thinner than 70 m may be a common phenomenon.

TV observations have also revealed that visually observed homogeneous arcs are often composed of parallel, thin arc-like structures (Davis 1967). The structures often appear to be streaming horizontally, parallel to the orientation of the auroral form.

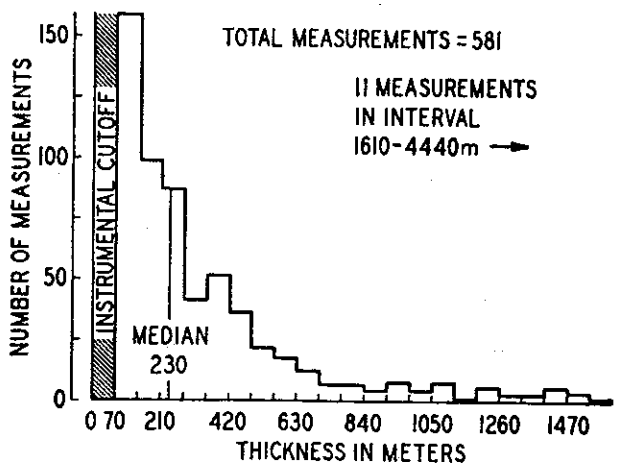

Fig. 7.1. Distribution of thickness of auroral forms as measured by Maggs & Davis (1968).

Altogether it can be stated that microstructures in aurora appear much more frequently than has been commonly believed. Furthermore, structures with dimensions down to order of 10 m may very well be present. The origin of the perturbations may be microstructures in the neutral atmosphere, in which case transport processes will most probably smear out the picture rather soon, it may be plasma instabilities, or it may be found in the source of ionization and excitation, *i.e.* in the precipitating particles.

7.3. *Finestructures in particle precipitation*

A lower limit for structures in particle precipitation is set by the gyro radius of the primary particles. This means that we only have to consider electrons in connection with small scale variations. As the altitudes of interest in connection with the *E*-layer noise is between 95 and 130 km we mainly have to deal with electrons with energies between 3 and 15 keV (*cf.* Sect. 3.4).

The gyro radius of a 10 keV electron in the earth's magnetic field in the auroral zone will be about 6 m or less, depending on pitch angle. We are thus within the range found in the irregularities associated with the ELF *E*-layer noise. However, when looking at distribution and dynamics of particle precipitation observed by polar orbiting satellites (*cf. e.g.* Hultqvist 1972 for a review) one is often surprised by the lack of finestructure in the records. This can partly be due to the effect that when overlooking the whole particle shower, the peaks giving rise to *e.g.* visible aurora, will not look so very spectacular. Another fundamental reason is, however, the smoothing introduced when integrating the satellite data, which together with the high speed of a satellite (~ 8 km s^{-1}), gives relatively poor spatial resolution. This means that to study microstructures in the precipitation we have to use rocket observations, where the lower limits of temporal and spatial resolution may come down to about 1 ms and 1 m (Evans 1971). However, the difficulty in distinguishing between variations in time and space introduces a problem in the interpretation of data.

From numerous rocket flights during the last

ten years it is evident that small-scale structures are commonly seen in the particle precipitation (*cf. e.g.* Mozer 1968; Evans 1971). The most violent and conspicuous fluctuations seen over the range of metres or ms seem, however, to be temporal effects. Nevertheless, weaker spatial structures, ranging down to the particle gyro radius, can be seen superimposed on larger forms (Evans, *loc. cit.*). These may be the particle analogy to the finestructure in luminosity revealed by the TV studies.

From the last two sections it can be concluded that structures in particle precipitation cannot be ruled out as a source of the irregularities associated with the ELF *E*-layer noise. If this is the case, it is, however, an open question why the ELF irregularities are only observed in the *E*-region. Diffusion at the higher and turbulent mixing at lower altitudes (*cf.* Sect. 3.2.) may be an explanation, but it does not sound very probable. Furthermore, it is not likely that direct production of structures by precipitating particles should give rise to irregularity spectra which, during so different conditions as in the present cases, should exhibit the observed similarity. Neither that it should extend over such a wide area as that covered by the rocket S70/1, from its ascent to its descent crossing of the *E*-region.

7.4. *Radio aurora*

VHF (30–300 MHz) and UHF (0.3–3 GHz) radio waves which have been scattered from the ionosphere contain information about the scattering region, and may thus be a valuable tool in ionospheric studies, if the reflecting mechanism is sufficiently understood. The measurements are made by high-power radar systems with large narrow-beam antennas (typical beamwidth 0.5–10°). The transmitter may either be pulsed, which will give good range resolution if the pulse length is short, or operate on continuous wave. This is better suited for studying finestructure in the scattering process but involves the loss of echo range information. Waves reflected from auroral ionization are often called radio aurora.

7.4.1. *Observational characteristics of radio aurora.* Features in radio aurora related to ionospheric irregularities will now be summarized. One should, however, be aware of the complexity of the phenomenon, which makes it necessary to distinguish between various types of echoes in a more thorough study of the kind. (For radio auroral nomenclature, *cf.* IAGA 1968.) To avoid uncertainties introduced by *e.g.* refraction, critical reflection, and absorption, we will mainly regard measurements made with frequencies greater than approximately 100 MHz.

a) Height distribution: The main reflection height in radio aurora varies from approximately 100 to 120 km, with a vertical extent from 5 to 20 km. Radio aurora is thus almost exclusively an *E*-region phenomenon.

b) Magnetic aspect sensitivity: Experiments show strongest echoes when the radio beam is nearly perpendicular to the magnetic field line at reflection height (*e.g.* Chesnut *et al.* 1968). On the average an amplitude decrease of 10 dB/degree for small deviations from perpendicularity and 4–6 dB/degree for angles greater than 4° has been reported (*e.g.* Egeland 1973). However, in individual events several degrees departure from orthogonality has been observed (Forsyth & Lyon 1971).

c) Frequency dependence: Generally, the scattering strength of the radio aurora is much greater at low frequencies than at higher ones. Chesnut *et al.* (1968), using 6 frequencies between 50 and 3000 MHz, which corresponds to wavelengths from 6 to 0.1 m, found that the scattering power as a function of frequency could be expressed by the following analytical form

$$P(f) = P_o \exp[-f/f_o]\,. \qquad (7.1)$$

The quantity f_o, called the scale frequency, varied between 100 and 160 MHz with a most frequently observed value of 120 MHz (wavelength 2.5 m). In other cases it has been found that the frequency distribution follows a power law variation of approximately f^{-3} to f^{-4}.

d) Doppler spectrum: The spectrum of the returned signal may be Doppler shifted and/or broadened, positively or negatively. The Doppler shift is caused by large scale radial motion of the scatterers, while the Doppler spread indicates that the scatterers may also be moving relatively to one another. Doppler shift measurements generally show a shift in drift direction around midnight consistent with the auroral electrojet picture (*cf.* Sect. 5.2). The Doppler spectra show, however, a high degree of complexity (Balsley & Ecklund 1972). The spectrum may appear as a broad peak centered around the transmitted frequency, it may be flat over a large range, showing a smooth distribution of velocities in the scattering region, it may be rather wide but still peaked at a certain frequency, or it may finally be a clean line spectrum. In the cases where a pronounced peak appears in the spectrum, Doppler shifts corresponding to velocities as high as 1800 m s^{-1} have been seen (Camnitz *et al.* 1969), but typically the velocities are found to be between 350 and 460 m s^{-1} (Chesnut 1971). The variation of Doppler shift with azimuth angle will often follow a smooth curve with zero shift approximately in the meridian plane. (Chesnut *et al.* 1968). However, one will also frequently find cases where the Doppler shift is almost constant in magnitude, but experiences a sign change in crossing the magnetic meridian (Abel & Newell 1969).

e) Threshold effect: With high-sensitivity radars it is observed that when echoes are seen they are never below a particular amplitude (Leadabrand *et al.* 1965).

7.4.2. *Scattering mechanisms.* The complexity, and often even inconsistency, seen in the observations of radio aurora makes it unlikely that one and the same mechanism can be responsible for the variety of reflection patterns.

Radio waves transmitted onto the ionosphere will set free electrons into oscillations. The electrons will in time reradiate electromagnetic waves, and thus cause scattering of the wave energy. This effect, known as Thomson scattering or incoherent scattering, can be detected on the ground if sufficiently powerful transmitters and sophisticated receiving instrumentation are used. However, radar measurements in the electrojet regions show that the scattered energy during special conditions is far too high to be explained as incoherent scattering. One has therefore to look for collective reflection processes caused by increased ionization in the electrojet regions. The problem has been extensively studied, both theoretically and by experimental methods during the last decades (*cf. e.g.* Egeland 1962 *a*, *b*; Forsyth 1968; Unwin & Knox 1971).

In principle two different models have been proposed, namely: a) Under dense scattering from non-isotropic irregularities (Booker 1956). b) Scattering from irregularities caused by plasma instabilities (*e.g.* Bowles *et al.* 1963; Farley 1963).

a) In Booker's model, and in further development of this theory (Egeland 1962*b*), a three-dimensional autocorrelation function was assumed to describe the variations in the medium, and then, by a Fourier transform, the scattering coefficient was obtained. The autocorrelation function, which was chosen more for mathematical convenience than for physical significance, was

$$\varrho(x,y,z) = \exp\left[-\tfrac{1}{2}\left(\frac{x^2+y^2}{T^2} + \frac{z^2}{L^2}\right)\right], \quad (7.2)$$

which is axially symmetric about the z-axis (taken to be coincidental with the earth's magnetic field). T and L are the correlation distances transverse to and along the z-axis, respectively. Based on this function one will arrive at the following expression for the power scattering cross section, σ, (*i.e.* the power scattered per unit solid angle, incident power, and volume)(*cf. e.g.* Egeland 1973)

$$\sigma = \frac{1}{\lambda_{pe}^4}\left\langle\left(\frac{\Delta N_e}{N_e}\right)^2\right\rangle T^2 L \times \exp\left[-\frac{8\pi^2}{\lambda^2}(T^2+L^2\chi^2)\right] \quad (7.3)$$

for small deviations, χ, between the line perpendicular to the magnetic field and the direction of incidence of the wave. The symbols are: λ = the wavelength of the incident wave, λ_{pe} = the free

space wavelength corresponding to the electron plasma frequency in the scattering medium, and $\left\langle \left(\frac{\Delta N_e}{N_e} \right)^2 \right\rangle$ is the rms fractional variation in electron density.

Even though this model, with reasonable values of T, L, and $\frac{\Delta N_e}{N_e}$, can explain some of the observed features in radio aurora, as for instance aspect sensitivity, it is not capable of explaining other important characteristics as wavelength dependence and Doppler shift in the scattered signal.

A somewhat related model was developed by Moorcroft (1961*a*,*b*). The model permitted synthesis of any arbitrary random ensemble of under dense and over dense scatterers of any size, and with a gaussian ionization distribution. This generalization made the model more successful in fitting the observed features, but Moorcroft concluded in a critical review of the model (1966) that no possible combinations of scatterers could explain essential points in the frequency dependence in the observations. Furthermore, features in the Doppler shift (as the azimuthal variation) of the wave could not be explained by scattering from drifting irregularities, but required a mechanism which can regulate the motion of the scatterers.

b) These early investigations showed that even though the Booker–Moorcroft models could explain a great part of the data, a considerable amount of observations remained which could not be explained unless the scattering medium exhibited some periodic structure. This led to the postulation that plasma instabilities of some kind could set up wavefields in the medium and cause the necessary periodicity.

At this juncture we shall omit reference to the nature of the plasma instability (this will be discussed in the next chapter). We will only postulate a plane wave propagating with velocity v_{ph}, with wavefronts parallel to the magnetic field lines, giving rise to field-aligned structures in the electron distribution (*cf.* Fig. 7.2). The relation between the autocorrelation function of the scattering medium and the spectrum of its spatial

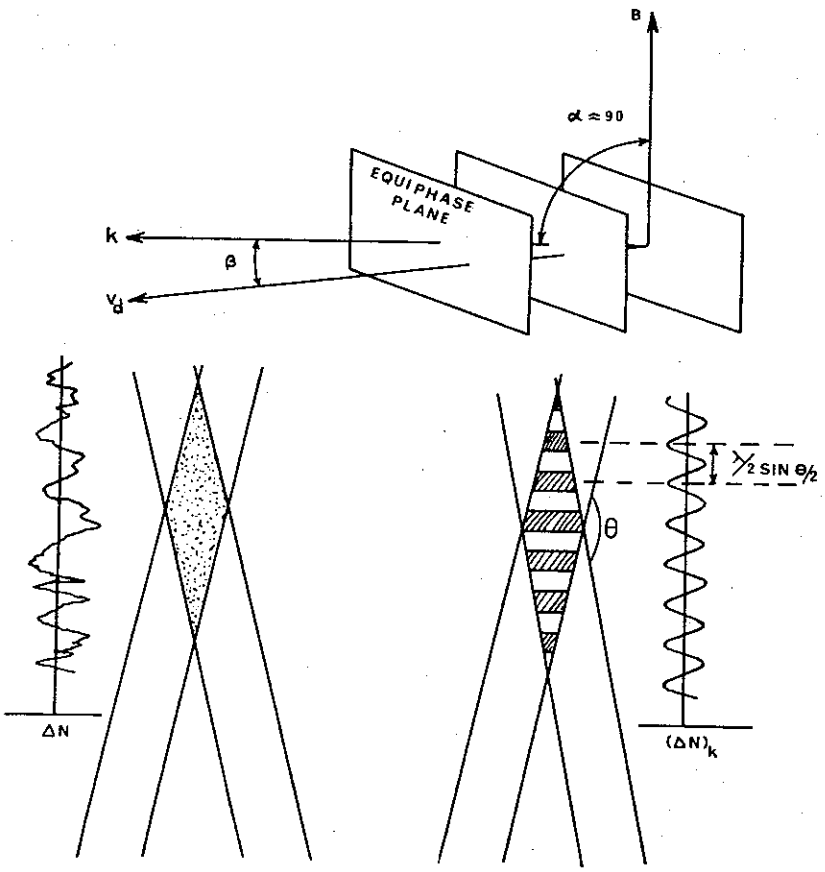

Fig. 7.2. Geometry of radar reflections from wave-generated irregularities. The lower part of the figure shows how the radar wave will only respond to the Fourier wavelength in the irregularities spectrum which is $\frac{1}{2}\,\lambda_{\text{radar}} \sin(\theta/2)$, where θ is the scattering angle (180° for backscatter) (after McNamara 1971).

fluctuations can be expressed by the Fourier transform (*e.g.* Booker 1956)

$$\varrho(r) = \int_{-\infty}^{+\infty} \exp[i\mathbf{k}\cdot\mathbf{r}]\, S(\mathbf{k})\, d\mathbf{k} \qquad (7.4)$$

$S(\mathbf{k})$ is here the three-dimensional spectral density function. Furthermore, for weak perturbations, the scattering cross section per unit volume is in the Born approximation

$$\sigma \propto N_e^2 \left\langle \left(\frac{\Delta N_e}{N_e}\right)^2 \right\rangle S(k_r)\,, \qquad (7.5)$$

where k_r is the radar wave number (*cf. e.g.* Flood 1967). The scattering cross section is thus proportional to the power spectrum of the electron density fluctuations evaluated at the radar wave number. However, the radar will not respond to the entire spectrum of density fluctuations. In order not to have destructive interference it will only select and measure the particular spatial Fourier component along the line of sight which corresponds to half the radar wavelength. It is indicated in Fig. 7.2 how the radar thus will resolve only particular spacings of plane wavefronts in an apparently random background medium.

A plasma instability, generating a limited spectrum of waves with a certain velocity, may thus explain the frequency dependence and the Doppler shift in the scatter measurements. If we compare this with the observations of ELF *E*-layer noise, we find that the altitude of our observations corresponds to the height region where one requires waves for the generation of scatterers. The wave velocity deduced from Doppler measurements is found to be on the order of 400 m s^{-1}. The horizontal dimension of the scatterer is on the order of $\gtrsim$ 1 m, which gives a rough estimate of the wave frequency $f \gtrsim 400$ Hz. This fits well with the frequency of the *E*-layer noise. It thus seems fair to accept as a working hypothesis that there is a connection between the *E*-layer noise and plasma instabilities giving rise to scattering of radio waves.

Furthermore, the scatter measurements support the statement that irregularities in the electron distribution with horizontal dimensions on the orders of one metre, or less, are frequently present in the auroral *E*-region.

8. PLASMA INSTABILITIES AND *E*-REGION IRREGULARITIES

8.1. *Introduction*

Both the AC electric field and the coherent scatter observations show that the *E*-region irregularities have preferred directions in space (*cf.* Sects. 2.4 and 7.4). In addition, a characteristic distribution of amplitude *vs.* spatial dimension is found. These are properties which may well be associated with wave motion. As the wave source, a plasma instability can be adopted. By the term plasma instability (or wave instability) we will in this context mean a process which causes a flow of energy from the plasma to a wave, resulting in a spontaneous growth of the wave amplitude. Seen from the wave this means that if the amplitude varies harmonically in space and time like $\exp[i(\omega t - \mathbf{k}\cdot\mathbf{r})]$, where ω is complex and $\mathbf{k}$ real, the wave will be growing if $Im(\omega) < 0$. The oscillation frequency will be $Re(\omega)$.

When a suitable range of ionospheric parameters is used, the instability theory should primarily be able to explain the observed spatial dimensions (or equivalently the frequency spectrum), direction dependence, and altitude distribution of the irregularities. Investigations on wave instabilities for application to coherent scattering have mainly been concerned with two different classes of instabilities, one which may be termed the crossed fields or gradient instability, and the other the ion wave instability.

8.2. *The crossed fields instability*

Simon (1963) and Hoh (1963) showed that an instability can arise in a plasma containing crossed electric and magnetic fields if the ionization has a gradient parallel to the electric field. A qualitative explanation of the instability can be given, based on the idealized situation shown in Fig. 8.1.a. A plasma slab, consisting of electrons and ions, with sharp boundaries, is under the influence of a homogeneous magnetic field, **B**, directed into the paper plane parallel to the slab boundaries, and an electric field, **E**, perpendicular

to these. This configuration will give rise to a Hall current towards the left. If a small disturbance occurs and perturbs the boundary, the Hall current will produce polarization fields, E', directed as shown on Fig. 8.1.b. The $\mathbf{E}' \times \mathbf{B}$ drift set up by these fields will produce a growth of the perturbation on the side of the slab where the applied electric field and the density gradient have the same direction. The opposite orientation is stable.

The application of the $\mathbf{E} \times \mathbf{B}$ instability to the ionosphere has been studied in great detail by Hooper & Walker (1971) and, in connection with radio aurora, by Unwin & Knox (1971) and Knox (1972). The geometrical configuration of a horizontal electric field (mainly in the meridian plane), a nearly vertical magnetic field, and a north-south gradient in the electron distribution associated with an auroral form, is here in accordance with the requirements for growth of instabilities.

Unwin & Knox (*loc. cit*) calculated the relation between the electric field and density gradient needed for onset of the instability at various wavelengths and related this to auroral forms of various widths and intensities. Some of their results are shown in Figs. 8.2 and 8.3. Taking the ionospheric conditions at the launch of *e.g.* F24 ($E \approx 30$ mV m^{-1}, auroral glow with faint structures, total intensity at 4278 Å during the last part of the flight < 1kR) it is seen from the figures that this instability cannot produce the structures and frequencies observed in the ELF *E*-layer noise.

It can then be concluded that even though the crossed fields instability can produce wave-like irregularities in connection with aurora, the frequencies of the waves which could be generated during the conditions present in the actual events will be far too low to explain the *E*-layer observations. It should, however, be noted that the small-scale structures observed on the DC field recordings in F24 when the rocket was in the vicinity of the auroral forms (*cf.* Sect. 5.6) may well be generated by this instability.

8.3. *Ion-wave instabilities – The two-stream instability*

A collisionless plasma with equal ion and electron temperatures and with no imposed magnetic field will be unstable if the mean velocity of the electrons relative to the ions is approximately greater than the electron thermal velocity ($> 0.926\ v_{th}$, *cf. e.g.* Bernstein & Kulsrud 1960). However, this is a requirement which will never be approached in the ionosphere. Farley (1963) and Buneman (1963) extended the theory to in-

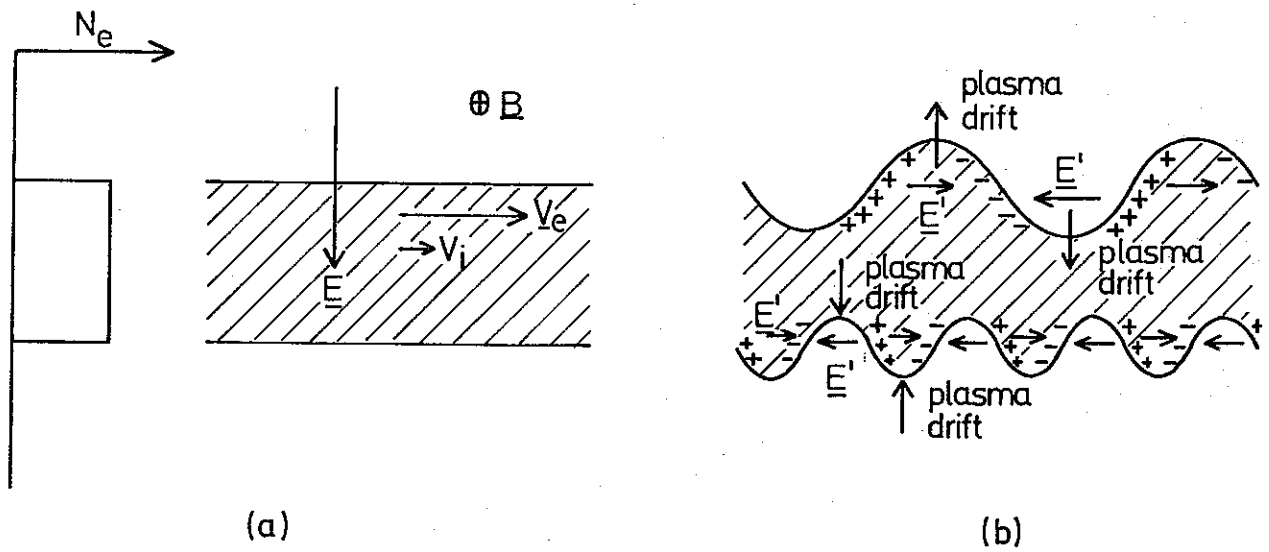

Fig. 8.1. Schematic representation of the $\mathbf{E} \times \mathbf{B}$ instability. The unperturbed situation (left) is a plasma slab with an electric field perpendicular to its boundaries and a magnetic field directed into the paper. A perturbation of the slab boundaries will produce a polarization field which will amplify the perturbation on the side of the slab where **E** points in the direction of increasing density.

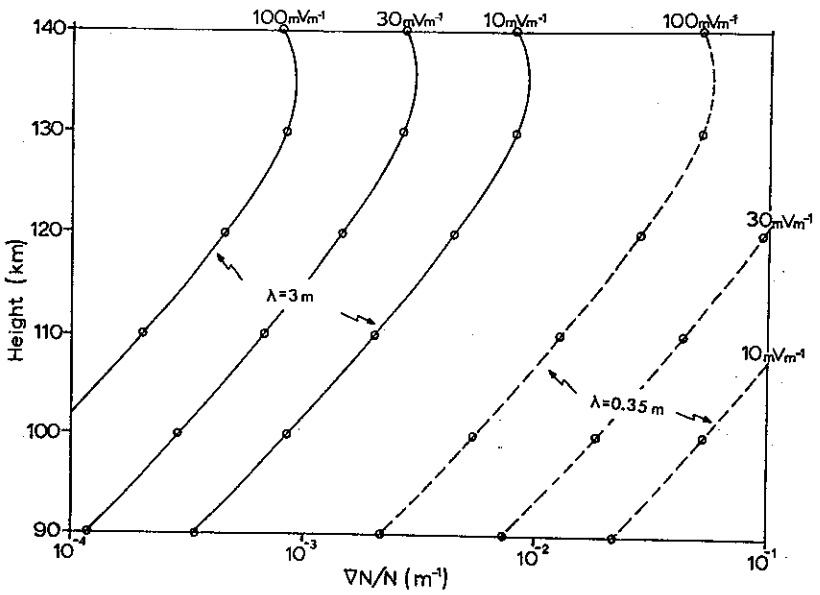

Fig. 8.2. Critical combination of electron density gradients and electric field as function of altitude for onset of $\mathbf{E}\times\mathbf{B}$ instability for $\lambda = 3$ m and $\lambda = 0.35$ m (after Unwin & Knox 1971).

clude collisions and magnetic field. In this case an instability will arise if the difference between the electron and ion drift velocities exceeds the *ion* thermal velocity, a condition which can be fulfilled in regions with high transverse conductivities. It was later shown by Kato & Hirata (1966) that among the six possible modes of electrostatic waves which could possibly be generated in a partly ionized plasma, without ionization gradients, influenced by crossed electric and magnetic field, this 'two-stream mode' was the only growing one.

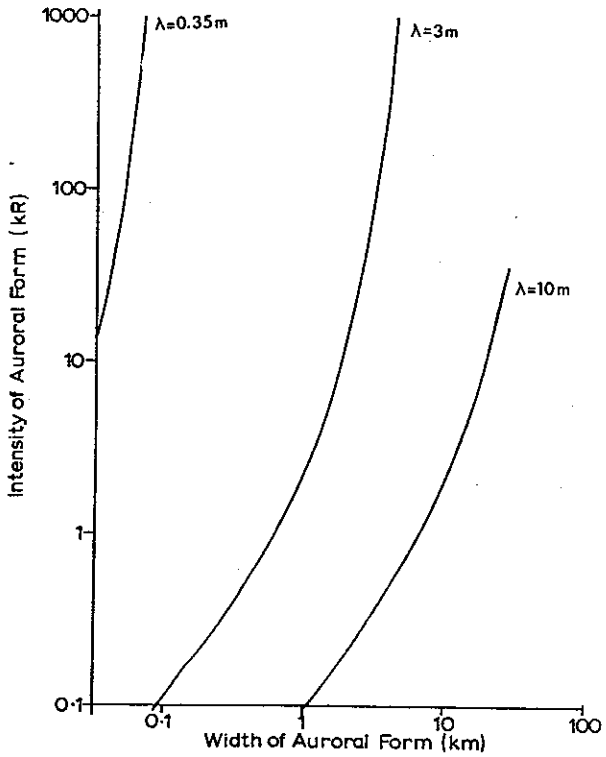

Fig. 8.3. Combinations of width and intensity of auroral forms giving the necessary density gradient for onset of $\mathbf{E}\times\mathbf{B}$ instability at a height of 105 km. The electric field is supposed to be 30 mV m^{-1} perpendicular to the earth's magnetic field (after Unwin & Knox 1971).

It may be difficult to acquire an understanding of the physical processes of the instability through the rather elaborate mathematics in these works. The instability can, however, be compared with a travelling-wave-tube amplifier (*cf. e.g.* Ettenberg 1963). Here an interaction between a plasma stream and a wave causes a growth of the wave if the particle velocity and the phase velocity of the wave are approximately the same. Thus, an *electron* beam may well give rise to an *ion* wave if the velocities are matching.

8.3.1. *The dispersion equation.* In the following the conditions for generation of ion waves by the two-stream instability will be derived, following the kinetic approach used by Farley. Some assumptions concerning the wave is necessary. All first-order quantities are supposed to vary as $\exp[i(\omega t - \mathbf{k}\cdot\mathbf{r})]$, where $\mathbf{k}$ is real but ω may be complex. A Cartesian coordinate system, with axes 1, 2, and 3 is chosen so that $\mathbf{k} = (0,0,k)$. The wave is electrostatic, which means that $\mathbf{E} = -i\mathbf{k}\varphi = -\nabla\varphi$ (Stix, 1962), and thus $\mathbf{E} = (0,0,E)$, if the wave is purely longitudinal.

In the derivation of the dispersion equation for the wave we will start with the generalized Ohm's law (*cf.* Eq. (4.2))

$$\mathbf{j} = \underset{\sim}{\sigma} \cdot \mathbf{E} \,. \tag{8·1}$$

The parameters involved here will, however, contrary to what was the case in Sect. 4.2, represent the AC properties of the medium. The current and charge densities, $\mathbf{j}$ and ϱ, must behave according to the continuity equation and Poisson's equation, *i.e.*

$$\nabla \cdot \mathbf{j} + \dot{\varrho} = 0 \,, \tag{8·2}$$

$$\nabla \cdot \mathbf{E} = \frac{1}{\varepsilon_o} \varrho \,. \tag{8.3}$$

Elimination of $\mathbf{j}$ and ϱ gives

$$\nabla \cdot (\underset{\sim}{\sigma} \cdot \mathbf{E}) + \varepsilon_o \nabla \cdot \dot{\mathbf{E}} = 0 \,. \tag{8.4}$$

With the coordinate system and assumptions introduced above, Eq. (8.4) becomes

$$\sigma_{33} E + i\omega\varepsilon_o E = 0 \,. \tag{8.5}$$

Excluding the trivial result $E = 0$, we have

$$\sigma_{33} + i\omega\varepsilon_o = 0 \,. \tag{8.6}$$

The problem of finding the dispersion equation will thus actually be that of finding the longitudinal component of the conductivity tensor. The basis for this derivation is the Boltzmann equation

$$\frac{\partial F_k}{\partial t} + \mathbf{v} \cdot \nabla F_k + \frac{q_k}{m_k} (\mathbf{E} + \mathbf{v} \times \mathbf{B}) \cdot \nabla_v F_k = \left(\frac{\partial F_k}{\partial t} \right)_v . \tag{8.7}$$

$F_k = F_k(\mathbf{r}, \mathbf{v}, t)$ is the distribution function for the k-particles in coordinate-velocity space; ∇F_k and $\nabla_v F_k$ denotes the gradient of F_k in coordinate and velocity space, respectively. (In the following the subscribt k will be omitted.) In linearization of this equation we will write $F(\mathbf{r}, \mathbf{v}, t) = F^{(0)} + F^{(1)}(\mathbf{r}, \mathbf{v}, t)$ and $B = B^{(0)} + B^{(1)}$. Considering only first-order quantities, the Boltzmann equation becomes

$$i(\omega - \mathbf{k} \cdot \mathbf{v}) F^{(1)} + \frac{q}{m} \mathbf{E} \cdot \nabla_v F^{(0)} + \frac{q}{m} (\mathbf{v} \times \mathbf{B}^{(0)}) \cdot \nabla_v F^{(1)} = \left(\frac{\partial F}{\partial t} \right)_v , \tag{8.8}$$

since $(\mathbf{v} \times \mathbf{B}) \cdot \nabla_v F^{(0)} = 0$ when $F^{(0)}$ is isotropic.

To proceed further one has to choose an approximate expression for the collision term. One main difficulty is that the relaxation term should affect only the velocity distribution of the particles and not their distribution in space, so that the particle concentration should be retained, not only on the average but also locally. Bhatnagar *et al.* (1954) introduced the following approximation (*cf.* also Dougherty 1963)

$$\left(\frac{\partial F}{\partial t} \right)_v = -\nu \left[F^{(1)} - \frac{N^{(1)}(\mathbf{r}, t)}{N^{(0)}} F^{(0)} \right] , \tag{8.9}$$

where ν is the effective collision frequency (*cf.* Sect. 3.5). $N^{(0)}$ and $N^{(1)}$ are the number densities corresponding to $F^{(0)}$ and $F^{(1)}$, and are defined by

$$N(\mathbf{r}, t) = \int_{\mathbf{v}} F(\mathbf{r}, \mathbf{v}, t) \, d^3v \,, \tag{8.10}$$

Using this expression for the relaxation term, Eq. (8.8) is transformed to

$$i(\omega - i\nu - \mathbf{k} \cdot \mathbf{v}) F^{(1)} + \frac{q}{m} (\mathbf{v} \times \mathbf{B}_o) \cdot \nabla_v F^{(1)} = \frac{q}{m} \mathbf{E} \cdot \nabla_v F^{(0)} + \nu \frac{N^{(1)}}{N^{(0)}} F^{(0)} \,. \tag{8.11}$$

The plan for the further analysis, after finding $F^{(1)}$, will be to obtain an expression for the corresponding current density, $\mathbf{j} = q \int \mathbf{v} F^{(1)} \, d^3v$, and finally use this in Eq. (8.1) to derive the components of the conductivity tensor. This procedure has been performed by Dougherty (1963) for the case that $F^{(0)}$ is Maxwellian. We will make use of his results, but regard the unperturbed distribution to be displaced with a mean drift velocity, $\mathbf{v}_d$, so that

$$F^{(0)}(v) = \left(\frac{m}{2\pi\kappa T} \right)^{3/2} N^{(0)} \exp \left[- \frac{m|\mathbf{v} - \mathbf{v}_d|^2}{2\kappa T} \right] . \tag{8.12}$$

In the equations previously derived in this section, ω should be replaced by $\omega' = \omega - \mathbf{k} \cdot \mathbf{v}_d$, *i.e.* we calculate the properties in a frame of reference moving with the velocity $\mathbf{v}_d$, and observe the corresponding Doppler-shifted frequency. Including

this modification in Dougherty's result, the longitudinal term of the AC conductivity tensor becomes

$$\sigma_{33} = \frac{\omega' N^{(0)} e^2}{\kappa T k^2} \mathrm{Y}(\omega^\dagger - v_d^\dagger, \nu^\dagger, \omega_c^\dagger, \alpha) \qquad (8.13)$$

for either electrons or singly charged ions. α is the angle between $\mathbf{k}$ and $\mathbf{B}^{(0)}$. The quantities $\omega^\dagger$, $\omega_c^\dagger$, $\nu^\dagger$ and $v_d^\dagger$ are the normalized oscillation frequency, gyrofrequency, collision frequency, and drift velocity, respectively. These are defined by

$$\omega^\dagger = \frac{\omega}{k}\left(\frac{m}{2\kappa T}\right)^{1/2}\left[\frac{\text{phase velocity}}{\text{thermal velocity}}\right], \qquad (8.14.a)$$

$$\omega_c^\dagger = \frac{\omega_c}{k}\left(\frac{m}{2\kappa T}\right)^{1/2}\left[\frac{\text{wavelength}}{\text{gyroradius}}\right], \qquad (8.14.b)$$

$$\nu^\dagger = \frac{\nu}{k}\left(\frac{m}{2\kappa T}\right)^{1/2}\left[\frac{\text{wavelength}}{\text{mean free path}}\right], \qquad (8.14.c)$$

$$v_d^\dagger = \frac{\mathbf{k}\cdot\mathbf{v}_d}{k}\left(\frac{m}{2\kappa T}\right)^{1/2} = v_d \cos\beta \left(\frac{m}{2\kappa T}\right)^{1/2}\left[\frac{\text{drift velocity}}{\text{thermal velocity}}\right], \qquad (8.14.d)$$

β is the angle between $\mathbf{k}$ and $\mathbf{v}_d$. The expressions apply to both electrons and ions, with proper use of parameters. 'The most probable velocity' in the distribution, $(m/2\kappa T)^{-1/2}$, has been taken as representative velocity.

The function Y, the normalized longitudinal conductivity, is defined by

$$\mathrm{Y} = \frac{(\omega^\dagger - v_d^\dagger - i\nu^\dagger)G + i}{1 - \nu^\dagger G}, \qquad (8.15)$$

where G is the Gordeyev integral of the complex argument $(\omega^\dagger - v_d^\dagger - i\nu^\dagger)$ (*cf. e.g.* Bernstein 1958)

$$G = \int_0^\infty \exp\left[-i(\omega^\dagger - v_d^\dagger - i\nu^\dagger)t - \omega_c^{\dagger -2} \sin^2\alpha \sin^2(\omega_c^\dagger t/2) - (t^2/4)\cos^2\alpha\right] dt . \qquad (8.16)$$

Considering a partly ionized plasma, consisting of drifting electrons and one species of singly charged ions, at rest with respect to the neutral particles, the total conductivity will be a sum of the electron and ion contributions. From Eq. (8.6) the dispersion equation becomes

$$\sigma_{33}^e + \sigma_{33}^i + i\omega'\varepsilon_o = 0 , \qquad (8{\cdot}17)$$

or, with insertion for σ_{33}^k from Eq. (8.13)

$$\mathrm{Y}_e(\omega_e^\dagger - v_{de}^\dagger, v_e^\dagger, \omega_{ce}^\dagger, \alpha) + \frac{T_e}{T_i}\mathrm{Y}_i(\omega_i^\dagger, \nu_i^\dagger, \omega_{ci}^\dagger, \alpha) + i\lambda_{De}^2 k^2 = 0 . \qquad (8.18)$$

λ_{De} is the Debye length (*cf.* Sect. 3.5). For a plasma with more than one kind of ions a weighted sum should replace the second term.

In general Eq. (8.18) is difficult to solve, as no simple closed analytic expression exists for the Gordeyev integral. One must therefore resort to approximate methods. The following inequalities are valid (*cf.* Chapter 3) in the part of the ionosphere of interest in this connection (*i.e.* 90–120 km): $\lambda_{De}^2 k^2 \ll 1$, $\omega_{ci}^\dagger < \nu_i^\dagger$, $\omega_{ce}^\dagger > \nu_e^\dagger$, and $\omega_{ce}^\dagger > 1$.

In the case $\omega_c^\dagger \ll \nu^\dagger$ (collision dominated motion) the following approximation can be made for Eq. (8.16)

$$G_i = \int_0^\infty \exp[-i(\omega_i^\dagger - \nu_i^\dagger)t - t^2/4]\, dt = -i\, Z(-\omega_i^\dagger + \nu_i^\dagger) . \qquad (8.19)$$

Z is the plasma dispersion function, $Z(w) = 2i \exp[-w^2] \int_{-\infty}^{iw} \exp[-t^2]\, dt$, which has been investigated and tabulated by Fried & Conte (1961).

In this approximation the normalized conductivity for ions becomes

$$\mathrm{Y}_i = \frac{(-\omega_i^\dagger + i\nu_i^\dagger)\, Z(-\omega_i^\dagger + i\nu_i^\dagger) + 1}{\nu_i^\dagger\, Z(-\omega_i^\dagger + i\nu_i^\dagger) - i} \qquad (8.20)$$

Regarding electrons, where $\omega_{ce}^\dagger \gg (1 \text{ and } \nu_e^\dagger)$, a different approximation is possible. Bernstein (1958) showed that for any $\omega_c^\dagger$ one can apply the following expression for the second term of the integrand in Eq. (8.16)

$$\exp[-\omega_c^{\dagger -2} \sin^2\alpha \sin^2(\omega_c^\dagger t/2)] = \exp[-\delta] \sum_{-\infty}^{\infty} \mathrm{I}_n(\delta) \exp[in\omega_c^\dagger t] , \qquad (8.21)$$

where $\delta = \sin^2\alpha/2\omega_c^{\dagger 2}$ and I_n is the Bessel function of first kind, of imaginary argument. In the

case that $\delta \ll 1$ (*i.e.* $\omega_c^\dagger \gg 1$) a series expansion of the Bessel function can be applied (Watson 1948)

$$I_n(\delta) = \sum_{m=0}^{\infty} \left(\frac{\delta}{2}\right)^{n+2m} \frac{1}{m!\,(n+m)!}. \quad (8.22)$$

Using these results and neglecting higher order terms in δ, Eq. (8.16) can for electrons be reduced to

$$G_e = -i\left(\frac{1-\delta_e}{\cos\alpha}\right) Z\left(\frac{-\omega_e^\dagger + v_{de}^\dagger + iv_e}{\cos\alpha}\right). \quad (8.23)$$

The normalized conductivity can then be expressed as

$$Y_e = \left(\frac{(1-\delta_e)w'\ Z(w')+1}{(1-\delta_e)\,(v_e^\dagger/\cos\alpha)\,Z(w')-i}\right), \quad (8.24)$$

where $w' = (-\omega_e^\dagger + v_{de}^\dagger + iv_e^\dagger)/\cos\alpha$. For large w' the assymptotic expansion of Z can be used (Fried & Conte 1961)

$$Z(w') \approx -\frac{1}{w'}\left(1+\frac{1}{2w'^2}+\ldots\right). \quad (8.25)$$

If **k** is nearly perpendicular to **B** so that $\cos^2\alpha \ll \nu_e^{\dagger 2}/\omega_{ce}^{\dagger 2} = \nu_e^2/\omega_{ce}^2$ the higher order terms of $\frac{1}{w'}$ can be neglected. In this case Eq. (8.24) reduces to

$$Y_e \approx \frac{i\delta_e(\omega_e^\dagger - v_{de}^\dagger - iv_e^\dagger)}{(\omega_e^\dagger - v_{de}^\dagger - i\delta_e v_e^\dagger)}. \quad (8.26)$$

As the wave parameters and ionospheric properties in the region of interest make $\lambda_{De}^2 k^2 \ll 1$, this term can be neglected in Eq. (8.18). If in addition we assume $T_e = T_i$, the resulting dispersion equation has the form

$$Y_i[\omega_i^\dagger - iv_i^\dagger] + Y_e[(\omega_e^\dagger - v_{de}^\dagger - iv_e^\dagger)/\cos\alpha] = 0 \quad (8.27)$$

for $\cos\alpha \neq 0$. Y_i and Y_e are defined by Eqs. (8.20) and (8.24). When $\cos\alpha \approx 0$ Eqs. (8.20) and (8.26) give

$$Y_i[\omega_i^\dagger - iv_i^\dagger] + i\delta_e(\omega_e^\dagger - v_{de}^\dagger - iv_e^\dagger)/(\omega_e^\dagger - v_{de}^\dagger - i\delta_e\, v_e^\dagger) = 0. \quad (8.28)$$

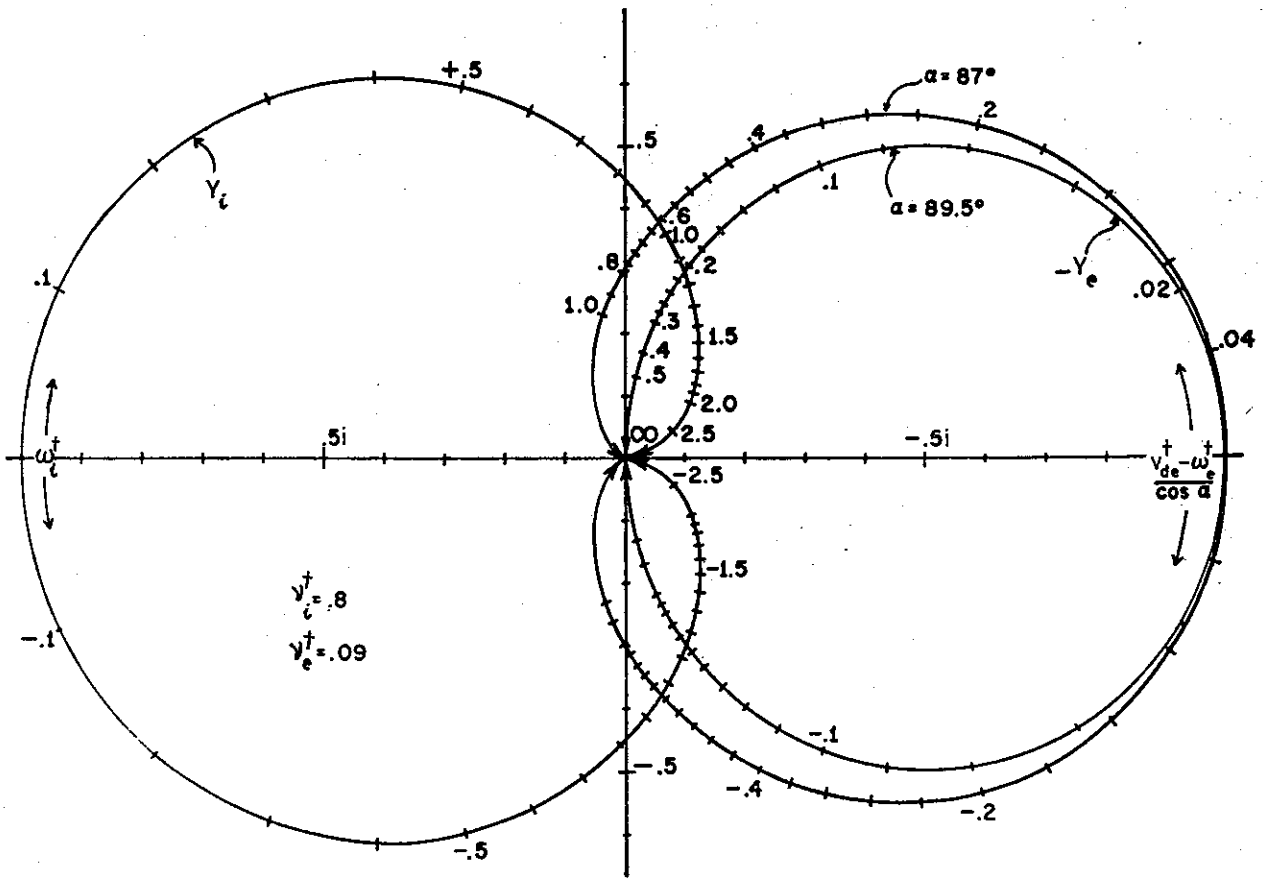

Fig. 8.4. Curves for normalized electron and ion conductivities, Y_e and Y. Intersection of the curves gives the critical conditions for a growing instability (after Farley 1963).

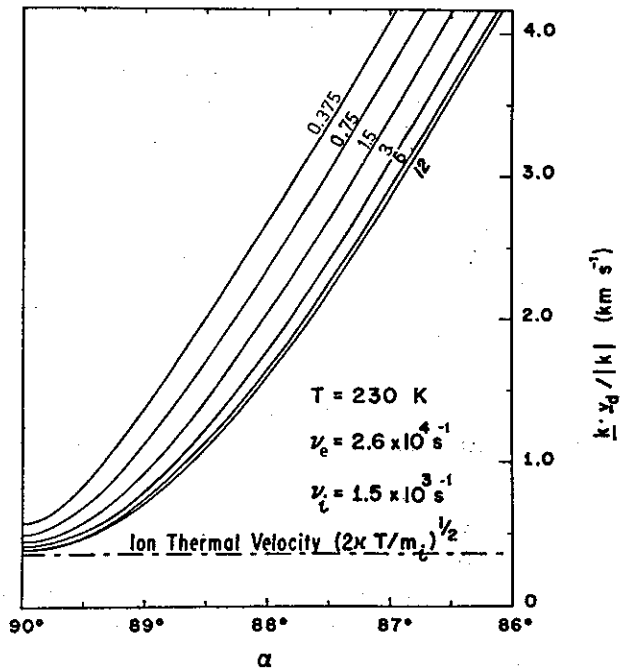

Fig. 8.5. Critical value of the component of the electron-ion drift velocity in the direction of the wave required to excite waves with various wavelengths (given by the numbers on the curves) as function of direction of propagation relative to the magnetic field (after Farley 1963).

Equations (8.27) and (8.28) thus give the conditions for critical stability, *i.e.* ω is purely real. Drift velocities greater than the critical value will give a negative imaginary part of ω, and a growing wave.

8.3.2. *Numerical examples.* The previous section gave the conditions for onset of the instability, but it remains to be seen if it will work in the ionospheric plasma, and generate waves within the desired frequency range. To sound this out, we will in an example use ionospheric parameters representing moderately disturbed *E*-region conditions and see if the required drift velocity can be obtained with a realistic value of the DC electric field. The calculations will be made for wavelength 1 m (*i.e.* $k = 2\pi$). The mean ion mass is assumed to be 30 u (NO^+), and the other parameters are: $T_e = T_i = 230$ K (thermal velocity for electrons 83.5 km s^{-1} and ions 356 m s^{-1}); $\nu_e = 2.6 \cdot 10^4$ s^{-1} ($\nu_e^\dagger = 0.05$), $\nu_i = 1.5 \cdot 10^3$ s^1 ($\nu_i^\dagger = 0.7$); $B = 5.10^{-5}\ T$ ($\omega_{ce} = 8.8$ MHz, $\omega_{ci} = 160$ Hz); $N_e = 10^{11}$ m^{-3}. One finds that the condition for critical stability for $\alpha = 90°$ and $\beta = 0°$ is $v_d = 465$ m s^{-1}. The corresponding phase velocity will be 415 m s^{-1} and the wave frequency 415 Hz. Regarding only the contribution from the Hall conductivity $\left(\frac{\sigma_H}{\sigma_P} \gg 1 \text{ with the present parameters } (cf.\ \text{Sect. } 4.2)\right)$ the electric field required to give the difference wanted between the electron and ion drift velocities is found to be 26 mV m^{-1}. This is a value often obtained at auroral latitudes (*cf.* Sect. 5.4), and one can from this example conclude that the *E*-region ionosphere is able to satisfy the conditions for growing instability.

To get more information about how the critical conditions and the first-order growth of the instability depend on the wavelength and direction of propagation, we will reproduce some of Farley's 1963 calculations. Figure 8.4 shows the variation of the normalized conductivities, Y_i and Y_e, for real values of the arguments $\omega_i^\dagger$ and

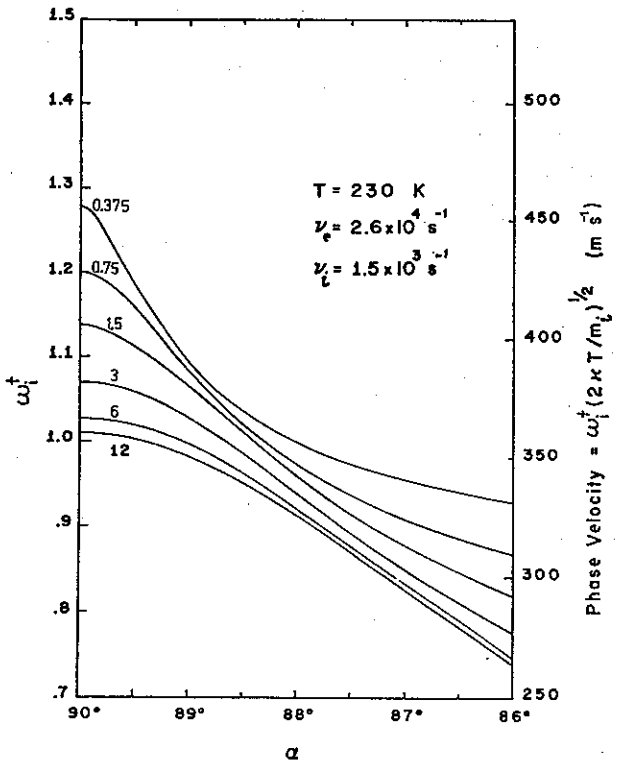

Fig. 8.6. Phase velocity of longitudinal waves generated at the critical growth condition. The numbers on the curves give the wavelength in metres (after Farley 1963).

$v_{de}^{\dagger}-\omega_e^{\dagger}$, and for a set of $v_i^{\dagger}$, $v_e^{\dagger}$, and α given on the figure. The intersection of the curves gives the conditions for critical stability, and the values of $\omega_e^{\dagger}$ and $v_{de}^{\dagger}-\omega_e^{\dagger}$ in this point determine the wave frequency and the critical drift velocity needed for growth of the wave.

Figure 8.5 gives the critical electron drift velocities for excitation of waves with various angles of propagation and for different wavelengths. It can be seen that waves propagating nearly perpendicular to the magnetic field can be generated if the electron drift velocity is slightly greater than the *ion* thermal velocity. The critical velocity increases only slowly with decreasing wavelength (or increasing frequency), but it increases rapidly as the propagation departs from orthogonality. Thus, waves with phase fronts parallel to the magnetic field lines are first excited.

Figure 8.6 shows a plot of the phase velocities of waves excited under the conditions given in Fig. 8.5. The waves, propagating perpendicular to the magnetic field, have a velocity somewhat greater than the ion thermal velocity, and the velocity decreases slowly as α deviates from 90°. The phase velocity increases with decreasing wavelength, but the dispersion is not great.

From these figures it is seen that drift velocities between approximately 400 and 580 m s^{-1} will generate waves perpendicular to **B** with frequencies ranging from 30 to 1200 Hz.

The growth rate of the instability will depend on the wavelength as well as the drift velocity. Figure 8.7 shows the growth rate of perpendicular waves as function of wavelength and drift velocity. The parameter τ is the time required for the wave amplitude to increase by a factor e (also called the e-folding time). The curve $\tau = \infty$ represents the critical growth conditions given in Figs. 8.5 and 8.6. The growth rate for a certain $v_d^{\dagger}$ will change with wavelength and reach a maximum before it decreases as one approaches $v_d^{\dagger}(\tau=\infty)$. The change in growth rate with drift velocity is most marked for the long wavelengths as the e-folding times here will be on the same order as the reciprocal of the oscillation frequency. The reciprocal of the e-folding time, the growth factor, gives information about the gain of the instability.

8.3.3. *Non-linear treatment.* In the linearization of the equations (Sect. 8.3.1) it is assumed that the perturbations in the fields and distribution function are sufficiently small, so that terms which are quadratic in these quantities can be neglected. Physically, this corresponds to neglecting coupling among the waves and the effect of wave-particle interaction on the distributions. This can be done at the onset of the wave growth and for a short time thereafter. The linear theory is therefore suited for deciding when a wave will go unstable. However, to determine the course of the wave growth, amplitude, energy spectrum, and phase velocities, it will be necessary to include non-linear effects.

Dougherty & Farley (1967) made a qualitative study of modifications of the irregularity spectrum caused by coupling between the primary waves. Consider a set of plasma waves with perturbations proportional to $\exp[i(\omega_j t-\mathbf{k}_j\cdot\mathbf{r})]$. For simplicity j is only supposed to take the values 1 and 2. Non-linear interaction involving products of the primary exponential terms will give rise to new Fourier components where $\mathbf{k}_j = s_1\mathbf{k}_1+s_2\mathbf{k}_2$ and $\omega_j = s_1\omega_1+s_2\omega_2$ $(j>2)$; $s_j = \pm 1$.

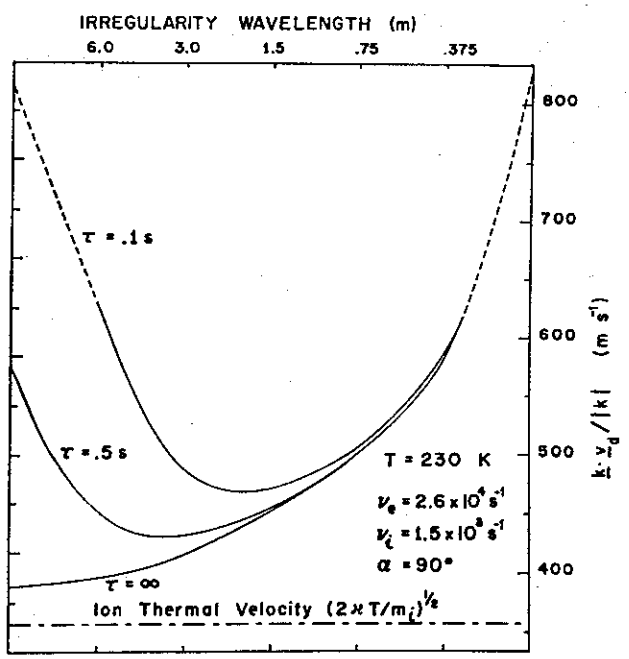

Fig. 8.7. The electron-ion drift velocity required to excite waves with various growth rates, τ, given as function of wavelength. $\tau = \infty$ represents the critical condition for onset of the instability (after Farley 1963).

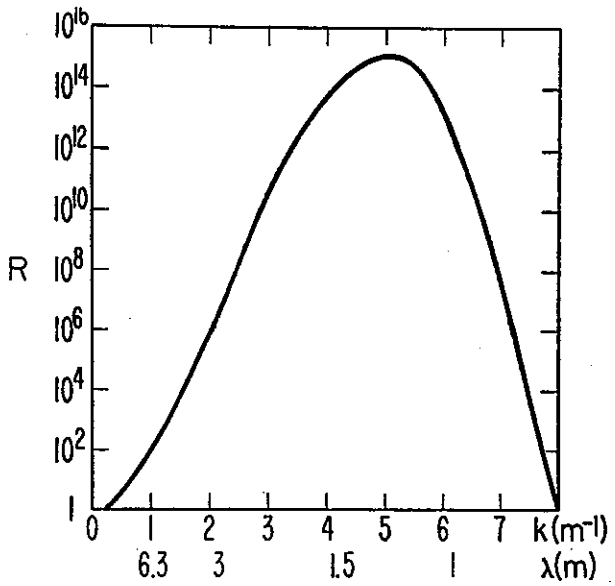

Fig. 8.8. Spectrum of irregularities generated by two-stream instability as calculated by Skadron & Weinstock (1969). The values on the ordinate give the ratio of turbulent electric field spectrum to incoherent backgroud spectrum. The spectrum is calculated letting the instability grow with its various growth rates for a time representing the stabilization time. The curve applies to a 500 m s^{-1} electron-ion drift velocity.

The effect of this interaction will be dual. It will limit the growth of the primary wave in transferring energy to secondary waves, which have properties – wavelength, velocity, direction of propagation – different from those found in the original components.

More rigorous theoretical treatments of the problem have been performed by *e.g.* Skadron & Weinstock (1969) and by Rogister (1971). Skadron and Weinstock also estimated an asymptotic wave spectrum (*cf.* Fig. 8.8), assuming all modes to grow in amplitude according to their linear growth rates for a time equal to the calculated stabilization time. The degree of perturbation reached in their calculations (rms fluctuation ≈ 0.6) seems, however, to be too high. Furthermore, the calculated phase velocities are in disagreement with velocity values deduced from the Doppler shift in radio aurora.

Rogister (*loc. cit.*) arrived at a more realistic value of the density fluctuations (≈ 0.05), but also in his calculations there is a divergence between the predicted and observed behaviour of the phase velocity.

8.3.4. *Discussion.* At present there appears to be no satisfactory non-linear treatment of the two-stream instability which shows quantitative agreement with the observations of *E*-region irregularities. On the other hand, these measurements are hardly sufficiently accurate, for instance concerning amplitude of the irregularities, to allow an adequate exchange of correcting features with the theoretical works. However, to answer the questions *if* and *where* waves will be set up by the instability, and also to give an idea of the range of wavelengths, the linear theory is found to be appropriate.

The main parameter in the two-stream theory is the electron drift velocity relative to the ions. The magnitude of this property will determine the frequency and the propagation angles of the waves and the gain in the generation mechanism (*cf.* Sect. 8.3.2.). The region of generation will thus be limited to the height interval where the mobility of the electrons differs significantly from that of the ions. Consequently, the instability will operate in the region where the motion of the electrons will be dominated by the magnetic field $\left(\frac{\omega_{ce}}{\nu_e} \gg 1\right)$, while the ion motion is collision dominated $\left(\frac{\omega_{ci}}{\nu_i} \ll 1\right)$ (*cf.* Sect. 4.2, Eqs. (4.11) and (4.13)). This means that the instability region will be located in the *E*-region (*cf.* Sect. 3.5), *i.e.* the height for the ELF noise and the ion waves coincides.

As the driving force of the directed charged particle motion is the DC electric field, this quality will be important when considering the possibility for instability. The process requires a minimum drift velocity for growth. A corresponding condition will then be put on the electric field, so that to generate waves at a certain frequency a minimum field strength is required. Taking an electric field of 30 mV m^{-1}, which is fairly typical for our two main events, this will give electron-ion drift velocities around 100 km of about 580 m s^{-1} for densities, temperatures, and collision frequencies (calculated after the equations in Sect. 4.2) representing the moderately strong auroral events (*cf.* Chapter 3). From Figs. 8.5 and 8.6 we will find that this will give rise to primary waves below approximately 1200 Hz. The two-stream

instability can thus generate waves within the actual frequency region during the existing conditions.

The theory for the two-stream instability showed a strong restriction on the geometrical configuration between **B**, **k**, and $\mathbf{v}_d$, so that the most easily generated wave has **k** parallel to the component of $\mathbf{v}_d$, which is perpendicular to **B** ($\alpha = 90°$). The electric field of a longitudinal wave will thus be approximately in the direction of the ionospheric current. As the auroral electrojet runs magnetically east-west, one will expect a maximum of the wave's electric field in this direction. This is what is observed in the ELF *E*-layer noise.

It can thus be seen that the main features – frequency range, altitude range, and direction of the field – in the *E*-layer noise agree with those predicted from a linear theory for a two-stream plasma instability where effects from collisions and magnetic field are included. We will therefore claim that the observed ELF *E*-layer noise is due to direct measurements of the fields generated by this process. In the next chapter we will return to the observations and give a detailed discussion of these, with the two-stream instability theory as a background.

9. DISCUSSIONS AND CONCLUSIONS

The two-stream plasma instability has turned out to be a profitable conception in the discussion of small-scale ionospheric irregularities associated with coherent scattering of radio waves (*cf.* Chapter 7). The present observation technique has, however, provided a new approach to the problems. New, first-hand information about spectral distribution, direction of the wavefield, and variations of the wave properties with altitude have been obtained from these in situ measurements. The direct result of this is an improved mapping of the small-scale electric fields in the *E*-region. To utilize fully our knowledge in a study where an interaction between theory and experiment can give a better understanding of the physical processes involved in the generation of the waves, it is, however, necessary to have detailed information about plasma parameters as temperatures, densities, collision frequencies, and local magnetic fields. This information is more or less missing in the present case. We will, therefore, in the following discussion restrict ourselves to the study of the two-stream instability wavefields as they appear from the simple linear theory, using an ionospheric model constructed from the available data. Comparison with the observed features will, however, give an answer to the question whether this instability can set up fields with the observed characteristics during the present conditions.

9.1. *An ionospheric model and the related two-stream instability*

The ionospheric model used in the following study represents the flight conditions of the rockets F23 and F24. The electron density profile, shown in Fig. 9.1, is a smoothed average of various density measurements (impedance probe, spherical electrostatic analyzer (Folkestad, priv. com.), and VLF Doppler) made on the downleg of the F23 flight. The collision frequencies and temperatures are taken from Sect. 3.5 for a moderately disturbed case. We will suppose $T_e \approx T_i$. This latter assumption will not be valid in the upper part of the height interval for the present conditions. However, the main effect of making $T_e > T_i$ is an

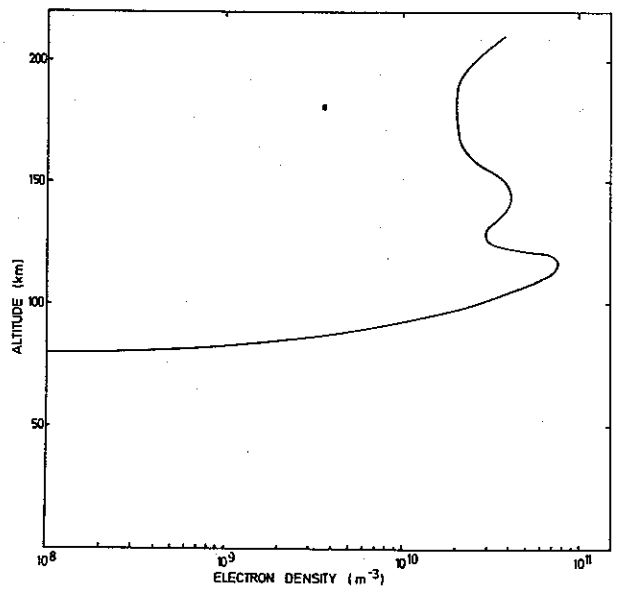

Fig. 9.1. Electron density profile representing a smoothed average of various measurements made from the rocket F23.

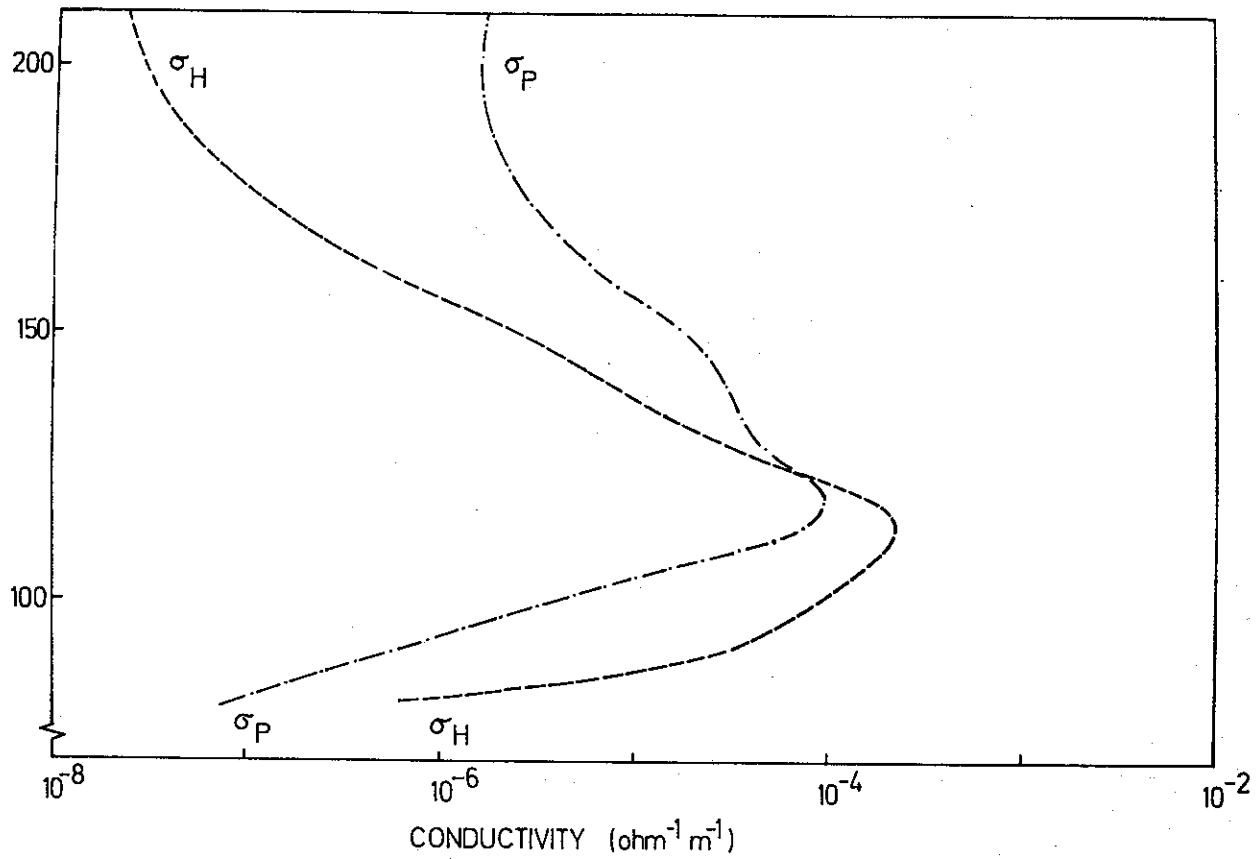

Fig. 9.2. Pedersen and Hall conductivities calculated from the electron density given in Fig. 9.1 and parameters representing moderately disturbed conditions (Fig. 3.8, Eqs. (3.6), (3.7), (3.8) and (4.9)).

increase in the critical drift velocity, so that the highest altitude for generation of waves will be shifted slightly downwards from that found in the model. A mean ion mass number of 30 is used. The DC electric field is 35 mV m^{-1} and directed southward (*cf.* Figs. 5.13 and 5.17). The earth's magnetic field is determined using the coefficients from Cain & Cain (1968). Conductivity profiles for this model, calculated from Eqs. (4.9.a) and (4.9.b), are shown in Fig. 9.2. It can be seen that the Hall conductivity dominates over the Pedersen conductivity below approximately 125 km.

The Pedersen and Hall mobilities are defined as

$$\eta_P^{(k)} = \sigma_P^{(k)}/N_k\, q_k\,, \qquad (9.1.a)$$

$$\eta_H^{(k)} = \sigma_H^{(k)}/N_k\, q_k\,. \qquad (9.1.b)$$

$\sigma_P^{(k)}$ and $\sigma_H^{(k)}$ are the contributions of the k-particles to the Pedersen and Hall conductivities respectively. From $v = \eta E$ one finds the velocity components of the electrons and ions and consequently the electron-ion drift velocity. This quantity is plotted in Fig. 9.3, curve (a). The direction of the velocity vector will, however, change as the ratio σ_H/σ_P varies (*cf.* Sect. 4.2). From Sect. 8.3 it is found that the present drift velocity will cause maximum growth rates for wavelengths between 3 to 1.5 m, corresponding to frequencies from about 150 to 300 Hz.

The calculated critical drift velocity, $v_d(\tau = \infty)$, for generation of perpendicular waves at $\lambda = 3$ m is plotted as function of altitude in Fig. 9.3, curve (*b*). A minimum in $v_d(\tau = \infty)$ is found between 102–105 km. This is due to the increase of T_k and decrease of ν_k with altitude.

From Fig. 9.3 it is seen that with the present ionospheric model and an electric field of 35 mV m^{-1}, the two-stream instability should generate waves with $\lambda = 3$m in the altitude range 95–123 km. Furthermore, since waves can be generated as long as $v_d \cos\beta \geq v_d(\tau = \infty)$ (*cf.* Fig. 9.4), it can be found that at the altitudes where

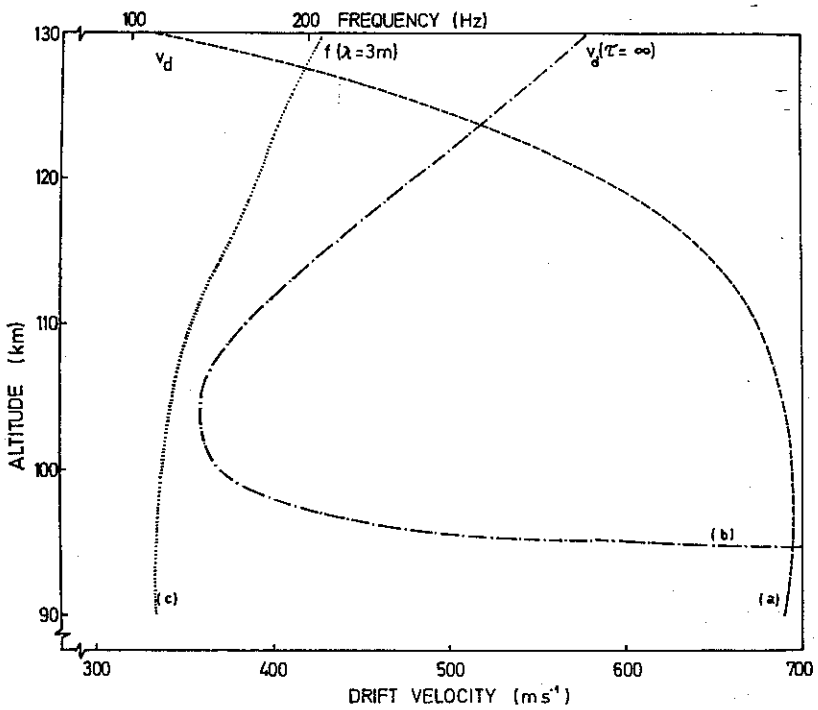

Fig. 9.3. The figure shows altitude plots of the following parameters calculated for the ionospheric model represented in Figs. 9.1 and 9.2, and a DC electric field of 35 mV m^{-1}. v_d: electron-ion drift velocity; $v_d(\tau = \infty)$: critical drift velocity for generation of a plasma instability with wavelength 3 m; $f(\lambda = 3$ m): frequency of a wave with 3 m wavelength.

$v_d - v_d(\tau = \infty)$ has its highest values, a spread in k over $\pm 55°$ can take place. However, as k departs from v_d the gain in the mechanism decreases. From the altitude of maximum β, the β-range will decrease towards the altitudes where $v_d(\tau = \infty) = v_d$. As the critical velocity will increase with decreasing wavelength, the fan of permitted propagation directions will be narrowed down towards shorter wavelengths. The electric field of the wave will thus be most spread out in the low frequency part of the spectrum.

The frequency of a wave with constant wavelength will vary with altitude as change in temperature causes variation of the phase velocity ($v_{ph} = \omega_i^{\dagger}(2\kappa T/m_i)^{1/2}$). The frequency of the wave generated at the critical velocity shown in curve (b) of Fig. 9.3 has been plotted in curve (c). One can see that for constant wavelength the frequency will increase with increasing altitude, and that $\Delta f/\Delta h$ will be greatest in the upper part of the generation region. For these altitudes there will thus be a double effect modifying the appearance of the spectrum. The first effect is that the critical velocity will increase, which reduces the generation of short wavelengths. The other effect, the increase in frequency for a fixed wavelength, goes in the other direction and tends to shift the spectrum towards higher frequencies.

The high altitude part of the observations seems to behave in accordance with this (*cf.* Figs. 2.8 and 2.9). The change in the high frequency cut-off is most pronounced, as one should expect, since this acts on the very generation mechanism. However, at the same time a rise of the low frequency limit can also be observed (*cf.* Fig. 9.5).

Other features in the ELF *E*-layer noise are

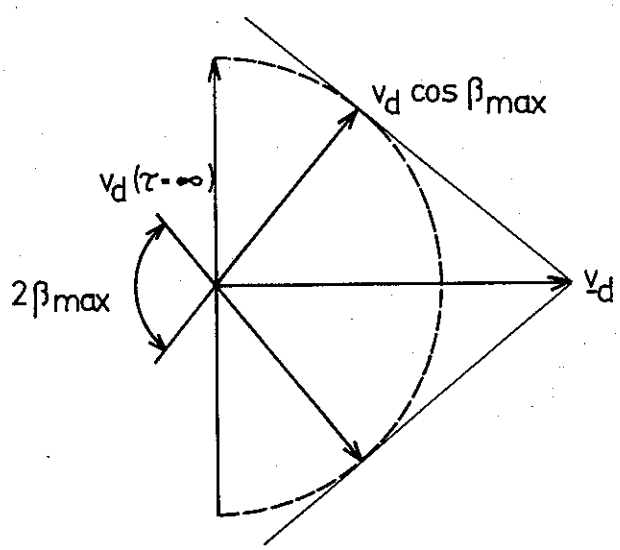

Fig. 9.4. Sketch showing possible deviations, β, between electron-ion drift velocity and direction of the wave for a given and $v_d(\tau = \infty)$. The magnetic field is directed into the paper ($\alpha = 90°$).

also found to agree well with the characteristics predicted from the two-stream instability model. The observed and calculated altitude ranges are almost identical. There is a minor disagreement concerning the high altitude boundary, but this could probably be improved in a model where $T_i \neq T_e$.

The observed frequency range corresponds fairly well to that found theoretically. However, a discrepancy appears for the high frequency part of the spectrum; the model spectrum stops at approximately 1500 Hz, whereas the observations show waves up to about 3000 Hz. The waves above 1000 Hz are, however, weak, and only observed during the most intense part of the noise bursts. It may be possible to explain this part of the spectrum as a result of non-linear effects. Secondary waves, created by wave-wave interaction (*cf.* Sect. 8.3.3), will have frequencies which differ from those of the interacting waves. Coupling between strong two-stream waves can then give wavefields with spectral components different from that predicted by linear theory. The high frequency part of the spectrum will also be modified by Doppler shift in the observed frequency (*cf.* Sect. 9.2).

The observed spin modulation in the *E*-layer noise showed that this effect almost disappeared for frequencies below 150 Hz and that it was more pronounced for high altitudes, *i.e.* above say 107 km, than below this height. When regarding this effect one should also take the antenna pattern into account. Theoretically this can be described as (Kraus 1950)

$$A \propto \frac{\cos\left[(2kd\cos\theta)/2\right] - \cos\left(2kd/2\right)}{\sin\theta}. \quad (9.2)$$

d is the distance between the electrical midpoints of the elements and θ is the angle between direction of antenna and E. For an antenna where $2d = \lambda$ the opening angle of the pattern is $\sim 50°$, and $\sim 80°$ for $d = \lambda$. The pattern can, however, deviate significantly from the theoretical values, and also appear in rather complicated forms. The regularity in the spin modulation indicates, however, a smooth variation with θ. Taking the width of the antenna diagram into account it is clear that the electric field of the wave has a well-defined direction in the high frequency part, but that it is more spread out at lower frequencies. This is also in accordance with what was found from the model where variation in β increased with decreasing

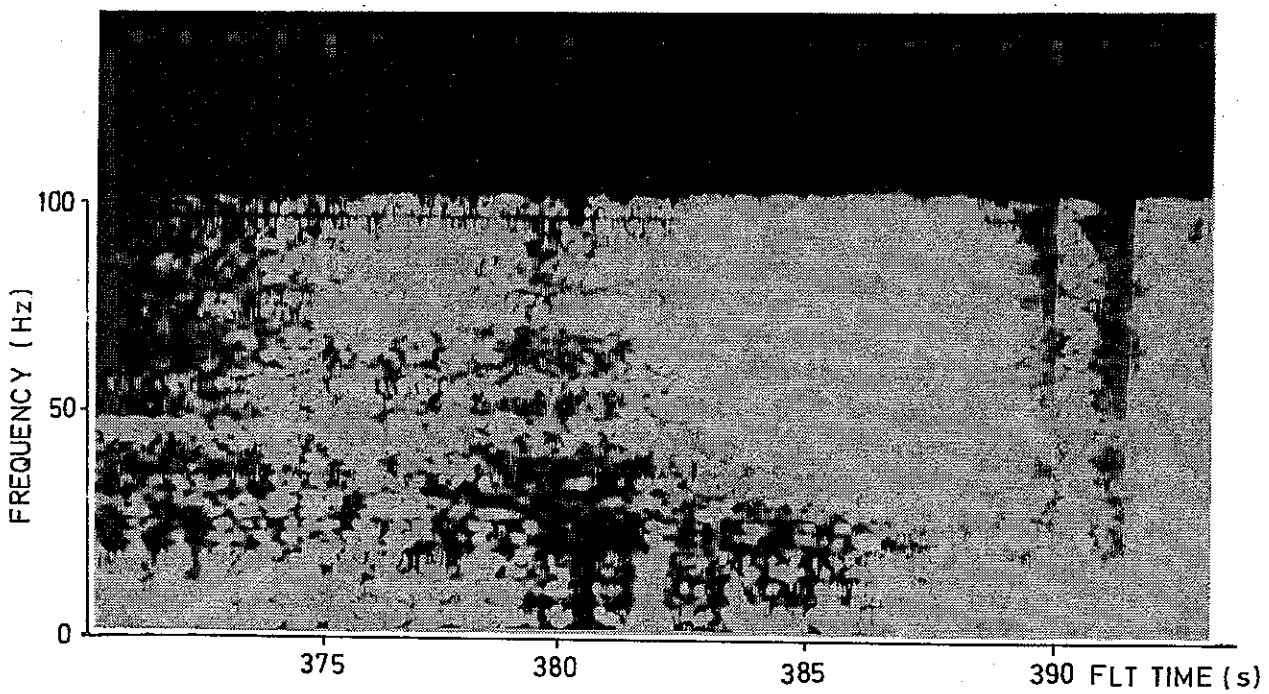

Fig. 9.5. Spectrogram of ELF *E*-layer noise as recorded by the DC *E*-field channel in F24 showing the variation in the low frequency cut-off of the emission.

frequency. The deviation in **k** together with the width of the antenna pattern will then smear out the spin variation at low frequencies. This effect should be greatest where $v_d - v_d(\tau = \infty)$ is great. This is what is mainly observed. The total lack of spin modulation during the last couple of km before the low altitude cut off can, however, hardly be explained by β-spreading of the primarily generated waves.

9.2. *Amplitude vs. frequency distribution of ELF E-layer noise*

Two effects will make the observed wave spectrum different from the real wavefield spectrum: Doppler shift due to the motion of the rocket, and the fact that the wavelengths of interest will range from where they are greater than the antenna length down to being only a fraction of this dimension.

A wave observed by a rocket borne receiver will be shifted in frequency by an amount given by the Doppler shift formula in Eq. (6.1). The form convenient to use in this connection is

$$\Delta f_D = -f_o \frac{v_R}{v_{ph}} \cos \sigma \,, \tag{9.3}$$

where the notations are the same as in Sect. 6.2, and where the spin term has been neglected. For an electromagnetic wave $v_{ph} \gg v_R$, so that the Doppler shift can normally be neglected in measurement of noise spectra. For electrostatic waves the relation between these two properties is, however, that $v_R \gtrsim v_{ph}$. Thus, the rocket motion can introduce a considerable displacement of the spectrum.

In the present case the geometrical configuration was as follows. The rocket trajectory plane had an azimuth $\chi_R \approx 320°$. The southward-directed electric field will give rise to an eastward drift of the electrons. Assuming that the velocity vector is in the same direction as the maximum electric field in the wave, the azimuth angle of **k** can then, *cf.* Fig. 2.12, be set $\chi_k \approx 70°$, so that $\sigma \approx 250°$, since only the horizontal component of the rocket velocity is important. As $\cos \sigma < 0$ we have $\Delta f_D > 0$ and the observed frequency is shifted to a value higher than the wave frequency. Using typical values for the velocities at 100 km, $v_R = 550$ m s^{-1} and $v_{ph} = 400$ m s^{-1}, the relative frequency shift will be approximately 47%. The Doppler shift will thus lift the low frequency cut-off. The true frequency of an observed value of 40 Hz will for instance be 21 Hz, and all together the whole spectrum is shifted downwards so that signals down to a few Hertz will be present in the true wavefield. The Doppler shift will also make the high frequency tail of the spectrum less extended than it appears in the observations.

As the wavelengths extend over a range which makes $\lambda_{min} < d < \lambda_{max}$, the antenna response will be different for different parts of the spectrum. Maximum sensitivity will appear when $d = \lambda/2$. Taking the attitude of the rocket with respect to **k** into account, this means maximum response around $\lambda \approx 11$ m, which corresponds to a frequency of about 35 Hz. Below this frequency the sensitivity will decrease slowly, as the antenna will not see the entire peak-to-peak value of the wavefield. This effect is, however, far too weak to explain the observed low frequency roll-off of the spectrum.

Above the frequency of maximum response the electric field of the wave will not be monotonously varying over the antenna elements, and one will have situations where a part of the field will be eliminated in the differential amplifier. In an ideal case the output signal may vary from the peak-to-peak value of the field down to zero, according to the position of the antenna with respect to the space-varying wavefield. One should therefore expect a highly fluctuating amplitude in the recordings, which was in fact observed (*cf.* Fig. 2.9), and that the amplitude, on average, will decrease with increasing frequency. The frequency response of the electronics in this part of the spectrum will, however, eliminate this effect, so that the observed decrease of amplitude with increasing frequency is supposed to be present also in the real field. We will thus claim that even though variations in the ratio λ/d will modify the observed spectrum to some extent, the observed amplitude *vs.* frequency distribution will in the main give a true picture of the distribution of the wavefield, when effects from Doppler shift are taken into account.

The high frequency part of the power spectrum has about the same appearance as that observed

by coherent scatter measurements. However, the slope of the curve in our measurements does not fall off quite as rapidly as in the radar spectra. Below the frequency of maximum amplitude there is total disagreement with the scatter measurements. One should, however, be aware that these measurements are subjected to great uncertainties at radar frequencies below 100 MHz, as *e.g.* refraction and critical reflections will influence the measurements at these frequencies.

The decreasing amplitudes at the low frequency part of the spectrum may be explained by decreased growth rate at these frequencies (Fig. 8.7). The appearance of the observed spectrum also corresponds reasonably well with that predicted from non-linear theory by Skadron & Weinstock (1969) (*cf.* Fig. 8.8).

9.3. *Direction variation of the wave electric field and corresponding changes in current distribution*

In the presentation of the data in Chapter 2 it became clear that the direction of the electric field vector varies with altitude. The strongest field should be generated when $\beta = 0$, and the direction of maximum amplitude in the wavefield will therefore give information about the direction of the electron-ion drift velocity. The *E*-layer noise can thus provide a means to directly trace the direction of the current. Furthermore, if vectorial measurements of the DC electric field are available, one can then learn about variations in the conductivities. The angle between the DC electric field and the current vector is found to be (*cf.* Sect. 4.2, Eq. (4.10)): $\arctan \frac{\omega_{ce}}{\nu_e} - \arctan \frac{\omega_{ci}}{\nu_i}$.

As $\frac{\omega_{ce}}{\nu_e} \gg 1$ above 90 km, direction variations are mainly caused by changes in ν_i. These measurements can then also give information about the collision frequencies of the ions.

In the F24 event the DC electric field was directed southwards, and stayed, within accuracy of the measurements, in the same direction in the *E*-region (*cf.* Fig. 5.13). The direction of the wavefield (Fig. 2.10) fits well with that expected for the current. With a dominating Hall conductivity this should run magnetic east-west. However, it can be seen that the direction of the wavefield is rotated more towards north-south in the upper part of the emission region (above 110 km). This shift is in accordance with the increasing importance of the Pedersen conductivity which will appear here.

In the F23 recordings a similar northward rotation with increasing altitude appears. However, the most conspicuous feature in the direction plot of the field is the sudden change which takes place at approximately 110 km. Over an altitude of a couple of km, a shift of about 30° occurs. Above and below this altitude the directions appear in two quite separate groups.

The configuration will thus not be a stratified structure, where the direction of the field goes back to its previous value after having crossed a layer, but rather a boundary surface at 110 km where a sudden shift in the direction of the current occurs. Even though the attitude information in the DC measurements are burdened with large uncertainties, it is clear that the DC field did not have a shift in direction corresponding to that seen in the *E*-layer noise field. It does not seem possible to explain these observations from the available information. The rocket magnetometers showed large fluctuations, giving evidence of local perturbations in the magnetic field. This may be associated with strong sheet currents which may influence temperatures and conductivities. The sporadic *E*-layer observed during the launch event (*cf.* Sect. 2.2) may also be suggested to be connected with the direction shift. The electron density profile (Fig. 9.1), however, did not show any drastic variation around 110 km.

In discussing the orientation of the amplitude maxima it has been assumed that the observed variations, both the spin pattern and the direction shift, are caused by spread in β and shifts of the direction of $\mathbf{v}_d$ in a plane perpendicular to the earth's magnetic field. Lurching of $\mathbf{k}$ out from perpendicularity has not been regarded, because, according to the two-stream instability theory, the present drift velocity will not give rise to primary waves where α deviates more than 1° from perpendicularity (*cf.* Fig. 8.5). In the case of local perturbations of the magnetic field, *e.g.* in connection with strong currents, it will be possible to get deviations from the direction predicted

from the model magnetic field. With single axis measurements it is, however, not possible to determine whether the shift is caused by $\mathbf{v}_d$ or **B** variations.

9.4. *Conclusions*

The features observed in the ELF *E*-layer noise and the properties of the wavefields predicted using the theory for a two-stream plasma instability, show a very good correspondence. It is therefore concluded that the observed fields are electrostatic waves generated by this mechanism. The presence of such waves in the auroral ionosphere has earlier been postulated from radio aurora measurements. With the present experiment direct observations of the wavefield, its frequency spectrum, altitude range, and direction, have been made.

Observation of *E*-layer noise will furthermore give information about the direction of the currents in the *E*-region, and thus provide information about variations in the Pedersen and Hall conductivities and the properties involved in these parameters.

Rocket measurements of *E*-layer noise should in the future be correlated with radar observations, this both to test the validity of the postulated relationship, and to obtain new experimental information which will add to the understanding of these phenomena.

The rocket experiments should be extended to include three-axis measurements of the field, and simultaneous measurements with antennas of different length. This would permit tracking not only of the β dependence of the wave, but also the variation of amplitude with α and local variations of the direction of the magneticfield. Furthermore, it would make it possible to determine the dispersion of the waves and to obtain absolute amplitude measurements. This would, in turn, enable us to compare experiments and theory, and to test and extend the validity of non-linear theories for generation of the waves.

Let us be satisfied with what we have discovered, and leave a little truth for our descendants to find out.

Seneca, Naturales quaestiones 7,26 (about A.D. 63).

APPENDIX I: VARIATIONS IN PROBE POTENTIAL CAUSED BY ENVIRONMENTAL EFFECTS

We will here return to the subject dealt with in Sect. 5.5 and consider factors which may cause variations in the probe potentials, and give contributions to the measured differential voltage not due to ambient electric fields.

AI.1. *Probe motion, velocity gradients, and their influence on the floating potential*

The motion of the probe through the plasma will modify the spatial density distribution of particles around the probe and change the currents flowing in the plasma sheath. Qualitatively, this can be described as an increase of the particle flux on the upwind side and a decrease on the downwind side. This will, however, not have appreciable influence unless the probe velocity is comparable with the mean particle velocity. Thus, only the ion current will be modified in ionospheric rocket measurements. As the particle flux on the upwind side will increase more than its decrease on the lee side, the net effect will be an increased ion current, driving the probe potential more positively than in the stationary case (*cf.* Eqs. (5.1.b) and (5.4)).

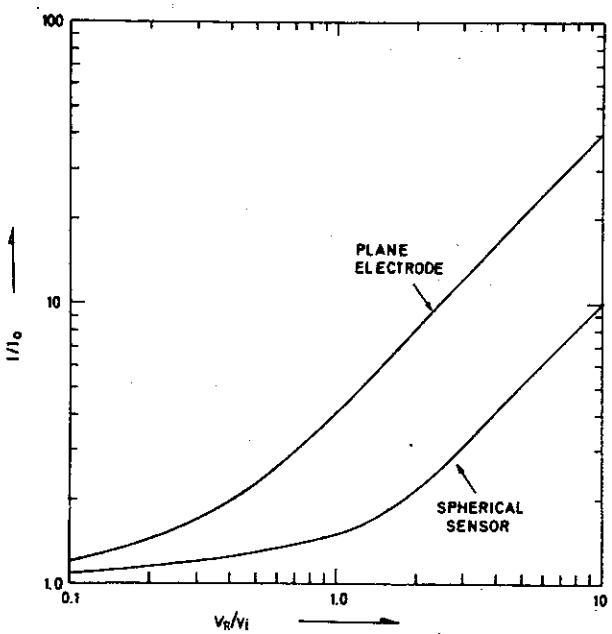

Fig. AI.1. Ion current, normalized to the value at zero probe velocity, as function of probe velocity to ion thermal velocity (after Folkestad 1970).

The curves in Fig. AI.1 show the current ratio $J_v/J_{v=o}$ as a function of probe velocity relative to particle thermal velocity ($v_R/\langle v_k\rangle$) for a spherical probe and a plane electrode (Folkestad 1970). The cylindrical probe values will be located somewhere between the two. It can be seen that for $(v_R/\langle v_k\rangle) > 1$–2 the normalized current is linearly related to the velocity, *i.e.* the particles can be regarded as stationary. In this case a good approximation for the current density (*cf.* Eq. 5.3) will be

$$j'_{ko} = \varepsilon_k \tfrac{1}{4} eN_k \left(\frac{8\kappa T_k}{\pi m_k} + v_R^2\right)^{1/2}. \qquad \text{(AI.1)}$$

An exact treatment of the problem is, however, complex as the ion trajectories are also influenced by the local electric fields. A few cases have been studied by Walker (1965), and it is apparent that the current may deviate considerably from what was said above. However, for rocket measurements in the ionosphere, where $v_R/\langle v_i\rangle \approx 1-2$ and the probe potentials are small, our estimate is accurate at least to the order of magnitude. Furthermore, as the effect of this linear velocity in an ideal case will be the same for both probes, it should not give rise to variations in the differential voltage.

Besides having a translational velocity, the probe will also rotate with an angular frequency ω_s. The two probes will thus in general have different velocities with respect to the plasma, introducing an error voltage. The maximum velocity difference will be $\omega_s d$, and the potential difference due to rotation is

$$\Delta\varphi_s \leq \omega_s d \frac{\partial \varphi_o}{\partial v_R}. \qquad \text{(AI.2)}$$

Differentiation of Eq. (5.5), where the expression in Eq. (AI.1) has been used for j_{io}, gives

$$\frac{\partial \varphi_o}{\partial v_R} = \frac{\kappa T_e}{e} \frac{\pi m_i v_R}{8\kappa T_i + \pi m_i v_R^2}, \qquad \text{(AI.3)}$$

when we suppose $j_{ph} = 0$.

Taking as numerical example $v_R = 10^3$ m s^{-1}, and $T_e = T_i = 250$ *K* this gives $\frac{\partial \varphi_o}{\partial v_R} \approx 1.8 \cdot 10^{-5}$ V s m^{-1}. With $d = 10$ m and $\omega = 2\pi$, $\Delta\varphi_s \approx 1.1$ mV, so that this may be a noticeable effect. A

similar sensitivity to velocity gradients in the plasma will also exist, and Eq. (AI.3) can also be applied in this connection.

AI.2. *Error analysis*

Section 5.5 listed various sources of error pertinent to electric field measurements with the double floating probe technique. We will here examine these effects in more detail, and estimate their importance in the observations.

i) The $\mathbf{v}\times\mathbf{B}$ term: For rocket measurements in the ionosphere, where $v_R \approx 10^3$ m s^{-1} and $B \approx 5\cdot 10^{-5}$ *T*, the electric field induced by the rocket motion will be on the order of some tens of mV m^{-1} or less, *i.e.* about the same as the ambient field. Our inability to distinguish between the rest frame field and the contribution due to the motion of the probes makes it very important to get information about the probe attitude and velocity with respect to the magnetic field. If we take as a design criterion the requirement that the $\mathbf{v}\times\mathbf{B}$ term should not give more than 10% error in the final value of *E*, it follows that the maximum relative error permitted in the measurements of $|\mathbf{v}\times\mathbf{B}|$ will be $\delta_{vB} \leq 10^{-1}\frac{E}{vB}$. This will not require any unrealistic measuring accuracy. In vectorial determination of *E*, similar restrictions will be put on the orientation of the vehicle and antennas in space. These requirements are difficult to fulfill, if one is limited to the use of magnetic aspect sensors, which are sensitive to variations in external conditions and are difficult to calibrate.

ii) Finite voltmeter current: The derivations in Sect. 5.5 were made under the assumption that no currents were drawn from the probes. As the voltmeters have a finite input resistance, *R*, currents will leak through the voltmeter and disturb the probe potential. This current increases the potential of the most negative probe and decreases that of the other. The voltmeter will thus read a value $E'd-2\Delta\varphi_j$, if symmetrical conditions are assumed. $\Delta\varphi_j$ is the change in potential for one probe due to the current.

Again supposing $\varphi < 0$ we will modify Eq. (5.10) to include a finite voltmeter current, *i.e.* $J \neq 0$ in Eq. (5.1.a). The probe length is $d' = d_2 - d_1 (= d - 2d_1)$. The probe potential is then expressed as

$$\varphi = -\frac{\kappa T_e}{e} \times \ln\left\{\frac{\kappa T_e}{e}\frac{2\pi j_{eo} a\left(\exp\left[\frac{e}{\kappa T}(\mathbf{E}+\mathbf{v}\times\mathbf{B})\cdot\mathbf{d}'\right]-1\right)}{(\mathbf{E}+\mathbf{v}\times\mathbf{B})\cdot\hat{\mathbf{d}}\left(\int j_i dS+\gamma\int j_{ph}dS+J\right)}\right\}. \quad \text{(AI.4)}$$

For small currents we will have $\Delta\varphi_j \approx \left|J\cdot\frac{\partial\varphi}{\partial J}\right|$, and

$$\Delta\varphi_j \approx -\frac{\kappa T_e}{e}\frac{J}{\int j_{io}dS+\gamma\int j_{pho}dS}. \quad \text{(AI.5)}$$

As $J = \frac{E'd}{R}$ this will define the minimum input resistance which can be permitted in order not to introduce noticeable errors in the determination of the field strength.

iii) Wake effects: A body which has a velocity relative to the ambient gas will be surrounded by a region where the density and velocity distribution of the particles differ from those in the bulk gas. A region of condensation, bounded by a shock-wave, is formed in front of the body. Since the body 'sweeps up' particles, preventing them from filling up the region behind, a region of rarefaction, a wake, is formed at the rear of the body.

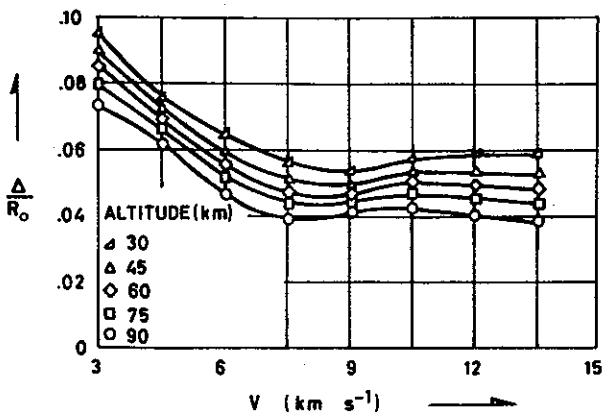

Fig. AI.2. Shock stand-off distances, Δ, of a spherical object with radius R_0, as function of altitude and velocity (after Lomax & Inonye 1964).

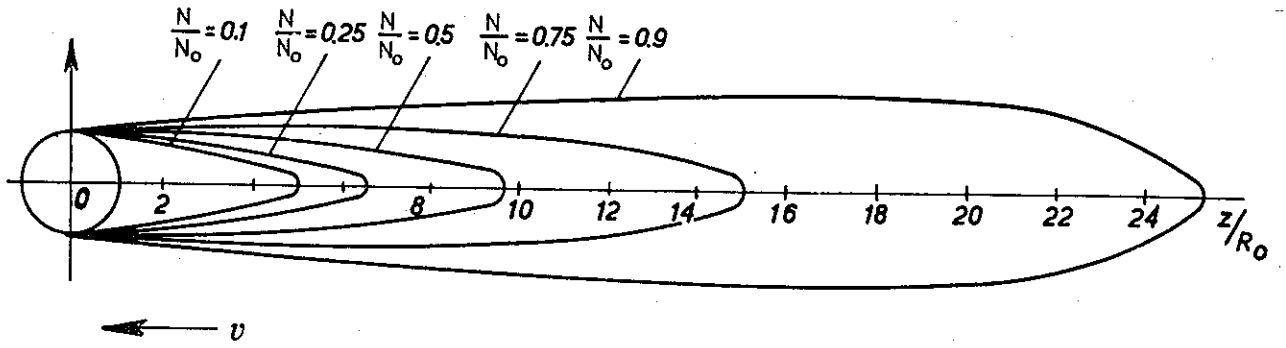

Fig. AI.3. Curves of constant rarefaction, $\frac{N}{N_o}$, at the rear of a spherical body moving with velocity $M = 8$ (after Al'pert *et al.* 1963).

For charged particles the conditions are further complicated, as their motion is also dependent on magnetic and electric fields. These disturbances of the plasma, asymmetric around the spacecraft, can produce substantial errors in the measurements whenever one of the booms lies in a disturbed region. The physics and behaviour of the plasma around a moving body have been studied in laboratory plasma by Knott & Pedersen (1970), and detailed theoretical investigations have been made by Al'pert *et al.* (1963). Some of their results will be applied.

The shape and extension of both the shock and the wake regions are to a great extent determined by the 'Mach number', M, defined as the ratio of body velocity to the local velocity of sound, $M = v_R/v_a$; $v_a \approx \left(\frac{2\kappa T}{m_i}\right)^{1/2}$. The condensation region will not extend far out from the spacecraft, *cf.* Fig. AI. 2 which shows computed values for the shock stand-off distance, Δ, in the lower ionosphere for a spherical body with radius R_o. Thus, this disturbed region will not have any influence on the signals from long probes, where $d' \gg 10\Delta$.

The region of rarefaction at the lee side is of greater importance. For a spherical object this wake has the approximate shape of a cone. Figure AI.3 shows the degree of rarefaction (N/N_o) for $M = 8$ (after Al'pert *et al.* 1963). The curves are computed without taking the earth's magnetic field into account. If, however, $r_{ci}/R_o > 3$, the effect of the magnetic field is negligible, and even

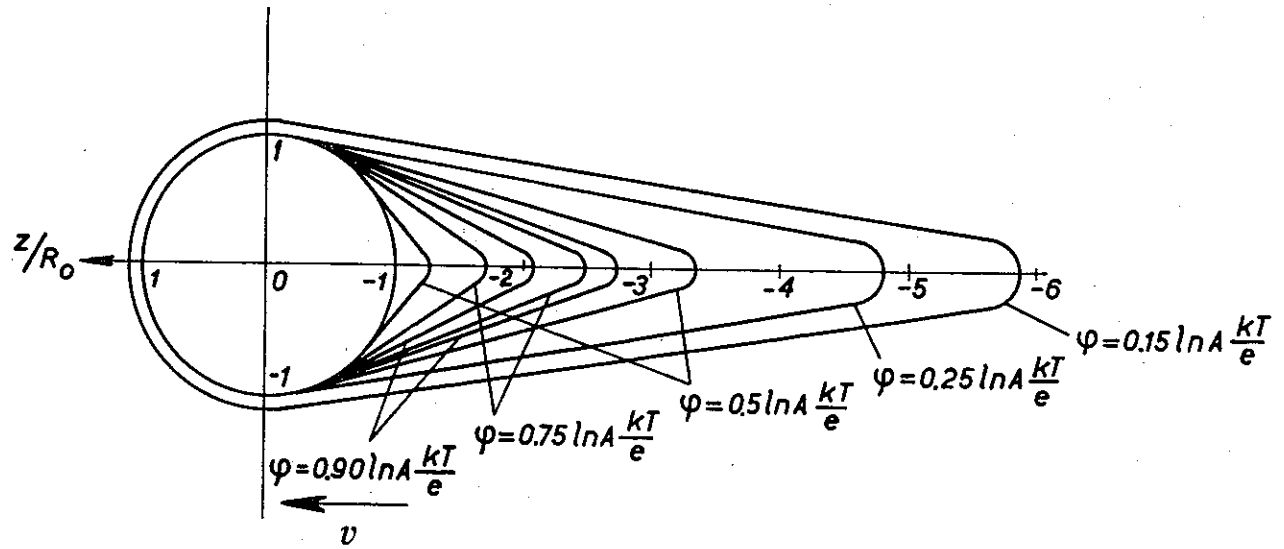

Fig. AI.4. Distribution of the potential in the neighbourhood of a metal sphere with radius R_o moving with velocity $M = 8$. The potential of the sphere is set $-\varphi = \frac{1}{4}\frac{\kappa T}{e} \ln A$, $A = \frac{R_o}{\lambda_D}$ (after Al'pert *et al.* 1963).

at $r_{cl}/R_o = 1$ the modifications caused by B are not important (Al'pert *et al.*, *loc. cit.*).

The perturbations of electron and ion distribution will also disturb the electric field configuration around the body. Achieving an approximate solution of Poisson's equation in the wake region, Al'pert and co-workers found a potential distribution as shown in Fig. AI.4. The wake region can be divided in two zones. In the outer region which is defined by $\frac{N_i(r)}{N_{io}}\left(\frac{R_o}{\lambda_D}\right)^2 \gtrsim 1$, the electric potential is given as $\varphi = \frac{\kappa T}{e} \ln \frac{N_{io}}{N_i}$. N_{io} is the ion density in the undisturbed plasma. The boundary between the regions will for $M = 8$ stretch out to approximately 2.5 R_o in the $-\mathbf{v}_R$ direction. Inside the region of maximum rarefaction the electric potential will stay constant at a value $\frac{\kappa T}{e} \ln\left(\frac{R_o}{\lambda_D}\right)^2$ for a specularly reflecting body. For a metal surface the potential will, however, undergo considerable changes within this zone, but it will still have a maximum value $\frac{\kappa T}{e} \ln\left(\frac{R_o}{\lambda_D}\right)^2$, which is reached at distance $\approx R_o$ from the surface.

At the Mach numbers under consideration, the wake will extend say 15 R_o and disturb the plasma significantly out to about 2 m for a rocket in the lower ionosphere. This means that even with the use of long cylindrical probes a substantial part of the element will occasionally be within the wake region.

The error introduced under these circumstances will come from violation of the symmetry in the probe configuration. The part of the probe, l, within the wake region will not be at the floating potential, φ_o, so that in the differential subtraction $\varphi_A - \varphi_B$ (Eq. (5.11)) a DC offset voltage, $\Delta\varphi_v$, will appear. This error will be on the order of $\frac{\kappa T}{e}\frac{l}{d'}$. With the numerical values $T = 250$ K, $l = 2$ m, and $d' = 6$ m we get $\Delta\varphi_v \approx 8$ mV. The wake effect will thus give significant variations in the signal levels, unless corrective steps are taken.

This error can be minimized either by increasing d' or insulating the part of the boom situated in the wake region electrically from the plasma. As the last method involves least practical difficulties, this will usually be preferred.

Besides the DC error introduced by the distorted probe potential inside the wake, we can expect variations in the AC voltages. Obviously, one field component will be present at twice the spin frequency, but the effects induced in the rest of the spectrum is difficult to estimate both in magnitude and spectral components. The AC signal can, for instance, arise directly from the potential variations seen over the wake region, or secondary effects as plasma instabilities within the wake can be present. In any case it is not possible to predict the erroneous contribution to the signal, but one should be aware that AC disturbances can also be introduced whenever one of the probes lies within the wake region.

iv) Work function errors: Variations in work function over the probe surface can cause unbalance in the probe potentials and thus introduce systematic errors in the measurements. Wilson & Garside (1968) found that variations in work function of a probe could cause potential differences ranging from a few mV when considerable precaution was taken to as much as 200 mV when the surfaces were handled. Extreme care is thus required in the preparation of the probe surfaces. This will be of special importance where the probes are exposed to sunlight. A fingerprint on one of the booms may cause changes in photon-emission current which results in a detectable error voltage (Aggson & Heppner 1966).

v) Sheath overlap: The plasma sheath surrounding the spacecraft will to some extent overlap the boom sheath. This will act as a bridge with finite impedance, and may more or less short circuit the booms. Model experiments have been carried out to simulate this effect (Kapetanakos 1965). The results showed that the sheath overlap has very little effect on the probe floating potential ($< 1.5\%$). Even less influence can be expected where the inner part of the elements are electrically insulated from the plasma.

vi) Spacecraft potential and interference: For ionospheric conditions, where $\lambda_D \ll d$, the DC

field induced by the potential of the vehicle will fall off rapidly and not introduce any difficulties in measurements with long symmetrical booms.

The AC fields around the spacecraft have a wider range, and as the signals can also be introduced into the system through the electronics, and not only via the antennas, this can give rise to serious disturbances. The interference fields may be radiated from the payload electronics, from currents in leads and structure, and it may be caused by RF radiation from the telemetry. The first two effects are reduced by careful electronic design and shielding. If effort is made to maintain a symmetrical configuration between probes and source of interference, this component will be further minimized by the common mode rejection.

The wavefield from the telemetry transmitter can influence the measurements by ionization due to RF excitation, which increases the electron density, or by absorption of RF energy, which will increase the temperature. Both effects will lead to variations in the floating potential, but their influence has in practice turned out to be negligible (Smith 1967).

A more severe interference may arise from demodulation of the RF signal caused by unlinearities in, and before, the input stage of the electronics. In the kind of telemetry systems used, the demodulated signal will just be in the frequency region of interest and will mix with the wanted signal. In broadband recordings this will cause a disturbing effect, but it is possible to distinguish between the artificial and natural signal as long as the interference does not saturate the amplifiers. In spectrometric recordings, it can be more troublesome to separate the real signals and the interference. As the primary source is the RF signal, well outside the frequency region of interest, this problem can be reduced by RF filtering. In addition, carefulness in performance of connections and in selection of components is necessary.

vii) Asymmetric photon-emission, shadowing: In the case of sunlight, errors can arise when the spacecraft casts shadow on one of the booms (Pedersen 1972). Differences in illuminated area will cause assymmetry in photon-emission current and differences in floating potential. These effects will give an error voltage which will be proportional to $\frac{\kappa T}{e}\frac{\Delta S}{S}$, where $\frac{\Delta S}{S}$ is the ratio 'shaded surface to illuminated surface'. For rocket measurements in the ionosphere, this will in most cases not represent any serious source of error, because the shadow is well defined and because the vehicle in most cases has a relatively high spin frequency, so that the induced error voltages only will show up as periodic spikes on the recordings (see *e.g.* Kelley *et al.* 1970). These will be present both in the DC and AC recordings with frequencies as high as $\frac{1}{\tau}$, where τ is the risetime of the pulse.

As the magnetic field influences the particle motion and causes an anisotropy, shading effects will result. The collection of charged particles at the probes will thus depend on the position of the probe with respect to the magnetic field lines. This will make the current distribution over the electrode non-uniform, modify its current/voltage characteristic, and cause the presence of the probe to be felt over a relatively long distance along the magnetic lines of force. As we will have $r_{ce} <$ (probe dimension) $\ll r_{ci}$, only the electrons will be affected. Exact calculations of these effects are difficult, but their results are that the effective collecting surface for electrons will be reduced, resulting in a decrease in the efficiency of the probes (Storey 1963; Aggson & Kapetanakos 1966; Fahleson 1967).

viii) Thermal and aerodynamical bending: In the preceding, the antenna elements have mechanically been considered as ideal rigid bodies, moving through the plasma without bending or other mechanical deformations. Deviations from this stiff rod structure may, however, introduce considerable errors. In the deployment phase the whole boom system is unstable so that measurements are more or less impossible. However, oscillations from this phase can also exist for some time after complete extension of the antenna. Furthermore, the elements are exposed to thermal and mechanical distortions which can cause deformations.

During the deployment phase the antenna must

resist a bending moment, mainly due to the tangential and Coriolis component of acceleration. Considering an antenna element, dr, located at $\mathbf{r}$, rotating with an angular velocity $\boldsymbol{\omega}$, the acceleration of dr is

$$\mathbf{a} = \frac{\partial^2 \mathbf{r}}{\partial t^2} + 2\boldsymbol{\omega} \times \frac{\partial \mathbf{r}}{\partial t} + \mathbf{r} \times \frac{\partial \boldsymbol{\omega}}{\partial t} + \boldsymbol{\omega} \times (\boldsymbol{\omega} \times \mathbf{r}) . \quad \text{(AI.6)}$$

The various contributions are, in order; acceleration due to nonuniform antenna extension (negligible), Coriolis, tangential, and centrifugal acceleration. From Eq. (AI.6) the following scalar expression is obtained for the normal load distribution, $F(r)$, along the antenna

$$F(r) = -(2\,\dot{r}\omega - r\dot{\omega})\,\eta\,dr . \quad \text{(AI.7)}$$

η is linear density of the antenna element. It is required that the element remains straight during extension, so that $\boldsymbol{\omega} \times (\boldsymbol{\omega} \times \mathbf{r})$ does not contribute to $F(r)$. From Eq. (A1.7) we obtain the bending moment at a distance r along the antenna, $M_\omega(r)$

$$M_\omega(r) = \int_r^{d'} r\,F(r)\,dr = -\eta(d'-r)^2 \times [v\omega - \tfrac{1}{6}\dot{\omega}(2d'+r)] . \quad \text{(AI.8)}$$

$\omega(t)$ and $\dot{\omega}(t)$ can be found from the principle of conservation of angular momentum knowing the extension rate of antenna elements.

The requirement for the element to remain straight during extension defines from empirically derived mechanical properties a maximum allowable bending moment, which in turn will determine the maximum extension rate at a given spin frequency. For one type of *STEM* antenna where the elements, made of BeCu, have the dimensions $a = 0.0035$ m, $d' = 6$m, and $\eta = 0.0082$ kg m^{-1} the critical bending moment is 0.11 N m (SPAR, priv. com.). For a rocket with initial spin 1.1 Hz and moment of inertia 2.7 kg m^2 this will define a maximum extension rate of 0.1 m s^{-1}.

Aerodynamical effects, atmospheric drag, will put restrictions both on maximum boom length and the lowest altitude where measurements can be completed with a certain boom construction.

We will consider an antenna element dr. The radius of the element is a, and it has a velocity, $\mathbf{v}_R$, relative to surrounding medium. This will produce a pressure, p, and a corresponding force, $d\mathbf{F}_p$ on the element

$$d\mathbf{F}_p = 2pa\,|\hat{\mathbf{p}} \times \hat{\mathbf{r}}|\,\hat{\mathbf{p}}\,dr . \quad \text{(AI.9)}$$

(*cf.* Fig. AI.5 for explanation of the vectors).

If we are only looking for an approximate expression, and do not take reflectability of the surface into account, the force can be expressed as

$$d\mathbf{F}_p = 2\,\varrho v_R^2 a \sin\gamma\,\hat{\mathbf{p}}\,dr , \quad \text{(AI.10)}$$

where ϱ is the atmospheric mass density. The attached bending moment will be

$$M_p(r) = \int_r^{d'} r\,dF_p . \quad \text{(AI.11)}$$

To estimate the importance of this force, $M_p(0)$ (*i.e.* bending moment at the root of the element) has been calculated for the same antenna elements as used in the examples earlier in this section. The velocity has been taken from the descent of a typical Nike–Tomahawk payload (F24). The result is shown in Fig. AI.6, where also the critical bending moment (0.11 N m) is marked off. It can be seen that critical conditions are reached at ≈ 90 km. Below this altitude deviations from the perfect straight probe configuration can be expected. The atmospheric drag will finally cause the antenna elements to break off. The first ef-

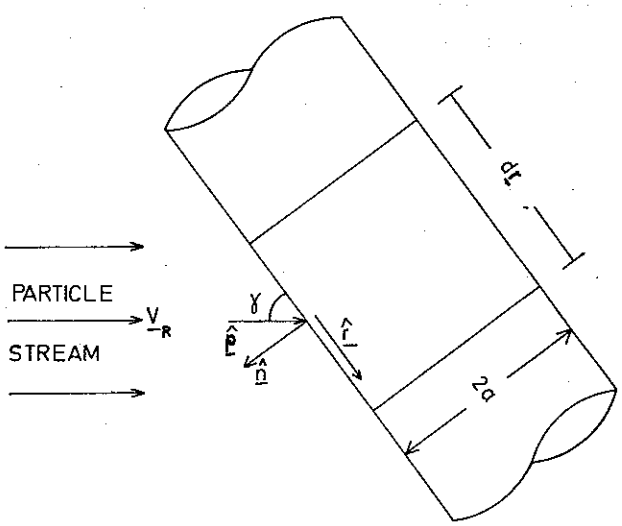

Fig. AI.5. Sketch showing the geometrical configuration of the force on an antenna element, due to atmospheric drag. The velocity of the medium relative to the antenna is $\mathbf{v}_R$.

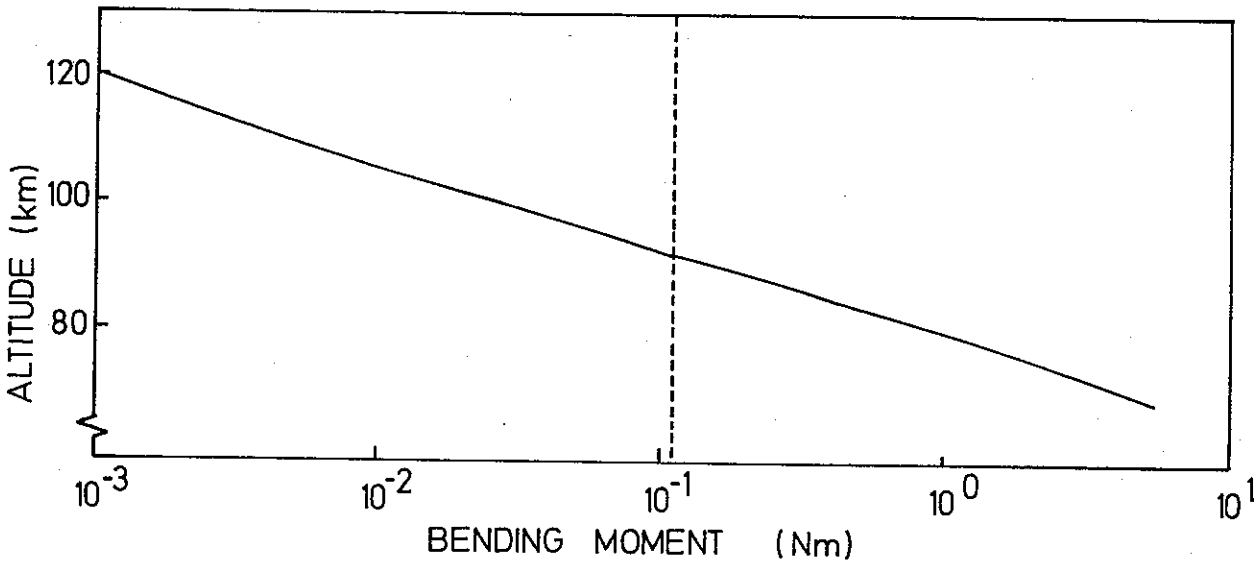

Fig. AI.6. Bending moment at the root of the antenna element for the type of antennas and rockets used in the present measurements calculated as function of altitude for a mean model atmosphere (*cf.* Fig. 3.1). The dashed line represents the critical bending moment.

fects, the bending of the probes, will, however, disturb the assumed geometrical configuration, and will cause an apparent artificial change in the DC field recordings. This can, however, be rather easily recognized (*cf.* last part of the *E*-field curve in Fig. 5.12).

If exposed to sunlight the antenna elements may be subjected to thermal distortion, as a result of differential heating. As this effect will obviously have no influence on ionospheric rockets, it is unnecessary to comment further on it here. One should, however, be aware that this can result in considerable disturbances in satellite measurements (*cf.* Mar & Garrett 1969).

ix) Temperature and plasma gradients, particle fluxes: Effects of more sporadic nature, thus difficult to foresee and more difficult to distinguish from real field variations, can be caused by variations in the ambient plasma. Velocity gradients have already been mentioned (Sect. AI.1). In a similar way it can be deduced from Eq. (5.10) that the contact potential will be sensitive to density and temperature gradients. These variations in plasma parameters may very well be a direct result of a wavefield. The fluctuations in contact potential caused by such irregularities are thus correlated with the electric field to be measured, and produce systematic rather than random errors. To distinguish between the contribution from the wave and the irregularities is from a single un-biased probe system very difficult, and absolute determination of the amplitude of AC electric fields may therefore be subjected to great uncertainties.

Variations in the floating potential can also be caused by influx of high energy particles. The problem has been studied by *e.g.* Betlinger (1965), and the following approximate expression for the probe potential appears from considerations of the currents, similar to those made in Sect. 5.5.

$$\varphi_o \approx -\frac{\kappa T_e}{e} \ln \frac{J_e}{J_i + J_{ph} + \pi a d' e\,(\Psi_i - \Psi_e)}, \tag{AI.12}$$

where Ψ_e and Ψ_i are the flux density for high energy electrons and ions, respectively. This effect can modify the probe potential considerably, especially if the 'flux-current' is of the same order or greater than the 'plasma-currents', *i.e.* (*cf.* Eqs. (5.4) and (AI.1)) when $\Psi_i - \Psi_e > N_e \left(\frac{8\kappa T_e}{\pi m_e}\right)^{1/2}$ for the ion flux and $\Psi_e - \Psi_i \gtrsim \left[\frac{j_{ph}}{e} + N_i \left(\frac{8\kappa T_i}{\pi m_i} + v_R^2\right)^{1/2}\right]$ for the electron flux. A moderate homogeneous particle flux does not, in itself, create any differential voltage between the two

probes. If, however, the flux is inhomogeneous an error is produced, and it will be difficult to distinguish this from real field variations without simultaneous particle measurements.

APPENDIX II: THE IMPEDANCE OF A CYLINDRICAL PROBE IN A PLASMA

In an analysis of short cylindrical antennas Aggson & Kapetanakos (1966) showed that for VLF and ELF frequencies the impedance is determined primarily by the sheat impedance.

The coupling between the plasma and the probe over the plasma sheath can be regarded as a resistor and a capasitor in parallel, as illustrated in Fig. AII.1a, and the equivalent circuit for the antenna and the preamplifier input is sketched in Fig. AII.1b. A voltage V induced in the antenna will represent a signal voltage V' at the input of the preamplifier which is given by

$$V' = V\frac{Z_i}{Z_i+Z_o}, \qquad \text{(AII.1)}$$

where Z_i and Z_o represent the impedance of the amplifier input and the antenna, respectively. The ideal condition will be $Z_i \gg Z_o$, so that $V' \approx V$.

The antenna impedance, formed by the sheath capasitance C_o and the sheath resistance R_o in parallel, can be expressed as

$$|Z_o| = \left(\frac{R_o^2}{1+4\pi^2 f^2 C_o^2 R_o^2}\right)^{1/2}. \qquad \text{(AII.2)}$$

It is important to determine the relative magnitude of R_o and C_o since these two quantities, acting electrically in parallel on the antenna, define a transition frequency given by the expression

$$f_o = \frac{1}{2\pi R_o C_o}. \qquad \text{(AII.3)}$$

Below this frequency the resistive impedance will dominate, while at frequencies above f_o one has a capacitive coupling between the antenna and the plasma. The transition frequency is also the upper frequency limit for the validity of the derivations made in Sect. 5.5, since the assumed equilibrium condition will not be reached above this frequency.

In order to derive an expression for C_o one has to assume a charge distribution in the sheath. The adopted distribution function is shown in

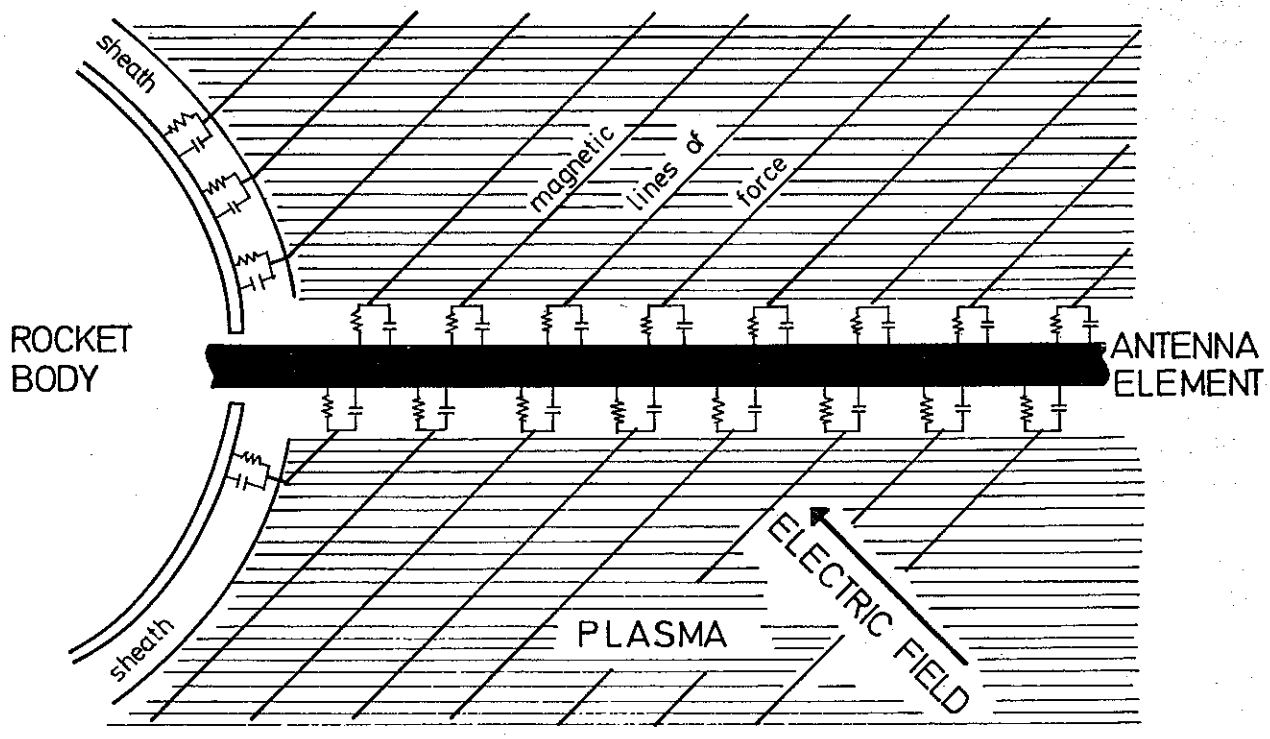

Fig. AII.1.a. Sketch showing the coupling between the plasma and the antenna element over the plasma sheath.

Fig. AII.1.b. Impedance of a double probe system.

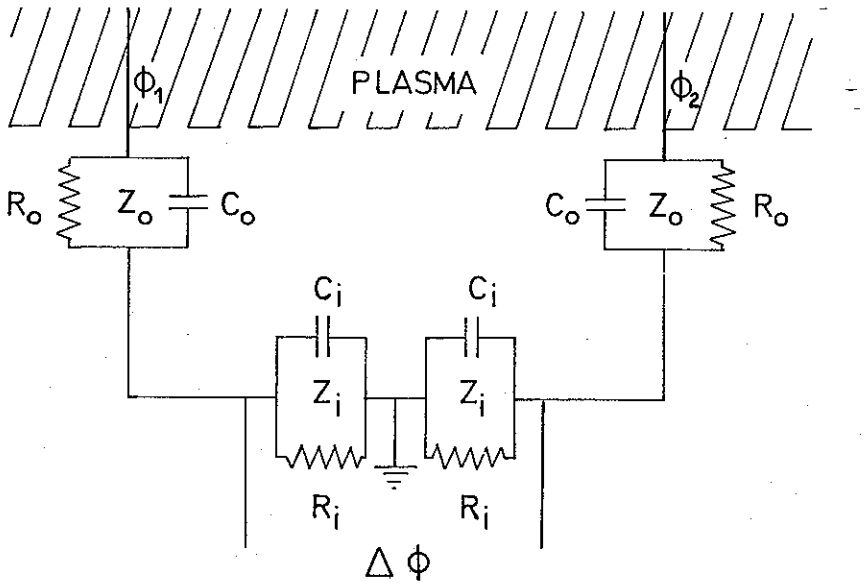

Fig. AII.2. It consists of a region extending from the probe surface at a, to a distance $a+b$ where the charge distribution is constant, and then a transition region of thickness $\alpha\lambda_D$ (α is a constant of the order of unity) where a change in distribution from pure sheath conditions to the charge neutral plasma conditions takes place.

The charge inside a tube with inner and outer radii a and b, length d', and where the charge distribution is $\varrho(r)$, is given by

$$q(r) = 2\pi d' \int_a^b \varrho(r) r \, dr \,. \qquad \text{(AII.4)}$$

The total charge inside the probe sheath, $q(s)$, can then be calculated from

$$q(s) = 2\pi d' \int_a^{a+b+a\lambda_D} \varrho(r) r \, dr \,. \qquad \text{(AII.5)}$$

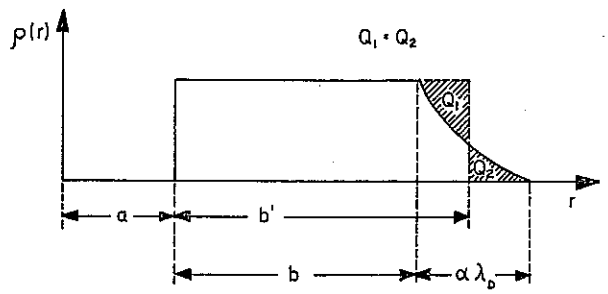

Fig. AII.2. Model charge distribution in the plasma sheath used in the calculation of the probe capacitance.

Using Gauss' law and $\mathbf{E} = -\nabla\varphi$, the following expression can be derived for the potential of the antenna:

$$\varphi = \frac{1}{2\pi\varepsilon_o d'} \int_a^{a+b+a\lambda_D} \frac{[q(s)-q(r)]}{r} dr \,. \qquad \text{(AII.6)}$$

ε_o is the permittivity of free space.

As capacity can be defined as $C = \dfrac{dq}{d\varphi}$, C_o can be derived from:

$$C_o = \frac{dq(s)}{d\varphi(b)} = \frac{dq(s)}{db}\frac{db}{d\varphi} = \frac{dq(s)/db}{d\varphi/db} \,, \qquad \text{(AII.7)}$$

supposing $\dfrac{d\varphi}{db} \neq 0$. Evaluation of $\dfrac{d\varphi}{db}$, using the rule for differentiations of integrals where the limits for integration are functions of the differential parameter, and substitution of this into Eq. (AII.7), gives the probe capacity as

$$C_o = \frac{2\pi\varepsilon_o d'}{\ln \dfrac{a+b+\alpha\lambda_D}{a}} \,. \qquad \text{(AII.8)}$$

It can be seen that for $\alpha = 0$, *i.e.* a 'box' distribution of the charge in the plasma sheath, one gets the expression for a coaxial capacitor formed by the probe (radius a) and the boundary of the sheath (radius $a+b$). It should be noted that the expression for C_o does not contain ϱ or $q(s)$, so that only information of b and $\alpha\lambda_D$ is needed.

Assuming a constant charge density, $N_e e$, between the limits a and $a+b' = a+b+\frac{\alpha}{2}\lambda_D$, $q(s)$ can be found by integration of Eq. (AII.5)

$$q(s) = \pi d' N_e e\,[(a+b')^2 - a^2]\,, \qquad \text{(AII.9)}$$

and further from Eq. (AII.6)

$$\varphi = \frac{N_e e}{2\varepsilon_o}\left\{(a+b')^2 \ln\frac{a+b'}{a} - \tfrac{1}{2}[(a+b')^2 - a^2]\right\}. \qquad \text{(AII.10)}$$

If the probe potential is known (Eq. (5.5)), it is then possible to find the sheath thickness from Eq. (AII.10) and the capacitance from Eq. (AII.8) It should be noted that since $C_o = f(\ln(b, \lambda_D))$, one will not expect large variations in the antenna capacity with the change of plasma parameters in the ionosphere.

To calculate the sheath resistance we will make use of the relation

$$R_o = \frac{\partial \varphi}{\partial J}\,. \qquad \text{(AII.11)}$$

Differentiation of Eq. (AI.5) gives

$$R_o = \frac{\kappa T_e}{e}\,\frac{1}{\int j_{io}\,dS + \gamma\int j_{pho}\,dS + J}\,. \qquad \text{(AII.12)}$$

If we assume the voltmeter current to be negligible, we arrive at the following expression for the sheath resistance at night conditions ($J_{ph} = 0$)

$$R_o = \left(\frac{\kappa m_i}{2\pi a^2 d^2 e^4}\,\frac{T_e^2}{N_i^2 T_i}\right)^{1/2}. \qquad \text{(AII.13)}$$

It can be noted that R_o is much more sensitive to variations in the plasma parameters than the capacitive part of the antenna impedance.

Based on the equations derived in this section and the mean ionospheric model given in Chapter 3, the antenna parameters R_o, C_o, f_o and Z_o for $f = 2.5$ kHz have been calculated as a function of altitude for the antenna element used in our measurements, and are plotted in Fig. AII.3. It is seen that the coupling is resistive below roughly 2 kHz in the E-region and below 5–10 kHz in the F-region.

ACKNOWLEDGEMENTS

This work, started in 1969, was accomplished as part of the research programme at the Norwegian Institute of Cosmic Physics. The author wishes to express his gratitude to the Director of the Institute, Professor A. Egeland, for providing the opportunity to undertake the studies, and for advice and encouragement through numerous discussions.

The importance of the contributions from Drs. N. C. Maynard and D. Evans, and from the

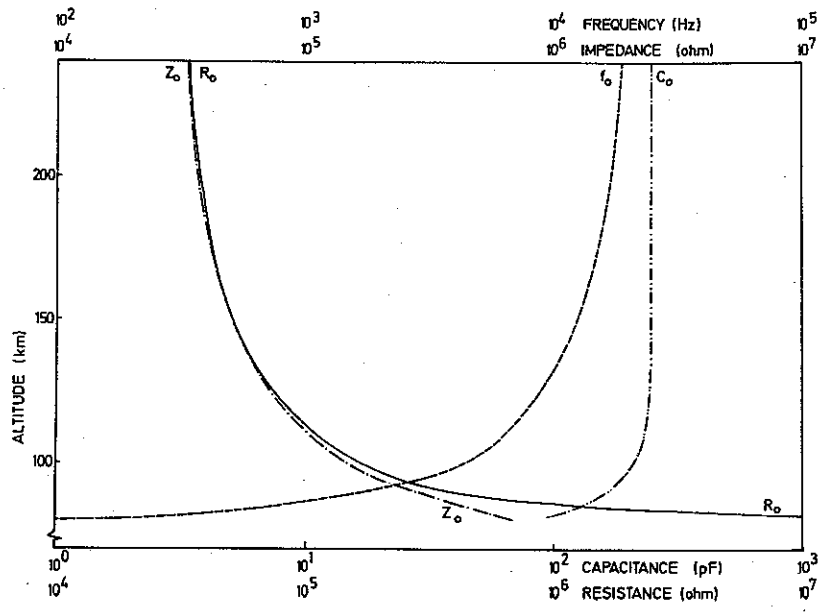

Fig. AII.3. Resistance, R_0, capacitance, C_0, and impedance at 2.5 kHz, Z_0, as function of altitude for an antenna element used in the present experiments. The curve f_0 gives the transition frequency. The calculations are based on a mean model ionosphere (*cf.* Fig. 3.4).

Fields and Plasmas Branch at Goddard Space Flight Center/National Aeronautics and Space Administration, should be stressed. Their support with the rocket instrumentation was essential for the completion of this work. Valuable assistance from Dr. K. V. Paulson, University of Saskatchewan, in the reduction of the VLF propagation data, is also gratefully acknowledged.

Thanks are due to Dr. E. Ungstrup, Danish Space Research Institute, for permission to use data from the rocket S70/1 prior to publication.

It is a pleasure to acknowledge the skilful and valuable assistance from Mr. L. T. Lyngdal, Mr. T. A. Sten, and Mr. K. Måseide. Likewise the author expresses his gratitude to Mrs. B. Crow and Mrs. L. Firing for secretarial work.

Ionospheric data were provided by The Auroral Observatory, Tromsø, and by Kiruna Geophysical Observatory, Sweden.

The payload integration was competently handled by Mr. Lars Lorntzsen and collaborators at the Norwegian Defence Research Establishment and by Christian Michelsen's Institute, Bergen.

The Royal Norwegian Council for Industrial and Scientific Research partly sponsored the research program and was responsible for operating and administering the launching facilities at Andøya.

The author would also like to acknowledge financial support received from the Roald Amundsen Memorial Foundation during the research period.

REFERENCES

Abel, W. G. & Newell, R. E. 1969: *J. Geophys. Res. 74*, 231

Aggson, T. L. 1969: p. 305 in *Atmospheric Emissions* (Eds. B. M. McCormac and A. Omholt) Van Nostrand Reinhold, New York.

Aggson, T. L. & Heppner, J.P. 1966: 'A proposal for tri-axial electric field measurements on IMP spacecraft H, I, and J'. NASA, Goddard Space Flight Center, Greenbelt, Md.

Aggson, T. L. & Kapetanakos, C. A. 1966: *NASA/GSFC Rep. No. X-612-66-380*, Goddard Space Flight Center, Greenbelt, Md.

Aggson, T. L. Maynard, N. C. & Heppner, J. P. 1965: 'A proposal for electric field measurements on OGO-E (EGO-3)'. NASA, Goddard Space Flight Center, Greenbelt, Md.

Akasofu, S. -I. 1966: *Space Sci. Rev. 6*, 21.

Akasofu, S. -I. 1968: *Polar and Magnetic Substorms*, Springer-Verlag New York Inc., New York.

Akasofu, S. -I. & Meng, C. -I, 1969; *J. Geophys. Res. 74*, 293.

Al'pert, Ja. L., Gurevic, A. V. & Pitaevskij, L. P. 1963: *Space Sci. Rev. 2*, 680.

Alfvén, H. 1939: *Kungl. Sv. Vetsk-Akad. Handl. III 18*. No. 3.

Alvén, H. 1940: *Kungl. Sv. Vetsk-Akad. Handl. III 18*. No. 9.

Alfvén, H. 1950: *Cosmical Electrodynamics*, Clarendon Press, Oxford.

Alfvén, H. & Fälthammar, C. G. 1963: *Cosmical Electrodynamics*, 2nd Ed., Clarendon Press, Oxford.

Armstrong, J. C. & Zmuda, A. J. 1970: *J. Geophys. Res. 75*, 7122.

Axford, W. I. & Hines, C. O. 1961: *Can. J. Phys. 39*, 1433.

Baker, D. A. & Hammel, J. E. 1962: *Phys. Rev. Letters 8*, 157.

Baker, W. G. & Martyn, D. F. 1953: *Phil. Trans. Roy. Soc. London A 246*, 281.

Balsley, B. B. & Ecklund, W. L. 1972: *J. Geophys. Res. 77*, 4746.

Banks, P. 1966a: *Planet. Space Sci. 14*, 1085.

Banks, P. 1966b: *Planet. Space Sci. 14*, 1105.

Bates, D. R. 1970: *Contemp. Phys. 11*, 105.

Belrose, J. S. 1967: *Nature 214*, 660.

Bernstein, I. B. 1968: *Phys. Rev. 109*, 10.

Bernstein, I. B. & Kulsrud, R. M. 1960: *Phys. Fluids 3*, 937.

Bettinger, R. T. 1965: In *Interactions of Space Vehicles with an Ionized Atmosphere* (Ed. S. F. Singer), Pergamon Press, London.

Bhatnagar, P. L., Gross, E. P. & Krook, M. 1954: *Phys. Rev. 94*, 511.

Birkeland, K. 1908: *The Norwegian Aurora Polaris Expedition 1902–1903. Vol. 1, 1st Sec.*, H. Aschehoug, Christiania.

Block, L. P. 1966: *J. Geophys. Res. 71*, 855.

Booker, H. G. 1956: *J. Atmosph. Terr. Phys. 8*, 204.

Boström, R. 1964: *J. Geophys. Res. 69*, 4983.

Boström, R. 1968: p. 445 in *The Birkeland Symposium on Aurora and Magnetic Storms* (Eds. A. Egeland and J. Holtet), CNRS, Paris.

Boström, R. 1973: p. 183 in *Cosmical Geophysics* (Eds. A. Egeland, Ø. Holter and A. Omholt), Universitetsforlaget, Oslo.

Bowhill, S. A. & Geisler, J. E. 1966: p. 487 in *Space Research VI*, (Ed. R. L. Smith–Rose), MacMillan & Co., London.

Bowles, K. L., Balsley, B. B. & Cohen, R. 1963: *J. Geophys. Res. 68*, 2485.

Buneman, O. 1959: *Phys. Rev. 115*, 503.

Buneman, O. 1963: *Phys. Rev. Letters 10*, 285.
Cain, J. C. & Cain, S. 1968: *NASA/GSFC Rep. No. X-612-68-501*, Goddard Space Flight Center, Greenbelt, Md.
Camnitz, H. G., Tsunoda, R. T. & Barczys, D. A. 1969: *Tech. Report, Cal 2469-P-1*, Cornell Aerospace Lab.
Carpenter, D. L. 1970: *J. Geophys. Res. 75*, 3837.
Caufman, D. P. & Gurnett, D. A. 1971: *J. Geophys. Res. 76*, 6014.
Celsius, A. 1741: *Kungl. Sv. Vetsk-Akad. Handl. 1*, 391.
Chapman, S. 1931: *Proc. Phys. Soc., London 43*, 26.
Chapman, S. 1935: *Terr. Mag. Atmos. Elec. 40*, 349.
Chen, W. M. & Harris, R. D. 1971: *J. Atmosph. Terr. Phys. 33*, 1193.
Chesnut, W. C. 1971: Paper 5 in *Radar Propagation in the Arctic*, AGARD-CP-97.
Chesnut, W. G., Hodges, J. C. & Leadabrand, R. L. 1968: *Report No. RADC-TR-68-286*. Stanford Res. Inst., Calif.
CIRA 1965: *Cospar International Reference Atmosphere 1965*. North Holland, Amsterdam.
Cloutier, P. A., Anderson, H. R., Park, R. V., Vondrak, R. R., Spiger, R. J. & Sandel, B. R. 1970: *J. Geophys. Res. 75*, 2595.
Cummings, W. D. & Dessler, A. J. 1968: *J. Geophys. Res. 72*, 1007.
Davis, T. N. 1966: *Space Sci. Rev. 6*, 222.
Davis, T. N. 1967: p. 133 in *Aurora and Airglow* (Ed. B. M. McCormac), Reinhold, New York.
Davis, T. N. 1971: *J. Geophys. Res. 76*, 5978.
Davis, T. N. 1972: *Planet. Space Sci. 20*, 1369.
Deehr, C. S., Gustafsson, G. A., Omholt, A., Anderson, L., Egeland, A. & Borg, H. 1970: *Phys. Norv. 4*, 101.
Desloge, E. A. 1962: *Phys. Fluids. 5*, 1223.
Dougherty, J. P. 1963: *J. Fluid Mech. 16*, 126.
Dougherty, J. P. & Farley, D. T. 1967: *J. Geophys. Res. 72*, 895.
Dungey, J. W. 1961: *Phys. Rev. Letters 6*, 47.
Egeland, A. 1962a: *Arkiv för Geofysik 4*, 103.
Egeland, A. 1962b: *Arkiv för Geofysik 4*, 171.
Egeland, A. 1973: p. 313 in *Cosmical Geophysics* (Eds. A. Egeland, Ø. Holter, and A. Omholt), Universitetsforlaget, Oslo.
Egeland, A., Bjøntegaard, G. & Aggson, T. 1970: *J. Atmosph. Terr. Phys. 32*, 1191.
ESSA 1970: *Solar Geophysical Data, No. 309 – Part I*, ESSA Research Laboratories, Boulder, Colorado.
Ettenberg, M. 1963: p. 1015 in *Handbook of Microwave Measurements*, 3rd Ed. Vol. III (Eds. M. Sucher and J. Fox). Polytechn. Press, New York.
Evans, D. S. 1971: p. 267 in *The Radiating Atmosphere* (Ed. B. M. McCormac) Reidel Publ. Comp., Dordrecht, Holland.
Evans, D. S., priv. com.: National Oceanic and Atmospheric Administration, Boulder, Colorado.
Evans, J. V. & Mantas, G. P. 1968: *J. Atmosph. Terr. Phys. 30*, 563.
Fahleson, U. 1967: *Space Sci. Rev. 7*, 238.
Fahleson, U., Fälthammar, C. -G., Pedersen, A., Knott, K., Brommund, G., Schumann, G., Haerendel, G. & Reiger, E. 1971: *Radio Science 6*, 233.
Farley, D. T. 1959: *J. Geophys. Res. 64*, 1225.
Farley, D. T. 1963: *J. Geophys. Res. 68*, 6083.
Fejer, J. A. 1961: *Can. J. Phys. 39*, 1409.
Flood, W. A. 1967: p. 563. in *Aurora and Airglow* (Ed. B. M. McCormac), Reinhold, New York.
Folkestad, K. 1970: *NDRE Report No. 59*, Norwegian Defence Research Establishment, Kjeller.
Forsyth, P. A. 1968: p. 153 in *The Birkeland Symposium on Aurora and Magnetic Storms* (Eds. A. Egeland and J. Holtet), CNRS, Paris.
Forsyth, P. A. & Lyon, G. F. 1971: Paper 11 in *Radar Propagation in the Arctic*, AGARD-CP-97.
Frank–Kamenezki, D. A. 1967: *Vorlesungen über Plasmaphysik*, VEB Deutscher Verlag der Wissenschaften.
Fried, B. D. & Conte, S. D. 1961: *The Plasma Dispersion Function*, Academic Press, New York.
Fukushima, N. 1969: *Rept. Ionosph. Space. Res. Japan 23*, 219.
Gauss, C. F. 1839: *Algemeine Theorie des Erdmagnetismus. Gesammelte Werke 5*, §36.
Graham, G. 1724: *Phil. Trans. Roy. Soc. London 33*, 96.
Gurnett, D. A. & Mosier, S. R. 1969: *J. Geophys. Res. 74*, 3979.
Haerendel, G. & Lüst, R. 1970: p. 213 in *Particles and Fields in the Magnetosphere* (Ed. B. M. McCormac), Reidel Publ. Comp., Dordrecht, Holland.
Haerendel, G. Lüst, R. & Rieger, E. 1967: *Planet. Space Sci. 15*, 1.
Haerendel, G., Lüst, R., Rieger, E. & Völk, H. 1969: p. 293 in *Atmospheric Emissions* (Eds. B. M. McCormac and A. Omholt), Van Nostrand Reinhold, New York.
Hakura, Y. 1965: *Rept. Ionosph. Space Res. Japan, 19*, 121.
Henlen, D. M. & McElroy, M. B. 1968: *J. Geophys. Res. 73*, 2421.
Helliwell, R. A. 1965: *Whistlers and Related Ionospheric Phenomena*. Stanford Univ. Press, Stanford, Calif.
Heppner, J. P. 1972a: *Geofys. Publ. 29*, 105.
Heppner, J. P. 1972b: *Planet. Space Sci. 20*, 1475.
Heppner, J. P., Stolarik, J. D. & Wescott, E. M. 1971a: p. 407 in *The Radiating Atmosphere* (Ed. B. M. McCormac), Reidel Publ. Comp., Dordrecht, Holland.
Heppner, J. P., Stolarik, J. D. & Wescott, E. M. 1971b: *J. Geophys. Res. 76*, 6028.

Hines, C. O. 1960: *Can. J. Phys. 38*, 1441.
Hines, C. O. 1963: *Quart. J. Royal Meteorol. Soc. 89*, 1.
Hoffman, R. A. & Evans, D. S. 1968: *J. Geophys. Res. 73*, 6201.
Hoh, F. C. 1963: *Phys. Fluids 6*, 1184.
Holt, O. 1973: p. 283 in *Cosmical Geophysics* (Eds. A. Egeland, Ø. Holter, and A. Omholt) Universitetsforlaget, Oslo.
Holtet, J. A., Egeland, A. & Maynard, N. C. 1971a: p. 345 in *The Radiating Atmosphere* (Ed. B. M. McCormac), Reidel Publ. Comp., Dordrecht, Holland.
Holtet, J. A., Egeland, A., Lyngdal, L. T. & Maynard, N. C. 1971b: In *Proceedings of the SAR Symposium, Kiruna March 1971. KGO Report No.* 714, Kiruna Geophysical Observatory, Kiruna.
Hooper, E. B. & Walker, J. C. G. 1971: *J. Atmosph. Terr. Phys. 33*, 1441.
Hultqvist, B. 1968: *KGO Report No.* 687. Kiruna Geophysical Observatory, Kiruna.
Hultqvist, B. 1971: *Planet. Space Sci. 19*, 749.
Hultqvist, B. 1972: *Geofys. Publ. 29*, 27.
IAGA 1968: *IAGA News 7*, 49.
Iwai, A,. Outsu, J. & Tanaka, Y. 1966: *Proc. Res. Inst. Atmospherics Nagoya Univ. 13*, 1.
Johnson, C. Y. 1969: p. 197 in *Annals of the IQSY, Vol. 5*. The MIT Press, Cambridge, Mass.
Jørgensen, T. S. & Ungstrup. E. 1966: p. 101 in *Electron Density Profiles in Ionosphere and Exosphere* (Ed. J. Frihagen), North-Holland, Amsterdam.
Kapetanakos, C. 1965: In 'A proposal for electric field measurements on OGO-E (EGO-3)' (Aggson, T. L., Maynard, N. C., and Heppner, J. P.), NASA, Goddard Space Flight Center, Greenbelt, Md.
Karlson, E. T. 1963: *Phys. Fluids 6*, 708.
Kato, S. 1963: *Planet. Space Sci. 11*, 823.
Kato. S. 1964: *Planet. Space Sci. 12*, 1.
Kato, S. & Hirata, Y. 1967: *Rept. Ionosph. Space Res. Japan, 21*, 85.
Kelley, M. C., Mozer, F. S. & Fahleson, U. V. 1970: *Planet. Space Sci. 18*, 847.
Kern, J. W. 1962: *J. Geophys. Res. 67*, 2649.
Kim, J. S. & Volkman, R. A. 1963: *J. Geophys. Res. 68*, 3187.
Kimura, I. & Nishina, R. 1967: *Rept. Ionosph. Space Res. Japan 21*, 187.
Knott, K. & Pedersen, A. 1970: *ELDO/ESRO Scientific Tech. Rev. 2*, 499.
Knox, F. B. 1972: *J. Atmosp. Terr. Phys. 34*, 747.
Kraus, J. D. 1950: *Antennas*. McGraw–Hill, New York.
Leadabrand, R. L., Schlobohm, J. C. & Barron, M. J. 1965: *J. Geophys. Res 70*, 4235.
Levy, R. H., Petschek, H. E. & Siscoe, G. L. 1964: *AIAA Journal 2*, 2065.
Lomax, H. & Inouye, M. 1964: *NASA Techn. Rept. R-204*, Ames Res. Center.
Maggs, J. E. & Davis, T. N. 1968: *Planet. Space Sci. 16*, 205.
Mar, J. & Garrett, T. 1969: *Proc. IEEE 57*, 882.
Maynard, N. C. 1972: p. 155 in *Magnetosphere-Ionosphere Interactions* (Ed. K. Folkestad), Universitetsforlaget, Oslo.
Maynard, N. C. & Heppner, J. P. 1970: p. 247 in *Particles and Fields in the Magnetosphere* (Ed. B. M. McCormac), Reidel Publ. Comp., Dordrecht, Holland.
Maynard, N. C., Bahnsen, A., Christophersen, P., Egeland, A. & Lundin, R. 1973: *J. Geophys. Res. 78*, 3976.
McDiarmid, D. R. & McNamara, A. G. 1969: *Can. J. Phys. 47*, 1271.
McNamara, A. G. 1969: *Can. J. Phys. 47*, 1913.
McNamara, A. G. 1971: p. 301 in *The Radiating Atmosphere* (Ed. B. M. McCormac), Reidel Publ. Comp., Dordrecht, Holland.
Mende, S. B. 1968: *J. Geophys. Res. 73*, 991.
Meng. C. -I. & Akasofu, S. -I. 1969: *J. Geophys. Res. 74*, 4035.
Moorcroft, D. R. 1961a: *Can. J. Phys. 39*, 677.
Moorcroft, D. R. 1961b: *Can. J. Phys. 39*, 695.
Moorcroft, D. R. 1966: *Planet. Space Sci. 14*, 269.
Morse, P. M. 1964: *Thermal Physics*, Benjamin Inc. N. Y.
Mott–Smith, H. M. & Langmuir, I. 1926: *Phys. Rev. 28*, 727.
Mozer, F. S. 1968: *J. Geophys. Res. 73*, 999.
Mozer, F. S. 1970: *Planet. Space Sci. 18*, 259.
Mozer, F. S. & Bruston, P. 1967: *J. Geophys. Res. 72*, 1109.
Mozer. F. S. & Fahleson, U. V. 1970: *Planet. Space Sci. 18*, 1563.
Murgatroyd, R. J. 1957: *Quart. J. Royal Met. Soc. 84*, 225.
Mæhlum, B. N. 1973: p. 211 in *Cosmical Geophysics* (Eds. A. Egeland, Ø. Holter and A. Omholt) Universitetsforlaget, Oslo.
Møller, C. 1952: *The Theory of Relativity*, Oxford Univ. Press, London.
Måseide, K., Holtet, J. A., Egeland, A. & Maynard, N. C.. 1973: *J. Atmosph. Terr. Phys. 35*, 1833.
Ogawa, T. & Tohmatsu, T. 1966: *Rept. Ionosph. Space Res. Japan 20*, 395.
Omholt, A. 1971: *The Optical Aurora*, Springer-Verlag, Berlin.
Opik, E. J. 1965: p. 3. in *Interactions of Space Vehicles with an Ionized Ionosphere* (Ed, S. F. Singer), Pergamon Press, New York.
Park, R. J. & Cloutier, P. A. 1971: *J. Geophys. Res. 76*, 7714.

Pedersen, A. 1972: *Internal Working Paper No. 677, European Space Research and Technology Centre*, European Space Research Organisation.
Persson, H. 1967: *Space Sci. Rev. 7*, 228.
Potter, W. E. 1970: *J. Geophys. Res. 75*, 5415.
Potter, W. E. & Cahill, L. J. 1969: *J. Geophys. Res. 74*, 5159.
Ratcliffe, J. A. 1959a: *J. Geophys. Res. 64*, 2102.
Ratcliffe, J. A. 1959b: *The Magneto-Ionic Theory and Its Application to the Ionosphere*. Cambridge, Univ. Press. Cambridge, England.
Rogister, A. 1971: *J. Geophys. Res. 76*, 7754.
Reid, G. C. 1972: p. 39 in *Magnetosphere–Ionosphere Interactions*. (Ed. K. Folkestad) Universitetsforlaget, Oslo.
Rishbeth, H. & Garriott, O. K. 1969: *Introduction to Ionospheric Physics*. Internat. Geophys. Ser., Vol. 14, Academic Press, New York.
Rottman, K. 1961: *Matematische Formelsammlung*, Bibl. Inst. Mannheim.
Sagalyn, R. C., Smiddy, M. & Wisma, J. 1963: *J. Geophys. Res. 68*, 199.
Sandel, B. R. 1970: *J. Geophys. Res. 75*, 2595.
Simon, A. 1963: *Phys. Fluids 6*, 382.
Singleton, D. G. 1962: *J. Atmosph. Terr. Phys. 24*, 909.
Smith, L. G. 1967: In *Electron Density and Temperature Measurements in the Ionosphere* (Ed. K. Maeda), COSPAR Techn. Manual Series, 2.
SPAR, priv. com.: SPAR Aerospace Products, Ltd., Toronto. Ontario, Canada.
Spreiter, J. R. & Briggs, B. R. 1961: *J. Geophys. Res. 66*, 1731.
Steward, B. 1882: p. 36 in *Terrestrial Magnetism*, Encyclopedia Britannica 9th Ed., London.
Stix, T. H. 1962: *The Theory of Plasma Waves*, McGraw–Hill, New York.
Storey, L. R. O. 1963: *Technical Report JO8 TC.*, Centre National d'Etudes de Telecommunications.
Swider, W. 1965: *J. Geophys. Res. 70*, 4859.
Søraas, F. 1973: p. 143 in *Cosmical Geophysics* (Eds. A. Egeland, Ø. Holter, and A. Omholt), Universitetsforlaget, Oslo.
Thomas, L. 1972: in *Aeronomy Report 48* (Eds. C. F. Sechrist Jr., and M. A. Geller), University of Illinois.
Unwin, R. S. & Knox, F. B. 1971: *Radio Science 6*, 1061.
Vestine, E. H. & Chapman, S. 1938: *Terr. Mag. Atmos. Elec. 43*, 351.
Walker, E. H. 1965: In *Interactions of Space Vehicles with an Ionized Atmosphere* (Ed. S. F. Singer). Pergamon Press, New York.
Walker, J. C. G. & Rees, M. H. 1968: *Planet. Space Sci. 16*, 459.
Watson, G. N. 1948: *Theory of Bessel Functions*, Cambridge University Press, New York.
Wedde, T. 1970: *Int. Rep. E-162*, Norwegian Defence Research Establishment.
Wescott, E. M. ,Stolarik, J. D. & Heppner, J. P 1969: *J. Geophys. Res. 74*, 3469.
Wescott, E. M., Stolarik, J. D. & Heppner, J. P 1970: p. 229 in *Particles and Fields in the Magnetosphere* (Ed. B. M. McCormac), Reidel Publ. Comp., Dordrecht, Holland, 229.
Whalen, J. A., Buchau, I. & Wagner, R. A. 1971: *J. Atmosph. Terr. Phys. 33*, 661.
Whitehead, J. D. 1967: p. 89 in *Space Research VII* (Ed. R. L. Smith–Rose), North – Holland Publ., Amsterdam.
Willmore, A. P. 1970: *Space Sci. Rev. 11*, 607.
Wilson, J. W. G. & Garside, G. 1968: *Planet. Space Sci. 16*, 257.
Yonezawa, T. 1968: *J. Atmosph. Terr. Phys. 30*, 473.
Zmuda, A. J., Martin, J. H. & Heuring, F. T. 1966: *J. Geophys. Res 71*, 5033.

Instructions to Authors

GEOPHYSICA NORVEGICA

publishes papers in English. When preparing manuscripts for submission, authors should consult 1973 copies of the journal and follow its style as closely as possible.

MANUSCRIPTS

Manuscript must be typewritten, double spaced throughout, on one side of the paper, with a wide margin. Authors should submit the *original* manuscript (preferably with one copy) to the editor, whose address is shown on page 2 of the cover.

Separate sheets should be used for the following: 1) title page, with the author's name and institution, and, if the title is longer than 40 letters and spaces, a short title not exceeding this limit for use in the running heads; 2) an abstract not exceeding 12 lines (910 letters and spaces) with the name and full postal address underneath of the author to whom communications, proofs, and reprints are to be sent; 3) references; 4) Tables with their headings; 5) legends to Figures.

Brief *Acknowledgements* of grants and other assistance, if any, will be printed at the end of the text.

FIGURES, TABLES, AND MATHEMATICAL SYMBOLS

All illustrations are to be considered as Figures. Each graph, drawing, or photograph should be numbered in sequence with arabic numerals, and should be identified on the back by the name of the journal, the author's name, and the Figure number. The top should be indicated. The Figures should be the original drawing. The columns of *Geophysica Norvegica* are 67 mm broad, and the size of the original drawings should be in proportion. Lines must be thick enough to allow for reduction. Letters and numbers should not be less than 2 mm high in the printed illustration. Photographs should be submitted as unmounted glossy enlargements showing good details.

Tables are to be numbered consecutively with roman numerals. Each Table should be typed on a separate sheet, with a descriptive heading that makes the Table self-explanatory.

All Figures and Tables should be referred to in the text by their number. Their approximate position should be indicated in the margin of the manuscript.

All numbered equations and all unnumbered but complicated equations should be typed on separate lines. Equations should be punctuated.

All text material will be set in roman type unless otherwise marked. Hence, all variables and other characters to be set in italic type should be underlined once with a straight line. Vectors and other characters in boldface type should be indicated by underlining with a single wavy line.

No footnotes should be used.

REFERENCES TO LITERATURE

In the text, Brown (1957, p. 9), Brown & White (1961). If more than two authors, Brown et al. (1963). Multiple references: 'As several authors have reported (Brown 1967, Brown & White 1961, Green et al. 1963)', i. e. chronological order, no commas between names and year.

Lists of References are to be unnumbered and in alphabetical order. The international alphabetical order of Scandinavian and German vowels, should be observed: Å = AA, Æ and Ä = AE, Ø and Ö = OE, Ü = UE. Indicate 1st, 2nd, 3rd, etc. works by the same author in the same year by a, b, c, etc. (White 1966a). No ditto marks should be used. Titles of journals should be abbreviated according to *World List of Scientific Periodicals.*

Examples:

Cadle, R. D. 1966. p. 83 in *Particles in the Atmosphere and Space.* Reinhold Publishing Corporation, New York.

Craig, R. A. 1965. p. 161 in *The Upper Atmosphere. Meteorology and Physics.* International Geophysics Series, Vol. 8. Academic Press, New York and London.

Eliassen, A. & Kleinschmidt, E. 1957. p. 66 in *Handbuch der Physik.* Vol. 48, Part 2, edited by S. Flügge. Springer-Verlag, Berlin.

Junge, C. 1972. *Quart. J. R. Met. Soc. 98,* 711.

PROOFS

Two copies of the first proof will be sent (page proofs). One copy, duly corrected, should be returned to the editor with the least possible delay. All technical parts of the article, including references, names, figures (numbers, formulae), illustrations, etc. are the responsibility of the authors. Authors will be required to pay for any major alterations they may make.

REPRINTS

Fifty reprints of each article will be supplied free. Additional reprints can be ordered at a charge.

International Journals

AMBIO
A Journal of the Human Environment
Research and Management

ARCTIC
Journal of Arctic Biology

BEAVER
Journal of the Northern Forest
Association

BOREAS
An International Journal of Quaternary
Geology

DEVELOPMENT
An International Forum for Development
and Cooperation

ECOLOGY
An International Journal of Ecology

NORSK GEOGRAFISK TIDSSKRIFT
Norwegian Journal of Geography

NORSK GEOLOGISK TIDSSKRIFT
Norwegian Journal of Geology

NORWEGIAN ARCHAEOLOGICAL REVIEW

NORWEGIAN ARCHITECTURAL RESEARCH

NPRI SCIENCE REVIEW

Periodicals

ACTA BOREALIA
A Journal of Arctic Biology

ARCTIC
Journal of Arctic Biology

ARKEOLOGISKE SKRIFTER
Norwegian Archaeological Publications

ARMAUK
Journal of Ethiopian Studies

BERGMUSEETS ARBOK
Scientific Publications of the University
of Bergen

BOREAS
An International Journal of Quaternary
Geology

CULTURAL SURVIVAL QUARTERLY

DIRECTIONS
Norwegian Journal of Student Politics

SARSIA
Journal of Marine Biology

UNIVERSITETSFORLAGET